



저작자표시-비영리-변경금지 2.0 대한민국

이용자는 아래의 조건을 따르는 경우에 한하여 자유롭게

- 이 저작물을 복제, 배포, 전송, 전시, 공연 및 방송할 수 있습니다.

다음과 같은 조건을 따라야 합니다:



저작자표시. 귀하는 원저작자를 표시하여야 합니다.



비영리. 귀하는 이 저작물을 영리 목적으로 이용할 수 없습니다.



변경금지. 귀하는 이 저작물을 개작, 변형 또는 가공할 수 없습니다.

- 귀하는, 이 저작물의 재이용이나 배포의 경우, 이 저작물에 적용된 이용허락조건을 명확하게 나타내어야 합니다.
- 저작권자로부터 별도의 허가를 받으면 이러한 조건들은 적용되지 않습니다.

저작권법에 따른 이용자의 권리는 위의 내용에 의하여 영향을 받지 않습니다.

이것은 [이용허락규약\(Legal Code\)](#)을 이해하기 쉽게 요약한 것입니다.

[Disclaimer](#)

공학박사학위논문

하이퍼볼릭 메타물질을 응용한 초음파의
회절한계 이상 해상도 구현

Sub-wavelength resolution in ultrasonic waves by
hyperbolic metamaterials

2014년 2월

서울대학교 대학원

기계항공공학부

오 주 환

하이퍼볼릭 메타물질을 응용한 초음파의 회절한계 이상 해상도 구현

Sub-wavelength resolution in ultrasonic waves by
hyperbolic metamaterials

지도교수 김 윤 영

이 논문을 공학박사 학위논문으로 제출함

2013년 11월

서울대학교 대학원

기계항공공학부

오 주 환

오주환의 공학박사 학위논문을 인준함

2013년 12월

위원장 : 조 맹 효

부위원장 : 김 윤 영

위 원 : 김 도 년

위 원 : 장 강 원

위 원 : 이 진 우

Abstract

Sub-wavelength Resolution in Ultrasonic waves by hyperbolic metamaterials

Joo Hwan Oh

School of Mechanical and Aerospace Engineering

The Graduate School

Seoul National University

The research in this dissertation aims at realizing sub-wavelength resolution by newly designed elastic metamaterial lens. Generally, elastic wave based imaging technology has been considered as highly useful imaging method, but its resolution is relatively low compared to other imaging method. The most critical resolution issue in elastic wave based imaging is diffraction limit which forbids resolution over certain limit in general media. Thus, the following question had been risen – ‘*how to overcome diffraction limit?*’. In recent years, a big progress in metamaterial has realized hyperlens which allow resolution over diffraction limit. However, although proposition of hyperlens made a big break-through, researches on hyperlens were mainly focused on electromagnetic waves. Researches on hyperlens for elastic waves have been rare, and the performance of the previously designed elastic hyperlens was still limited. Motivated by this, a new elastic hyperlens that exhibits much improved performance than the previously proposed one is proposed in this work.

The study of new elastic hyperlens performed in this work not only deals proposition of the new hyperlens but also covers physical, numerical, experimental and analytic approaches. After reviewing background physics related to diffraction limit and hyperlens, the way to break the previous hyperlens' limitation is presented. New elastic metamaterial that satisfies pre-considered design requirements is engineered, and new elastic hyperlens is designed from the metamaterial. To verify the proposed elastic metamaterial and hyperlens, finite element analysis is formulated and numerical wave simulation is performed. For confirmation of performance improvement, numerical simulations with sub-wavelength sources are conducted for both the proposed hyperlens and the previous one, and the results are directly compared. In the experimental approach, the proposed hyperlens is realized in aluminum plate and sub-wavelength resolution of the hyperlens is experimentally shown. To achieve desired sub-wavelength sources, a new elastic wave transducer is developed. During experiments, actuation pulse tailoring and measured signal calibration is introduced to facilitate the experiment. Finally, analytic approach for the elastic metamaterial and hyperlens is performed. Equivalent mass-spring system for the designed metamaterial is constructed, and wave dispersion equation is analytically formulated. From the constructed analytic mass-spring system, design guidelines for further improvement of the proposed elastic hyperlens are shown.

Keywords: Hyperbolic equi-frequency curve, Elastic hyperlens,

Sub-wavelength resolution, Elastic metamaterial

Student Number: 2008-20762

Contents

Abstract.....	i
----------------------	----------

List of Figures.....	vi
-----------------------------	-----------

Chapter 1. Introduction.....	1
-------------------------------------	----------

1.1 Research motivation	1
1.2 History of metamaterial and sub-wavelength resolution	5
1.2.1 What is metamaterial?	5
1.2.2 Sub-wavelength imaging via metamaterial	7
1.3 Research objectives and coverage	11
1.4 Organization of the thesis	13

Chapter 2. Theories of metamaterial-based sub-wavelength resolution.....	15
---------------------------------------------------------------------------------	-----------

2.1 Chapter overview.....	15
2.2 Physical origin of diffraction limit.....	16
2.3 Physics behind sub-wavelength resolution by hyperlens.....	26
2.3.1 Hyperlens with hyperbolic EFC	26
2.3.2 Hyperlens with elliptic EFC	36

Chapter 3. Proposition of new elastic hyperlens based on hyperbolic elastic metamaterial.....	43
------------------------------------------------------------------------------------------------------	-----------

3.1 Chapter overview.....	43
3.2 Design of hyperbolic elastic metamaterial and hyperlens	45
3.2.1 Design requirements of proposed hyperbolic elastic metamaterial	45
3.2.2. How to obtain the desired hyperbolic elastic metamaterial?	49

3.2.3 Proposition of new hyperbolic elastic metamaterial and hyperlens	59
3.3 Numerical verification of hyperbolic elastic metamaterial.....	64
3.3.1 Finite element formulation for wave dispersion characteristics of the proposed elastic metamaterial	64
3.3.2 EFC calculation for the proposed elastic metamaterials.....	72
3.4 Numerical simulation for the proposed elastic hyperlens.....	77
3.4.1 Numerical simulation for sub-wavelength resolution.....	77
3.4.2 Numerical simulation for resolution improvement of the proposed hyperlens	84

Chapter 4. Experimental approach for the proposed elastic hyperlens 89

4.1 Chapter overview.....	89
4.2 Development of new elastic wave actuator for the experiment.....	90
4.3 Experimental procedure.....	98
4.3.1 Experimental setting.....	98
4.3.2 Signal post-processing.....	104
4.4 Experimental results	108

Chapter 5. Analytic approach for the proposed elastic hyperlens110

5.1 Chapter overview.....	110
5.2 Analytic modeling along circumferential directions.....	112
5.2.1 Analytic calculation of the dispersion relation of mass-spring model along circumferential directions	112
5.2.2 Calculation of the equivalent mass/spring coefficients along circumferential directions.....	115
5.2.3 Verification of the analytic modeling along circumferential directions..	121
5.3 Analytic modeling along radial directions	123

5.3.1 Analytic calculation of the dispersion relation of mass-spring model along radial directions	123
5.3.2 Calculation of the equivalent mass/spring coefficients along radial directions	129
5.3.3 Verification of the analytic modeling along radial directions.....	134
5.4 Design improvement by the proposed analytic method.....	136
Chapter 6. Conclusion	140
Appendix A. Finite element analysis of radiation characteristics of guided waves generated by magnetostrictive patch-type transducers	143
A.1. Appendix overview	143
A.2. Finite element formulation for general MPT's	147
A.2.1 Linearized magnetostrictive modeling for general MPT's	147
A.2.2 Time-harmonic wave simulation for general MPT's	152
A.2.3 Overall finite element analysis procedure	159
A.3. Verification of the proposed analysis and numerical observations	161
A.3.1 Verification of the proposed finite element analysis.....	161
A.3.2 Numerical observations for elastic wave generation in MPT's	172
A.4. Conclusion	175
References	178
Abstract (Korean)	192
Acknowledgements.....	194

List of Figures

Fig. 1.1 Schematic diagram of the effect of diffraction limit in elastic wave based imaging.....	2
Fig. 1.2 Schematic diagram of the wave propagation from two sub-wavelength sources (a) with and (b) without hyperlens.....	3
Fig. 1.3 (a) Picture of the previously proposed elastic hyperlens by Lee <i>et al.</i> [8], (b) experimental results of the previous hyperlens with two sub-wavelength sources inside the lens.....	4
Fig. 1.4 Schematic illustrations of propagating and evanescent waves' behaviors at (a) general medium, (b) superlens and (c) hyperlens	9
Fig. 2.1 Plane wave incidenting on circular crack with very small size	16
Fig. 2.2 Displacement plot of various scattering modes with the order of (a) 0, (b) 1, (c) 2, (d) 10, (e) 15 and (f) 20 around the circular crack at general isotropic media...	20
Fig. 2.3 EFC and internal wave characteristics of the general isotropic medium.....	23
Fig. 2.4 (a) Plot of the wavelength at two different radial location, and plot of the hollow zone generated in the (b) 10th order, (c) 15th order and (d) 20th order scattering mode, respectively	25
Fig. 2.5 EFC and internal wave characteristics of hyperlens with hyperbolic EFC	28
Fig. 2.6 Displacement plot of various scattering modes with the order of (a) 0, (b) 1, (c) 2, (d) 10, (e) 15 and (f) 20 at metamaterials having hyperbolic EFC	30
Fig. 2.7 (a) Wave propagating characteristics of evanescent wave incident at inner circle of hyperlens, (b) schematic illustration of wavevector compression inside the hyperlens	32
Fig. 2.8 Two representative composite structure with (a) radially and (b) circumferentially arranged layered structure for realization of hyperlens.....	36
Fig. 2.9 EFC and internal wave characteristics of the hyperlens with elliptic EFC.....	38
Fig. 2.10 Displacement plot of various scattering modes with the order of (a) 0, (b) 1, (c) 2, (d) 10, (e) 15 and (f) 20 at metamaterials having elliptic EFC	40

Fig. 3.1 Plot of Von-Mises stress at phononic crystal prism exhibiting bi-refraction phenomenon	48
Fig. 3.2 (a) Schematic diagram of mass-spring system for general phononic crystal, and free-body diagrams along (b) radial direction and (c) circumferential direction	50
Fig. 3.3 (a) Schematic diagram of newly proposed mass-spring system for desired hyperbolic elastic metamaterial, and free-body diagrams along (b) radial direction and (c) circumferential direction	55
Fig. 3.4 Schematic dispersion curve along circumferential and radial directions of the mass-spring system shown in fig. 3.3 (a)	58
Fig. 3.5 Geometric configuration of the proposed hyperbolic elastic metamaterial	59
Fig. 3.6 Picture of the proposed hyperlens consists of the proposed elastic metamaterial shown in fig. 3.5	60
Fig. 3.7 Mode shape of the S0 wave propagating along (a) circumferential and (b) radial direction in the proposed hyperbolic elastic metamaterial	62
Fig. 3.8 Schematic illustration of the periodic boundary condition imposed for wave dispersion calculation	69
Fig. 3.9 (a) Plot of the calculated dispersion surface, (b) plot of EFC which is extracted from (a) at desired frequency.....	73
Fig. 3.10 Plot of the EFC's at 15 kHz for varying value of a of the proposed elastic metamaterial	75
Fig. 3.11 Plot of the EFC's at various frequencies for the elastic metamaterials considered in fig. 3.6.....	76
Fig. 3.12 Finite element modeling for sub-wavelength resolution simulation with the proposed hyperlens	78
Fig. 3.13 Plot of the S0 wave displacement generated from two sub-wavelength sources (a) with and (b) without the proposed hyperlens	81
Fig. 3. 14 Plot of the S0 wave displacement inside the proposed hyperlens	82
Fig. 3.15 Plot of the hyperlens simulation results (a) with and (b) without the proper treatment of backward waves	83

Fig. 3. 16 Plot of the hyperlens simulation result with two sub-wavelength sources whose minimum separation distance d is 3.2 mm	85
Fig. 3.17 Comparison of the S0 wave's displacement field transmitted from the proposed hyperlens (left) and the previously proposed one by Lee <i>et al.</i> [8] (right) while the relative distance between two sub-wavelength sources with respect to the actuation wavelength are (a) 0.48, (b) 0.45 and (c) 0.41, respectively	88
Fig. 4.1 Schematic illustration of the proposed G-MPT and its operating principle	91
Fig. 4.2 Picture of two G-MPT installed inside the fabricated hyperlens	97
Fig. 4.3 Schematic diagram of the experimental procedure	99
Fig. 4.4 Picture of the series connection device used in the experiment (left) and circuit configuration of the series connection device (right)	100
Fig. 4.5 (a) Plot of modulated Gaussian pulse generally used in ultrasonic elastic wave based inspection, (b) tailored modulated Gaussian pulse used in the hyperlens experiment	102
Fig. 4.6 (a) Picture of S0 wave measurement that transmitted from the hyperlens, (b) measured raw data from the sensor in (a), (c) plot of STFT results of the raw data in (b), (d) extracted data from STFT results in (c) at 15 kHz	105
Fig. 4.7 (a) STFT results without data calibration, (b) improved STFT results after data calibration	107
Fig. 4.8 Comparison of the numerical and experimental results of the S0 wave displacements at the measurement points	109
Fig. 5.1 (a) Definition of Segment S_1 and S_2 , (b) equivalent mass-spring model for analytic investigation of the proposed elastic metamaterial	111
Fig. 5.2 (a) Equivalent mass-spring model for circumferential direction, and corresponding free-body diagrams of (b) m_1 and (c) m_2	113
Fig. 5.3 Mechanical models for stiffness analysis of (a) Segment S_1 and (b) Segment S_2	117
Fig. 5.4 Comparison of circumferential dispersion curves computed from the developed analytical model and the finite element model for metamaterials with $a =$ (a) 9.6 mm, (b) 14.4 mm and (c) 19.2 mm.	122

Fig. 5.5 (a) Equivalent mass-spring model for radial direction, (b) corresponding free-body diagram	124
Fig. 5.6 (a) Equivalent mass-spring model for radial direction with additional shear spring s_4 , and corresponding free-body diagrams of (b) m_3 and (c) m_4	126
Fig. 5.7 (a) Equivalent mass-spring model for general internal resonant structures, and corresponding free-body diagrams of (b) m'_3 and (c) m'_4	128
Fig. 5.8 Mechanical models for stiffness analysis of (a) Segment S_1 and (b) Segment S_2	130
Fig. 5.9 Comparison of radial dispersion curves computed from the developed analytical model and the finite element model for metamaterials with $a =$ (a) 9.6 mm, (b) 14.4 mm and (c) 19.2 mm.....	135
Fig. 5.10 (a) Original hyperbolic elastic metamaterial proposed in the previous chapter, (b) newly designed hyperbolic elastic metamaterial	137
Fig. 5.11 Comparison of dispersion curves between original metamaterial (left) and new metamaterial (right) for $w =$ (a) 9.6 mm, (b) 14.4 mm and (c) 19.2 mm.	139
Fig. A.1 (a) Schematic illustration of an MPT installed on a plate waveguide with circular magnetostrictive patch, (b) typical magnetostriction curve	144
Fig. A.2 a finite element in the patch under simultaneous applications of the static magnetic field H_s and the dynamic magnetic field H_D	149
Fig. A.3 The total displacement field distribution in the waveguide obtained by the proposed finite element method.....	155
Fig. A.4 Schematic diagram of the waveguide mode extraction scheme at the measurement point.....	157
Fig. A.5 The results of spatial Fourier transformation for two displacement fields measured along the dotted line in fig. A.3	158
Fig. A.6 The proposed finite element analysis procedure for the MPT-waveguide system	160
Fig. A.7 The geometric parameters of MPT's considered in CASE 1 and CASE 2	162
Fig. A.8 Plots of wave displacement fields of (a) S0 mode and (b) SH0 mode generated by the MPT of CASE 1 with $\theta = 0^\circ$	166

Fig. A.9 Comparison of the numerically and experimentally measured radiation patterns of the S0 mode for CASE 1 with (a) $\theta = 0^\circ$, (b) $\theta = 45^\circ$ and (c) $\theta = 90^\circ$...	167
Fig. A.10 Comparison of the numerically and experimentally measured radiation patterns of the SH0 mode for CASE 1 with (a) $\theta = 0^\circ$, (b) $\theta = 45^\circ$ and (c) $\theta = 90^\circ$...	168
Fig. A.11 Plots of wave displacement fields of (a) S0 mode and (b) SH0 mode generated by the MPT of CASE 2 with $\theta = 0^\circ$	170
Fig. A.12 Comparison of the numerically and experimentally measured radiation patterns of (a) the S0 mode and (b) the SH0 mode for CASE 2 with $\theta = 0^\circ$	171
Fig. A.13 Distribution plots of (a) coupling coefficient d_{35} , (b) induced dynamic magnetic field H_{D_y} and (c) external shear force term S_{MS_y} in the patch	173
Fig. A.14 Comparison of the SH0 mode generated by the MPT with a circular patch of various radiuses with $\theta = 90^\circ$	175

Chapter 1.

Introduction

1.1 Research motivation

Wave-based imaging technology has been widely used in many engineering applications, such as microscopy in optics, sonar applications in acoustic and non-destructive evaluations (NDE) in elastics. By imposing incident wave to sample or crack and measuring reflected wave, wave-based imaging technology allows fast, in-vivo non-destructive imaging for wide region with low cost. Nevertheless, wave-based imaging suffers from several shortcomings, and one of the most critical problems is low resolution. In fact, the resolution and accuracy of wave-based imaging is somewhat low, which limits applicable fields of the imaging technology.

To overcome the resolution issue, researchers tried to develop a new technology that can improve the resolution of wave-based imaging. However, in 1873, Abbe showed that the resolution problem in wave-based imaging is fundamental problem that cannot be overcome by any technology [1]. He showed that two sample of which the separation distance is below half of the wavelength are impossible to be distinguished by wave-based imaging (fig. 1.1), i.e., every wave-based imaging has theoretic resolution limit, called Abbe-Rayleigh limit, or more generally, diffraction limit. After the Abbe's frontier work, researchers no more tried to find *technology that can improve resolution*, instead

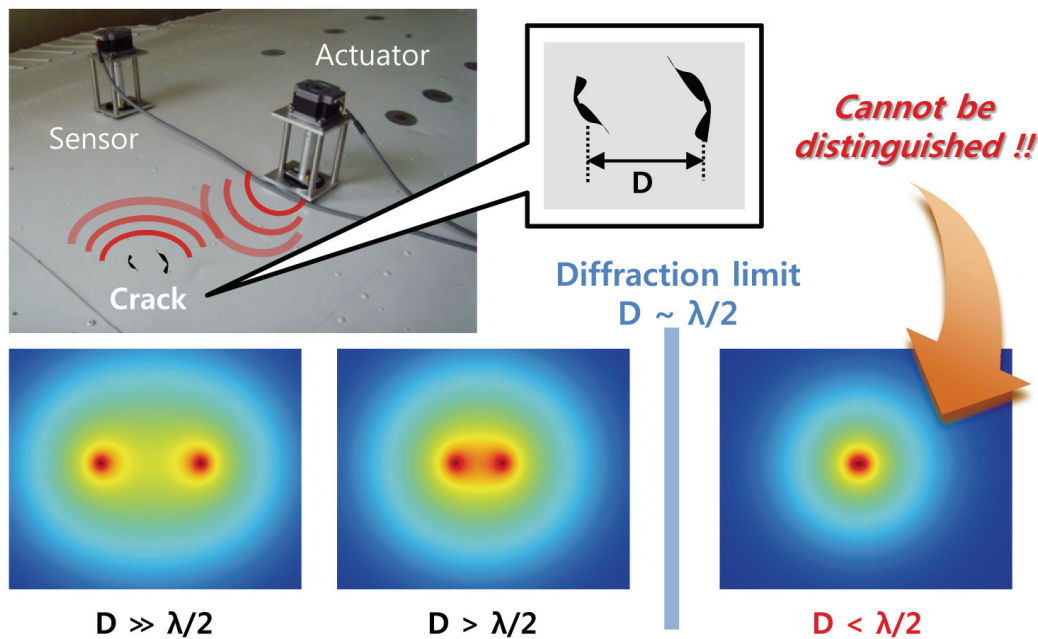


Fig. 1.1 Schematic diagram of the effect of diffraction limit in elastic wave based imaging

they have tried to find *technology that can break diffraction limit*. New methods that allow resolution over diffraction limit, called sub-wavelength resolution, have been proposed by utilizing near-field scanning [2], fluorescence [3], interference [4], etc [5]. Unfortunately, these methods usually achieved sub-wavelength resolution by sacrificing imaging speed.

Recently, break-through in sub-wavelength resolution technique has been made by using new concept in wave physics, called metamaterial. Metamaterial is artificially made materials which exhibit extraordinary wave phenomena that cannot be achieved by materials in nature. Especially, metamaterial can exhibit negative parameters, such as $\varepsilon < 0$ and $\mu < 0$ for electromagnetic waves. By utilizing the negative parameter of

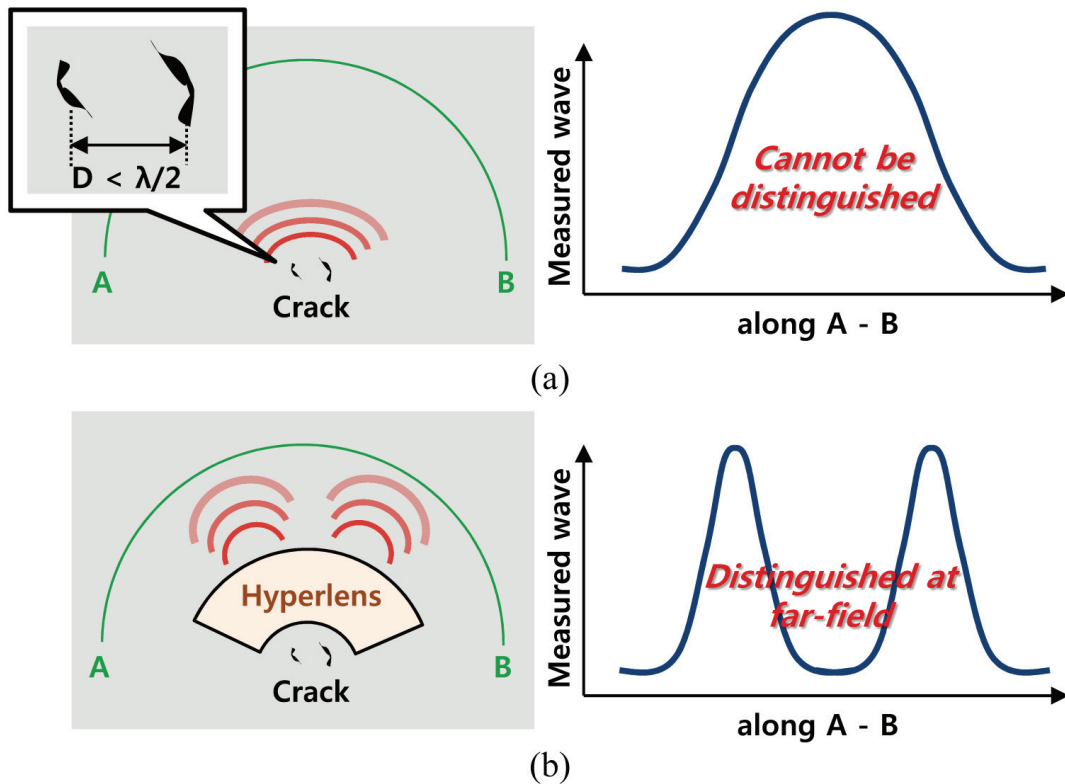


Fig. 1.2 Schematic diagram of the wave propagation from two sub-wavelength sources (a) with and (b) without hyperlens

metamaterials, new wave-based device called hyperlens is recently developed [6,7]. Hyperlens allow sub-wavelength resolution even at the far-field, as in fig. 1.2, which guarantee fast imaging speed. Moreover, hyperlens has theoretically un-limited resolution. Thus, hyperlenses have been achieved much attentions these days and expected to open new era in wave-based imaging technologies. Previous researches on hyperlens and metamaterial-based sub-wavelength technique are given in the following sections.

Although a large amount of researches have been performed on hyperlens, they usually

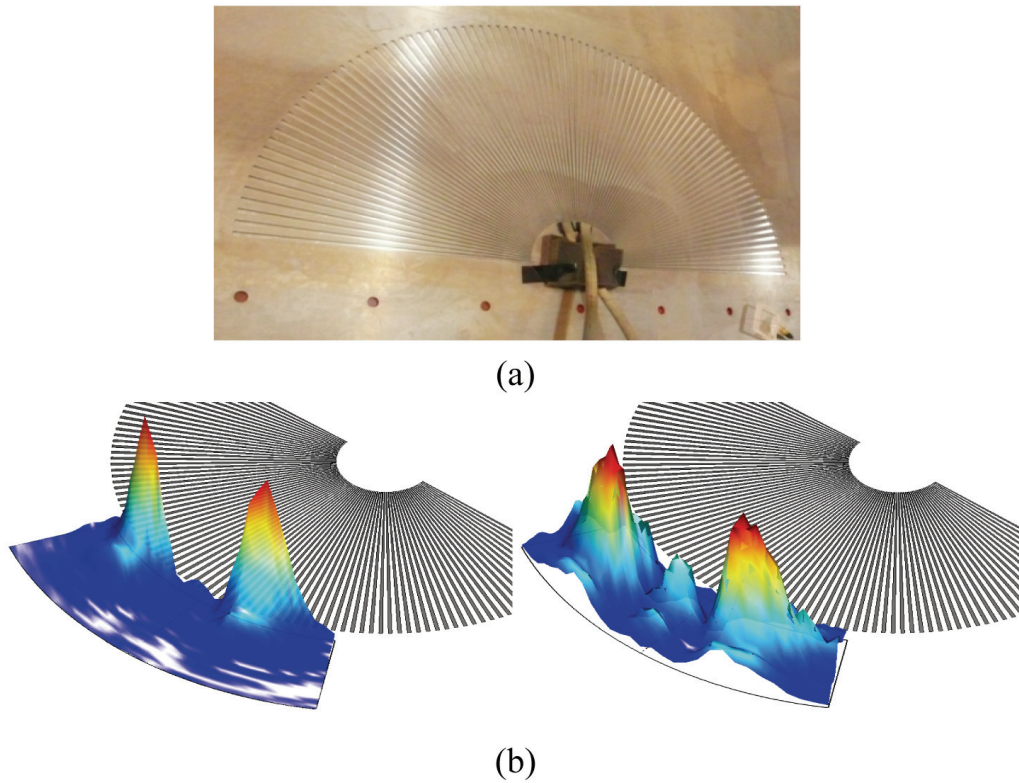


Fig. 1.3 (a) Picture of the previously proposed elastic hyperlens by Lee *et al.*[8], (b) experimental results of the previous hyperlens with two sub-wavelength sources inside the lens

focused on electromagnetic waves while researches on hyperlens for elastic waves are somewhat limited. Unlike electromagnetic waves for which metamaterial with negative parameter can be easily obtained by plasmonics effect, it is very hard to obtain metamaterial with negative parameter for elastic waves. Thus, only the hyperlens having limited performance has been realized for elastic waves by Lee *et al.* [8]. As in fig. 1.3, by using alternatively layered aluminum fin and air heterostructure, Lee *et al.* [8] realized elastic hyperlens without negative parameter but instead using extreme anisotropy. Although this previous work could realize resolution over diffraction limit at far-field for

elastic waves, its resolution is theoretically limited, unlike hyperlenses in electromagnetic waves. Regarding that elastic wave based imaging is widely used such as non-destructive evaluation or non-destructive testing in structural health monitoring, there is a need for the hyperlens which exhibit much higher resolution, i.e., theoretically un-limited resolution. However, there has been no work that realized the elastic hyperlens which shows theoretically un-limited resolutions.

Motivated by the issue, this thesis will proposed and realize a new elastic hyperlens which is improved than the previous work done in Ref. [8]. Before presenting the detailed researches, it is worth to review related researches for metamaterials and sub-wavelength resolution, especially for hyperlens. From the review, the research motivation of the work would be more cleared.

1.2 History of metamaterial and sub-wavelength resolution

1.2.1 What is metamaterial?

Metamaterial is artificially-made material that cannot be found in the nature. Unlike previous human-made materials which were based on chemical or physical processing, metamaterial is based on the artificially-designed microstructure of which the scale is usually much smaller than the wavelength of operating frequency. Among many interesting properties of metamaterials, the most striking point is that metamaterials can exhibit negative parameters which are impossible to be achieved by the existing materials.

As negative parameters become available by metamaterials, the border of wave physics is extremely expanded.

The first research of metamaterial was made in 1986 when Veselago [9] theoretically predicted the physics related to the metamaterial. Veselago theoretically showed how electromagnetic waves will behave if they encounter negative material, having $\epsilon < 0$ and $\mu < 0$. However, the negative material could not be realized at that time. By using plasmon, negative ϵ was available but the frequency range was extremely high. Furthermore, negative μ was not available at that time. As a result, the researches related to the metamaterial had been almost abandoned till mid-1990s. In 1996, Pendry and his co-workers found that plasmon can be generated at relatively low frequency ranges [10], and eventually, showed that negative ϵ can be realized by using low frequency plasmons [11]. Based on these works, Smith and his co-workers [12] realized the electromagnetic metamaterial having both negative ϵ and μ . They utilized split-ring-resonator to achieve negative μ by resonance phenomena while negative ϵ was achieved by low frequency plasmons. After these frontier works, extremely large amount of researches have been published, including the studies for cloaking device, waveguide, tunneling, etc. Since there are too many researches for metamaterials, they will not be dealt in this thesis except those related to sub-wavelength resolution.

On the other hand, there had been other researches that realized negative parameter in different way. Researches on periodic structures, called photonic crystals, had found that

the extraordinary wave characteristics can also be achieved by periodic structures. The major difference between metamaterial and photonic crystal is scale of unit cell; the unit cell of metamaterial is usually much smaller than operating wavelength while that of photonic crystal is usually in similar order with respect to operating wavelength. In 2003, Cubukcu and his co-workers [13] found that photonic crystals can also exhibit negative refraction phenomenon which was only observed by the metamaterial having simultaneously negative parameters, such as $\epsilon < 0$ and $\mu < 0$. From then, photonic crystals started to gather much attention as metamaterial. Although the term metamaterial generally cover photonic crystal (or, phononic crystal, which is acoustic/elastic counterpart of photonic crystal in electromagnetic wave), those two materials are distinguished in this thesis since wave behavior of two materials is somewhat different. As will be shown in chapter 3, phononic crystals cannot be utilized in this work due to its comparably large unit cell size.

1.2.2 Sub-wavelength imaging via metamaterial

The first attempt to use metamaterials in sub-wavelength resolution was made in 2000 when Pendry *et al.* [14] proposed that negative refraction due to negative ϵ and μ can make a perfect lens, called superlens. Since metamaterial having both negative ϵ and μ can reverse the spatial distribution of incident waves and re-amplify decaying evanescent waves, any waves actuated from source (including propagating and evanescent waves) can be focused at the other side of superlens with same amplitude as they are actuated. Thus, Pendry *et al.* proposed that a perfect imaging can be made at

other side of the superlens.

Based on this work, Fang *et al.* [15] first realized the superlens which can realize sub-wavelength resolution at near the lens. Melville *et al.* [16] also confirmed sub-wavelength resolution by superlens. Wood *et al.* [17] expanded the previously proposed single layered superlens into multi-layered structures. Taubner *et al.* [18] combined the idea of superlens with a scanning probe microscopy to achieve sub-wavelength resolution. On the other hand, the same idea of superlens was also adopted in photonic crystal fields as Luo *et al.* [19], Parimi *et al.* [20] and Cubukcu *et al.* [21]. For more details about superlens for electromagnetic waves, see Ref. [22]. Focusing on superlens for other waves than electromagnetic waves, Ambati *et al.* [23] showed that superlens can be realized in acoustic fields by using surface resonant states in 2007. Deng *et al.* [24] theoretically studied the acoustic superlens made of solid array immersed in liquid mercury. Jia *et al.* [25] experimentally realized acoustic superlens. Also, acoustic superlenses have been realized by phononic crystals, as Sukhovich *et al.* [26] and He *et al.* [27].

Although the idea of superlens opened a new way in sub-wavelength resolution, superlens still had a problem that imaging should be made at the near field of the lens. Since evanescent waves that propagate through superlens still decay, sub-wavelength resolution at far-field is impossible. This results in slow imaging speed, which is not preferred in wave based imaging. Sub-wavelength resolution at far-field wasn't realized until a new idea of hyperlens came out.

In 2006, Jacob *et al.* [6] and Salandrino *et al.* [7] first proposed a concept of hyperlens, which allow sub-wavelength resolution at far-field. The major difference between superlens and hyperlens is illustrated in fig. 1.4. As in fig. 1.4, evanescent waves propagating through superlens are amplified but still decays after they pass through the

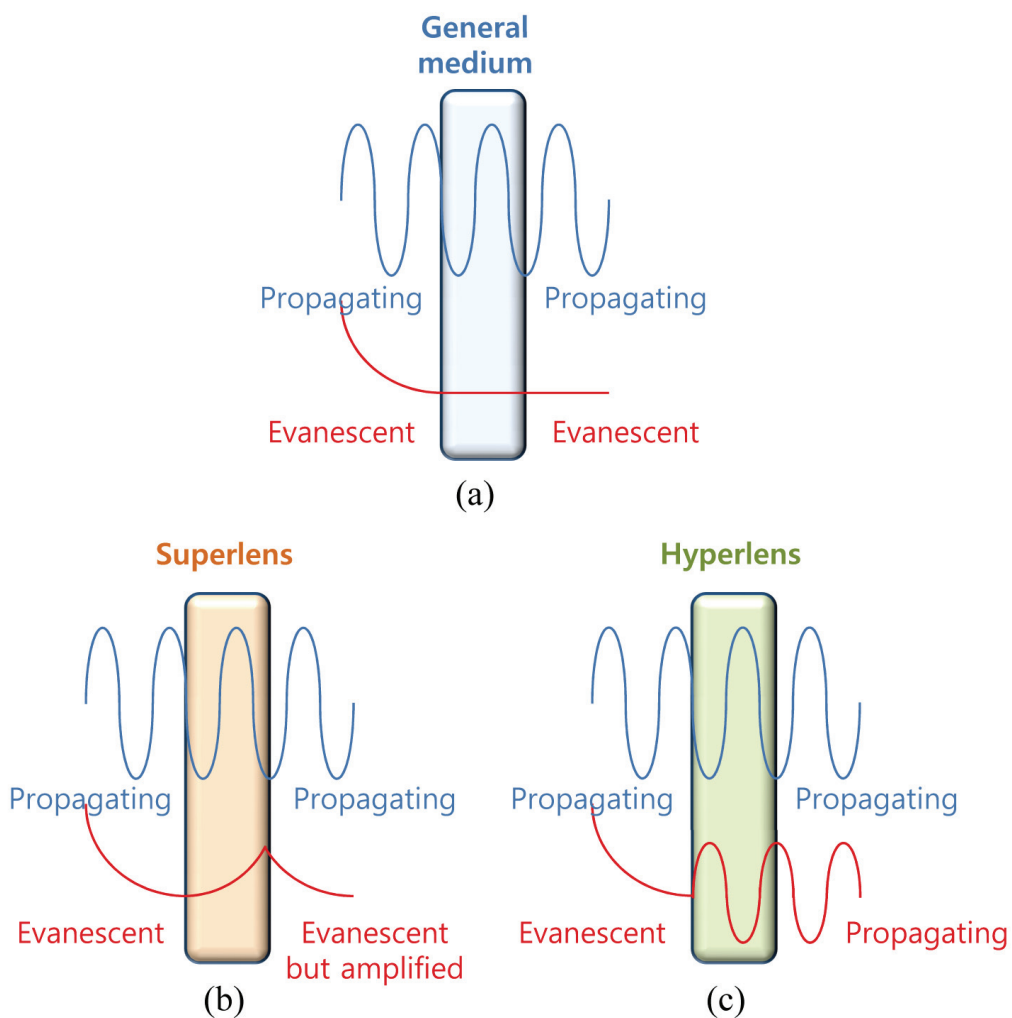


Fig. 1.4 Schematic illustrations of propagating and evanescent waves' behaviors at (a) general medium, (b) superlens and (c) hyperlens

lens. However, evanescent waves propagating through hyperlens becomes propagating waves as they pass through the lens. Thus, all scattering modes can be measured at far-field, resulting in perfect imaging. In fact, hyperlens guarantees theoretically un-limited resolution at far field.

After the frontier researches done by Ref. [6, 7], Zhang's research group [28, 29] first realized electromagnetic hyperlens by arranging silver and dielectric nano layer. Kildishev *et al.* [30] proposed impedance matched hyperlens which shows improved transmission performance. Wang *et al.* [31] studied planar hyperlens by transformational optics. Xiong *et al.* [32] proposed idea to adopt hyperlens to lithography. Recently, Rho *et al.* [33] realized spherical hyperlens for 2-dimensional sub-wavelength resolution. For more researches about electromagnetic hyperlens, see Ref. [34].

Accordingly, several researches for acoustic hyperlenses have been performed, but the researches are somewhat limited compared to the electromagnetic hyperlenses due to difficulty of metamaterial realization. Ao *et al.* [35] first demonstrated that acoustic hyperlens can be achieved by using internal resonance structures. However, since the metamaterial is based on internal resonance structure, it may suffer from high loss and narrow operating frequency ranges. In 2009, Li *et al.* [36] realized acoustic hyperlens and sub-wavelength resolution for acoustic wave is experimentally shown by the lens. In his work, Li utilized extremely anisotropic structure which was not based on resonance nature, thus can avoid the problems that occurs due to resonance nature [37]. Based on the idea proposed by Li, Zhu *et al.* [38] realized a holey structured lens which exhibits

extremely high resolution recently. However, these acoustic hyperlenses had a limited performance that the resolution of the lenses was theoretically limited while the hyperlenses for electromagnetic waves had theoretically un-limited resolution. Chiang *et al.* [39] designed acoustic hyperlens having theoretically un-limited resolution based on internal resonance structure, but it suffered from the problems related to the resonance and wasn't realized.

For elastic waves, the works related to hyperlens are very rare. In 2011, Lee *et al.* [8] adopted the idea of Li and realized elastic hyperlens by using extreme anisotropic elastic metamaterial. However, this elastic hyperlens also had a limited performance as those in [37, 38]. Still, the elastic hyperlens which shows theoretically un-limited resolution has not been realized.

1.3 Research objectives and coverage

As explained in the previous section, the motivation of the present research is obvious; unlike those in acoustics and electromagnetic, only few works have been performed for elastic hyperlens. Moreover, the previously proposed elastic hyperlens had a degraded performance compared to the electromagnetic hyperlenses. Thus, the major objective of the present research is to develop a new elastic hyperlens which exhibit improved performance than the previous one in Ref. [8]. To achieve the major objective, the following questions should be properly answered;

- **How to improve hyperlens' imaging performance?**

Hyperlenses proposed for electromagnetic waves have theoretically un-limited resolution while that for elastic wave has theoretically limited resolution. The reason of the difference is studied to develop elastic hyperlens with theoretically un-limited resolution.

- **How to design proper elastic metamaterials for new hyperlens?**

Regarding that the property of metamaterials is based on their microscopic geometry rather than material properties, proper design of elastic metamaterial is key in metamaterial-based engineering. To develop a new elastic hyperlens, requirements that the new elastic metamaterial should satisfy are established and new elastic metamaterial is properly designed.

- **How to experimentally verify the new elastic hyperlens?**

Although the performance of the new elastic hyperlens can be numerically shown, it is no use until the idea is realized and supported by experimental verification. By using experimental equipments for elastic waves, sub-wavelength capability of the new elastic hyperlens is experimentally shown.

- **How to formulate analytic model for the new elastic hyperlens?**

Analytic model provides explicit relation between design variables of the elastic metamaterial and performance of the hyperlens. Thus, analytic model can provide a guideline in hyperlens design or optimization. Based on equivalent mass-spring system, the analytic model for the new hyperlens is formulated and verified.

1.4 Organization of the thesis

In chapter 2, physics behind diffraction limit and hyperlens are studied. Study of physical origins of diffraction limit and hyperlens are important in this research since it can provide guidelines for improved sub-wavelength resolution. First, the reason why diffraction limit cannot be overcome in general materials is revealed. In addition, the operating principle of hyperlens is subsequently reviewed. From the operating principle, the reason why previously proposed elastic metamaterial suffers from theoretical resolution limit is clearly shown. As a result, the way how to improve the performance of the elastic hyperlens from the previous one is presented in the chapter.

Chapter 3 is mainly dedicated to proposition of new elastic metamaterial and elastic hyperlens. To realize metamaterials having negative parameter in elasticity, design issues required for new elastic metamaterial are figured out. From the issues, new elastic metamaterial that is expected to form desired elastic hyperlens is engineered. Subsequently, its wave dispersion characteristics are evaluated to check whether it can show sub-wavelength resolution. In wave dispersion characteristics, finite element analysis method is utilized whose formulation is derived in the thesis. After the proposition of the new elastic hyperlens, resolution improvement by the new hyperlens is verified by numerical simulation.

In chapter 4, experimental investigation is made for the proposed elastic hyperlens. Although the performance of the proposed hyperlens is verified in chapter 3 by

numerical simulation, there still exists a question that the proposed hyperlens is realizable. Chapter 4 clearly answers the question by elastic guided wave-based hyperlens experiment. To facilitate the experimental procedure, new elastic wave actuator is developed which is tailored for the hyperlens experiment. Detailed experimental procedure is given including several issues in post-processing. In addition, the experimental results are compared with those by numerical simulations to check the feasibility of the experiments. From chapter 4, the sub-wavelength resolution of the hyperlens is proved to be realizable.

In chapter 5, an analytic modeling dedicated to the proposed hyperbolic elastic metamaterial is established. The analytic approach made in this chapter can provide explicit relation between overall wave characteristics and design variables. Accordingly, further researches such as design optimization are expected to be carried out based on the analytic method. An equivalent mass-spring system is constructed and wave dispersion equation is analytically derived from the system. Subsequently, equivalent mass and spring coefficients of the constructed mass-spring system with respect to the proposed elastic metamaterial are calculated.

Finally, conclusion of the thesis is made in chapter 6.

Chapter 2.

Theories of metamaterial-based sub-wavelength resolution

2.1 Chapter overview

In this chapter, physical origin of diffraction limit is reviewed since it can clearly show the operating principle of hyperlens and related resolution issues. Diffraction limit is a theoretical resolution limit that any two particles of which the separation distance is smaller than half of the wavelength cannot be distinguished at far field [1]. Since the limit is related to the operating wavelength, the most general way in achieving high resolution was using a shorter wavelength, i.e., high frequency. However, waves having high frequency inevitably suffer from high loss, resulting in a low penetration depth [40]. On the other hand, sub-wavelength resolution has been also obtained by near-field scanning [2,4] which rarely suffer from diffraction limit, but they were much slower than conventional wave based imaging. Until hyperlens is developed, every wave based imaging method could not avoid diffraction limit. The reason why diffraction limit cannot be overcome is revealed in this chapter.

In addition, the operating principle of sub-wavelength resolution in hyperlens is subsequently reviewed. Recent advances in metamaterials open a new way of higher resolution than diffraction limit, which was believed to be impossible to be exceeded previously. The metamaterial based sub-wavelength resolution device, called hyperlens, has a noble characteristic that allow sub-wavelength resolution at far-field, so higher

resolution (exceeding diffraction limit) can be achieved with fast imaging speed. Before the idea of metamaterial is introduced, every available material theoretically exhibited diffraction limit since their material parameters were positive. However, by using the idea of metamaterial, material having negative parameters becomes now available. The key in hyperlens is making lens with the metamaterial that is free from diffraction limit by properly engineering the negative parameters. The physics lying behind the avoidance of diffraction limit is shown in this chapter. Furthermore, the reason why existing elastic hyperlens should suffer from low performance is figured out, which provides the way to new elastic hyperlens.

2.2 Physical origin of diffraction limit

To explain the physical origin of diffraction limit, consider a simple wave-based crack imaging case. Imagine that plane wave is incident to very small circular crack as in fig. 2.1. To achieve the crack imaging, one should measure every scattered waves from the crack and re-construct the imaging. In other word, if one fails to measure any of the

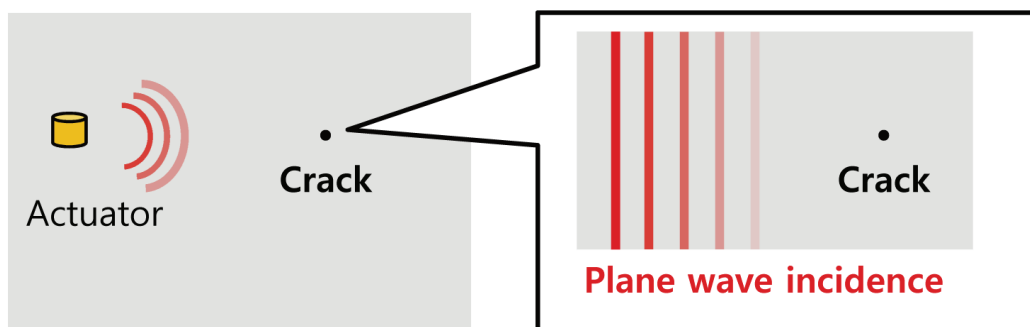


Fig. 2.1 Plane wave incidenting on circular crack with very small size

scattered waves, imaging cannot be perfectly re-constructed. This results in loss of information and reduction of imaging resolution. To study the behavior of scattering waves at general media, let's begin with wave equation at isotropic media which can be written as [41]

$$\nabla^2 u = \frac{1}{c^2} \frac{\partial^2 u}{\partial t^2} \quad (2.1)$$

where u , c and t denote displacement field, wave speed and time, respectively. In cylindrical coordinate (r, θ, z) , the gradient operator ∇^2 is defined as

$$\nabla^2 = \frac{\partial^2}{\partial r^2} + \frac{1}{r} \frac{\partial}{\partial r} + \frac{1}{r^2} \frac{\partial^2}{\partial \theta^2} + \frac{\partial^2}{\partial z^2} \quad (2.2)$$

Here, for simplicity, we only focus on 2 dimensional wave propagation in (r, θ) plane and assume $\partial / \partial z = 0$. As a result, equation (2.2) can be re-written as

$$\frac{\partial^2 u}{\partial r^2} + \frac{1}{r} \frac{\partial u}{\partial r} + \frac{1}{r^2} \frac{\partial^2 u}{\partial \theta^2} = \frac{1}{c^2} \frac{\partial^2 u}{\partial t^2} \quad (2.3)$$

To solve equation (2.3), it is convenient to assume the following time-harmonic wave solution

$$u = u_0 R \Theta \exp(i\omega t). \quad (2.4)$$

In equation (2.3), R and Θ are functions of only r and θ as

$$R = R(r), \quad \Theta = \Theta(\theta). \quad (2.5)$$

Here, $i = \sqrt{-1}$, and ω is angular frequency. Substituting equation (2.4) and (2.5) to equation (2.3) yields

$$\begin{aligned}
u_0 \frac{d^2 R}{dr^2} \Theta \exp(i\omega t) + u_0 \frac{1}{r} \frac{dR}{dr} \Theta \exp(i\omega t) + u_0 \frac{1}{r^2} \frac{d^2 \Theta}{d\theta^2} R \exp(i\omega t) \\
= -u_0 \frac{\omega^2}{c^2} R \Theta \exp(i\omega t)
\end{aligned} \tag{2.6}$$

Dividing $u = u_0 R \Theta \exp(i\omega t)$ at both sides of equation (2.6) results in following equation;

$$\left(\frac{1}{R} \frac{d^2 R}{dr^2} \right) + \frac{1}{r} \left(\frac{1}{R} \frac{dR}{dr} \right) + \frac{1}{r^2} \left(\frac{1}{\Theta} \frac{d^2 \Theta}{d\theta^2} \right) = -\frac{\omega^2}{c^2} . \tag{2.7}$$

To solve equation (2.7), following assumption is introduced;

$$\frac{1}{\Theta} \frac{d^2 \Theta}{d\theta^2} = -m^2 . \tag{2.8}$$

where m is arbitrary value for now. Substituting equation (2.8) to equation (2.7) yields following differential equation consists of only r term as

$$\left(\frac{1}{R} \frac{d^2 R}{dr^2} \right) + \frac{1}{r} \left(\frac{1}{R} \frac{dR}{dr} \right) - \frac{m^2}{r^2} = -\frac{\omega^2}{c^2} . \tag{2.9}$$

Since both equation (2.8) and equation (2.9) consist of only single degree of freedom (θ for equation (2.8) and r for equation (2.9)), each differential equation can be easily solved separately.

First, focusing on equation (2.8), it is a simple differential equation whose solution can be written as

$$\Theta(\theta) = \Theta_0 \exp(im\theta) . \tag{2.10}$$

The solution in equation (2.10) can satisfy equation (2.8) for any value of m . However, in physical point of view, the wave solution u at $\theta = 0$ should satisfy periodic condition

which can be expressed as

$$\Theta(\theta) = \Theta(\theta + 2\pi). \quad (2.11)$$

Since Θ is the only term which is affected by θ as in equation (2.4), equation (2.11) indicate that m should be integer.

On the other hand, equation (2.9) can be re-written as

$$r^2 \frac{d^2 R}{dr^2} + r \frac{dR}{dr} + \left(\frac{r^2 \omega^2}{c^2} - m^2 \right) R = 0. \quad (2.12)$$

Equation (2.12) is a Bessel differential equation whose solution can be written as

$$R(r) = R_0 J_m \left(\frac{\omega}{c} r \right) + R_0^* Y_m \left(\frac{\omega}{c} r \right) \quad (2.13)$$

where J_m and Y_m are Bessel functions of the first kind and second kind, respectively, of order m . Although the solution in equation (2.13) satisfies equation (2.12) for any values of R_0 and R_0^* , R_0^* should be zero to ensure finite displacement field at the origin. Substituting equation (2.13) and (2.11) to equation (2.4), the following wave solution can be achieved.

$$u = \left[\sum_{m=-\infty}^{m=\infty} U_m J_m \left(\frac{\omega}{c} r \right) \exp(im\theta) \right] \exp(i\omega t). \quad (2.14)$$

From equation (2.14), it can be seen that any waves propagating in cylindrical coordinate, including scattering waves, can be expressed in the series of infinite orders of waves. Since we are focusing on the scattered waves around the crack, each wave modes in equation (2.14) is denoted as scattering modes in the rest of the thesis.

The mode shapes of the scattering modes of several orders are plotted in fig. 2.2. In fig. 2.2, it can be observed that the wavelength along the circumferential direction becomes lower, i.e., the circumferential component of the m th order scattering mode's wavevector (k_θ^m) increases, as the order of the mode m increases. It should be noted that high resolution along radial direction requires short radial wavelength while that along circumferential direction requires short circumferential wavelength. To obtain image details and improve imaging resolution, higher resolution along circumferential direction is essential. Therefore, from fig. 2.2, it can be figured out that the scattering waves of

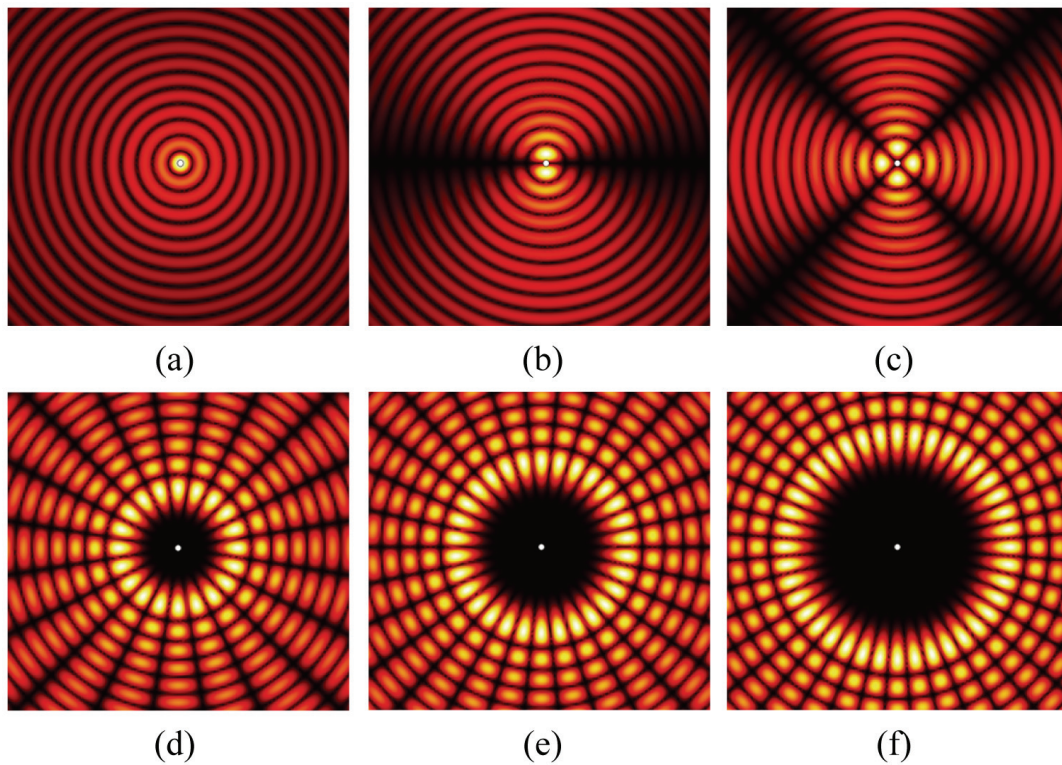


Fig. 2.2 Displacement plot of various scattering modes with the order of (a) 0, (b) 1, (c) 2, (d) 10, (e) 15 and (f) 20 around the circular crack at general isotropic media

higher orders are key in the resolution improvement.

Based on this observation, let's consider wave dispersion relation. For waves in every media, the following dispersion relation should be satisfied [42];

$$c_r^2 k_r^2 + c_\theta^2 k_\theta^2 = \omega^2 \quad (2.15)$$

where c is wave speed at the media and ω is angular frequency. Here, k_r and k_θ denote radial and circumferential component of the wavevector, respectively. For isotropic media, equation (2.15) can be re-written as

$$k_r^2 + k_\theta^2 = \omega^2 / c^2 . \quad (2.16)$$

Equation (2.16) indicates that wavevector k_r and k_θ are not independent variables; for given frequency, waves in isotropic media having wave speed c should have wavevector (k_r, k_θ) that satisfies the wave dispersion relation shown in equation (2.16).

Then, what if k_θ is very high as in higher order scattering mode? To investigate this case, equation (2.16) is re-written as

$$k_r = \sqrt{\omega^2 / c^2 - k_\theta^2} . \quad (2.17)$$

From equation (2.17), it can be inferred that k_r is purely imaginary if

$$k_\theta > \omega / c \text{ or } k_\theta < -\omega / c . \quad (2.18)$$

For this case, wave propagating along radial direction becomes

$$u = \exp(ik_r r)U(\theta, t) = \exp(-|k_r| r)U(\theta, t) . \quad (2.19)$$

Equation (2.19) indicates that wave's displacement field u along radial direction does not exhibit sinusoidal motion anymore. It exhibit rather exponentially decaying motion as it propagates radially - the wave is evanescent wave along radial direction. Regarding that the m th order scattering mode's circumferential wavevector k_θ^m increases as m increases, higher order scattering modes having k_θ^m higher than ω/c cannot propagate to far-field since their corresponding radial wavevector k_r^m should be purely imaginary. As a result, higher order scattering modes, which contain detailed information along the circumferential direction, cannot be measured at far-field. Regardless of technique additionally applied, resultant imaging inevitably has a low circumferential resolution since detailed image information carried by higher order scattering modes are lost. This is why diffraction limit take place when wave based imaging is performed at far-field.

To more clearly illustrate physical origin of diffraction limit, equi-frequency contour (EFC) might be helpful. EFC is wave dispersion curve plotted in (k_r, k_θ) plane at certain frequency ω . For example, EFC of isotropic media is circle (as can be expected in equation (2.16)) whose radius is equal to ω/c , as in fig. 2.3. In fig. 2.3, waves having k_θ between $-\hat{k}_\theta$ and \hat{k}_θ (which belongs to the yellow region) has a real k_r value since there exist a contour in the yellow region, i.e., there exist a real valued k_r that satisfies equation (2.16). However, waves having k_θ lower than $-\hat{k}_\theta$ or higher than \hat{k}_θ (which belongs to the orange region) should have a purely imaginary k_r value. There are no contours in the orange region suggesting that k_r should be purely

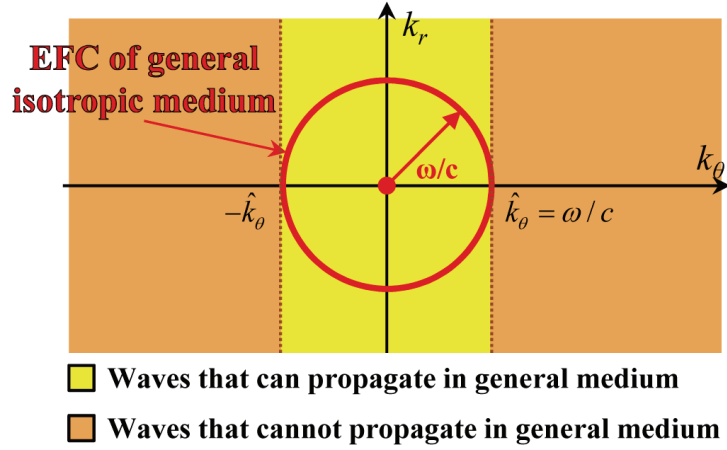


Fig. 2.3 EFC and internal wave characteristics of the general isotropic medium

imaginary to satisfy equation (2.16). This point can be summarized as

$$k_r \text{ is purely real if } -\omega/c = -\hat{k}_\theta < k_\theta < \hat{k}_\theta = \omega/c. \quad (2.20a)$$

$$k_r \text{ is purely imaginary if } k_\theta < -\hat{k}_\theta = -\omega/c \text{ or } k_\theta > \hat{k}_\theta = \omega/c \quad (2.20b)$$

for general isotropic media.

Unfortunately, waves having low k_θ that are propagating waves only have large scale information, and small scale information is carried by waves having high k_θ that are evanescent waves. Therefore, wave based imaging at far field can be made by using only the waves in the yellow region while small scale information are lost, resulting in the diffraction limited imaging.

Before proceeding to the next issue, let me introduce another explanation of the physical origin of diffraction limit, made by Jacob *et al.* [6]. In this approach, diffraction limit is

explained in the viewpoint of incident plane waves, while the previous explanation shown in the thesis focused on scattering waves. As shown in equation (2.14), every waves in cylindrical coordinate can be expressed in the infinite series of wave solutions shown in equation (2.14). Especially, plane wave propagating through x direction in Cartesian coordinate (x, y) can be expressed in the sum of infinite wave modes in cylindrical coordinate (r, θ) as

$$u = \left[\sum_{m=-\infty}^{m=\infty} U_m i^m J_m \left(\frac{\omega}{c} r \right) \exp(im\theta) \right] \exp(i\omega t). \quad (2.21)$$

According to Jacob *et al.* [6], wave-based imaging by incidenting plane wave can be seen as imaging by infinite incident waves in equation (2.21) whose displacement field distribution is same as that of each scattering modes. Thus, incident wave components having low m may provide low circumferential resolution while those having high m allow high circumferential resolution. On the other hand, every waves propagating in cylindrical coordinates should satisfy the following equation of momentum preservation;

$$k_\theta^r r = k_\theta^{r^*} r^* = \text{const} \quad (2.22)$$

for any arbitrary value of radial coordinate r and r^* . Therefore, k_θ increases to infinite value as wave becomes closer to the origin ($r=0$) unless $k_\theta=0$ as in the zeroth order scattering mode (this can be easily seen from fig. 2.4 (a) where the circumferential wavelength depicted as λ^r and λ^{r^*} become longer as r increases.) However, as explained previously, waves having too high k_θ are evanescent waves in general isotropic media. This results in the hollow zone near the origin where waves are evanescent and wave energy does not exist, as shown in fig. 2.4 (b-d). It can be seen

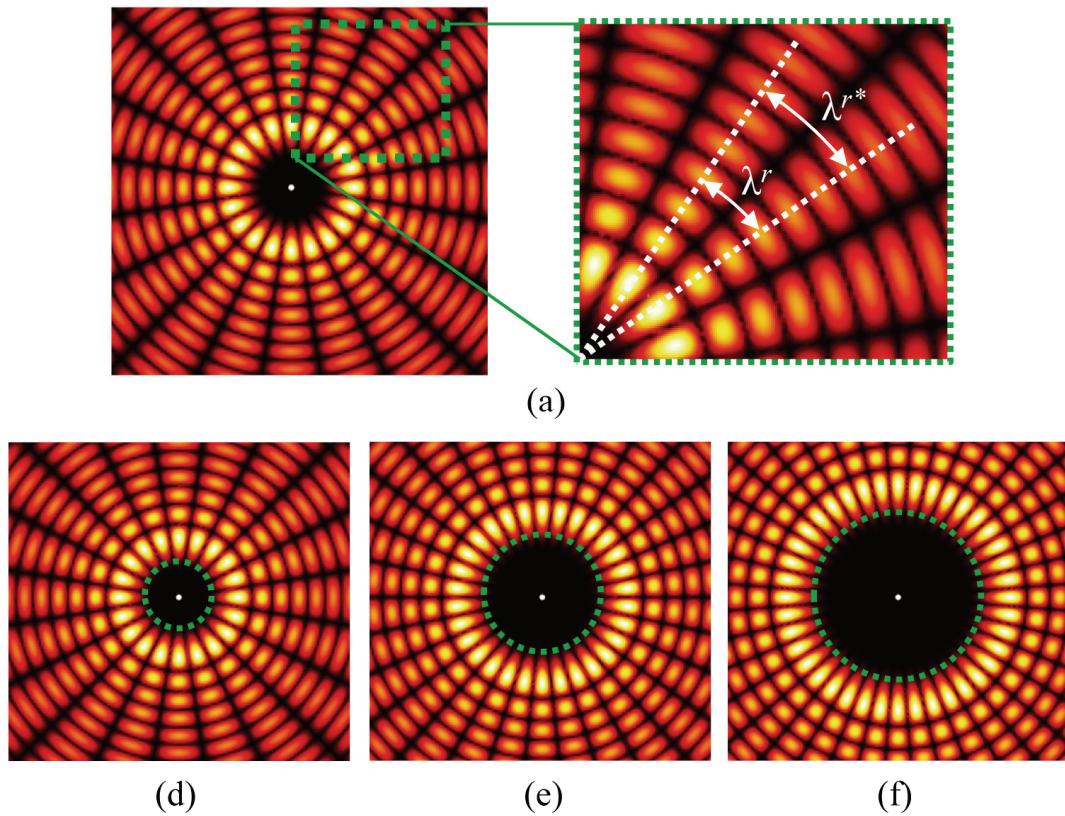


Fig. 2.4 (a) Plot of the wavelength at two different radial location, and plot of the hollow zone generated in the (b) 10th order, (c) 15th order and (d) 20th order scattering mode, respectively

from fig. 2.4 (b-d) that the radius of the hollow zone increases as the scattering order increases, due to the high k_θ value of the higher order scattering modes. As a result, incident wave components having high m , which corresponds to higher order scattering modes, should have lower interaction with the crack due to the larger hollow zone. This means that incident wave components having high m almost rarely affect overall imaging. Thus, only incident wave components that can provide low resolution dominantly affect overall imaging, resulting in diffraction limited measurement.

Although there exist many other explanation related to diffraction limit, its physical origin is unambiguous. The major reason of diffraction limit is that general medium cannot carry the waves having high k_θ values. As shown in this section, diffraction limit is originated from fundamental wave characteristics of general medium. Thus, it has been extremely hard to be overcome.

2.3 Physics behind sub-wavelength resolution by hyperlens

2.3.1 Hyperlens with hyperbolic EFC

If we only consider the materials having positive parameters, such as those existing in nature, the wave speeds along radial and circumferential directions in equation (2.15) should be real values. However, recent advances in metamaterial allow utilizing materials with negative parameters. By combining negative parameter with other positive parameter, the wave speeds in equation (2.15) can be imaginary value. For examples, since the wave speed of electromagnetic waves in material is defined as

$$c = \sqrt{\epsilon\mu}, \quad (2.23)$$

the wave speed becomes purely imaginary if

$$\epsilon < 0 \quad \text{and} \quad \mu > 0, \quad \text{or vice versa.} \quad (2.24)$$

Similarly, material having negative density ρ and positive bulk modulus K , or vice versa, shows imaginary acoustic wave speed, and material having negative density ρ and positive stiffness modulus (E or G , according to the wave's mode), or vice versa,

shows imaginary elastic wave speed.

The key in hyperlens is making material's circumferential wave speed imaginary by metamaterial. In this case, c_θ in equation (2.15) is purely imaginary and the wave dispersion relation of hyperlens can be expressed as

$$c_r^2 k_r^2 - |c_\theta^2| k_\theta^2 = \omega^2 . \quad (2.25)$$

Re-writing equation (2.25) with respect to k_r results in

$$k_r = \sqrt{\frac{\omega^2 + |c_\theta^2| k_\theta^2}{c_r^2}} . \quad (2.26)$$

In equation (2.26), the term inside square root is always positive for any value of k_θ . This indicate that for any value of k_θ , there always exist real-valued k_r , i.e., every waves having any value of k_θ is propagating wave in this type of materials. Unlike general medium, hyperlens can carry the waves having any value of k_θ . Thus, every information can be carried through hyperlens and diffraction limit can be overcome.

This point becomes clear if EFC of hyperlens and general medium is compared, as in fig. 2.5. If the dispersion relation of the hyperlens shown in equation (2.25) is plotted in (k_r, k_θ) plane, the result would be hyperbolic curve whose asymptotes are parallel to the k_θ axis, while circular curve is plotted for general isotropic media. In fact, the word 'hyperlens' is originated from its hyperbolic EFC. As previously shown, only the waves having k_θ between $-\hat{k}_\theta$ and \hat{k}_θ (which belongs to the yellow region) can propagate

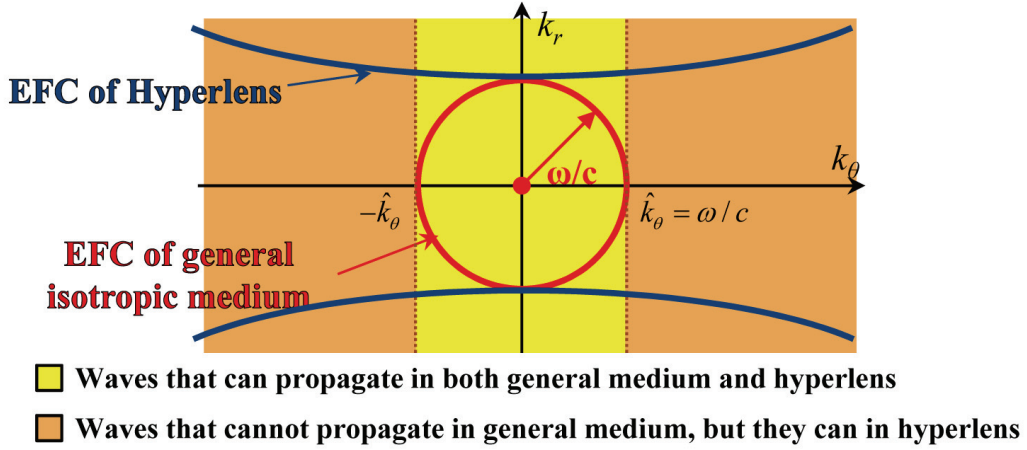


Fig. 2.5 EFC and internal wave characteristics of hyperlens with hyperbolic EFC

to far field in general isotropic medium. Waves having k_θ higher than \hat{k}_θ or lower than $-\hat{k}_\theta$ (which belongs to the orange region) cannot propagate through, resulting in diffraction-limited imaging. However, not only the waves belong to the yellow region but also those to the orange region can propagate through hyperlens since the contour of hyperlens is un-limited along k_θ axis. This can be summarized as follows;

$$k_r \text{ is purely real for both isotropic media and hyperlens if } -\omega/c = -\hat{k}_\theta < k_\theta < \hat{k}_\theta = \omega/c, \quad (2.27a)$$

$$k_r \text{ is purely real for hyperlens but purely imaginary for isotropic media if } k_\theta < -\hat{k}_\theta = -\omega/c \text{ or } k_\theta > \hat{k}_\theta = \omega/c. \quad (2.27b)$$

Thus, waves having extremely high k_θ , which contain extremely detailed circumferential information, can be measured at far field, resulting in theoretically unlimited imaging.

The operating principle of hyperlens can also be explained from the mode shape of scattering modes, as Jacob *et al.* [6] did in their work. As explained in the previous section, higher order scattering modes inevitably have hollow zones near the origin, which lower the interactions between crack and higher order scattering modes. In hyperlens, however, wave does not evanescent for any value of k_θ and hollow zones disappear. To see this effect, the scattering modes in equation (2.21) are re-calculated for hyperlens case. Since wave speed c is not constant value but having different value for different directions, it is convenient to re-write equation (2.21) by using equation (2.15) as

$$u = \left[\sum_{m=-\infty}^{m=\infty} U_m i^m J_m(kr) \exp(im\theta) \right] \exp(i\omega t) \quad (2.28)$$

where k is magnitude of wavevector which is defined as $k^2 = k_r^2 + k_\theta^2$. Unlike equation (2.21) which can be used for isotropic materials having constant c , equation (2.28) can be applied to more general materials, including metamaterials. From equation (2.28), it can be seen that the scattering order m is related to the angular wavelength along circumferential direction. As shown in fig. 2.4, the wavelength of m th order scattering mode along circumferential direction can be written as

$$\lambda^r = \frac{2\pi}{m} r \quad (2.29)$$

where the corresponding k_θ value is

$$k_\theta = \frac{2\pi}{\lambda^r} = \frac{m}{r}. \quad (2.30)$$

Substituting equation (2.30) into equation (2.26) yields

$$k_r^2 = \frac{\omega^2 + |c_\theta^2| k_\theta^2}{c_r^2} = \frac{\omega^2 r^2 + |c_\theta^2| m^2}{c_r^2 r^2}. \quad (2.31)$$

From equation (2.30) and (2.31), k of m th order scattering mode in any arbitrary point (x, y) in hyperlens can be expressed as

$$k = \sqrt{k_r^2 + k_\theta^2} = \sqrt{\frac{\omega^2(x^2 + y^2) + (c_r^2 + |c_\theta^2|)m^2}{c_r^2(x^2 + y^2)}}. \quad (2.32)$$

By substituting equation (2.32) to equation (2.28), mode shapes of scattering modes in hyperlens can be plotted. The calculated results are plotted in fig. 2.6. From fig. 2.6, although low order scattering modes in hyperlens such as $m = 0, 1$ and 2 (shown in fig.

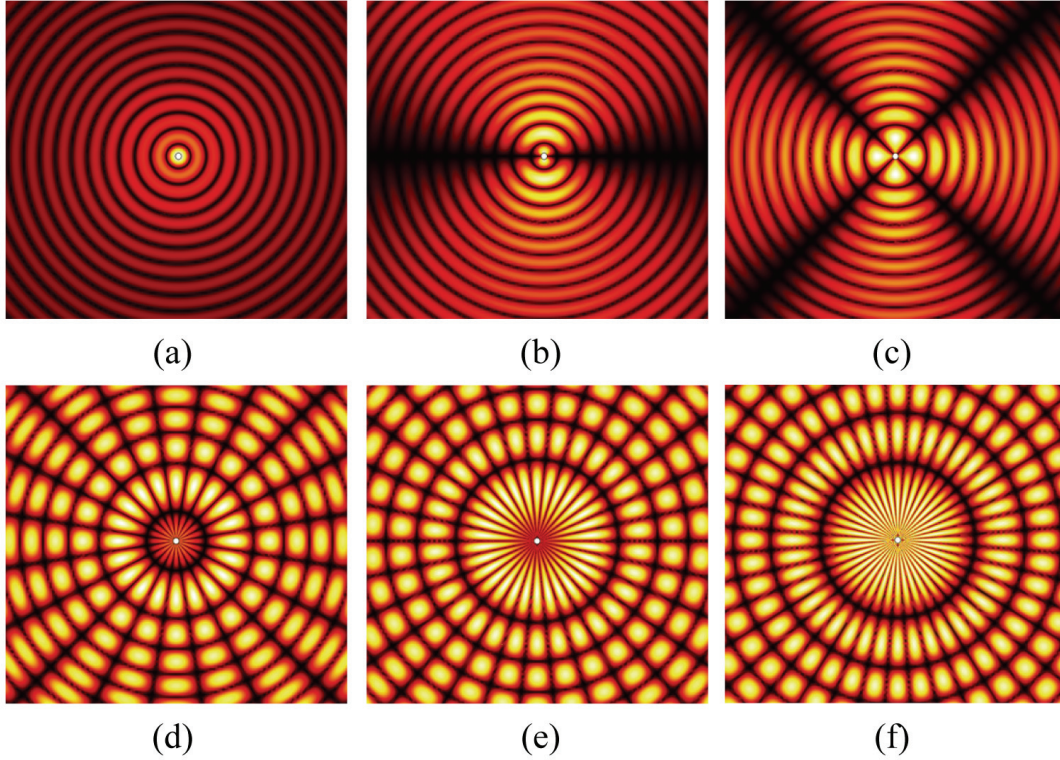


Fig. 2.6 Displacement plot of various scattering modes with the order of (a) 0, (b) 1, (c) 2, (d) 10, (e) 15 and (f) 20 at metamaterials having hyperbolic EFC

2.6 (a), (b) and (c) respectively) are almost same as those in isotropic media (shown in fig. 2.2 (a), (b) and (c) respectively), big differences can be observed between the waves having high order such as $m = 10, 15$ and 20 in hyperlens (shown in fig. 2.6 (d), (e) and (f) respectively) and in isotropic media (shown in fig. 2.2 (d), (e) and (f) respectively). In fig. 2.6 (d-f), it can be easily seen that the hollow zones which were observed for isotropic media case are disappeared. This indicates that in hyperlens, both low and high order scattering modes have very high interaction with the crack placed at the origin. Therefore, incident wave components having high m , which corresponds to higher order scattering modes, act as high-resolution probes that allow evaluation of the crack in more details and highly participate in imaging process.

Since it is clearly shown that waves which were evanescent wave in isotropic media can propagate in hyperlens, here rises another question: *‘by what mechanism do the evanescent waves still propagate after they pass through hyperlens?’*. To answer the question, image that evanescent wave incidents to the inner layer of hyperlens at point P and passes through the hyperlens at point P*, as shown in fig. 2.7 (a). At first, the evanescent wave has high k_θ that the isotropic media cannot carry the wave. Assume that the evanescent wave’s k_θ is k_θ^P at the point P, as in fig. 2.7 (b). At point P, the evanescent wave in the isotropic media is transmitted to the hyperlens while satisfying the proper boundary condition. To derive boundary condition at point P, incident wave from the actuator to the hyperlens is written as

$$u^{inc} = u_0^{inc} \exp(i\omega t - k_\xi^{iso} \xi - k_\eta^{iso} \eta) \quad (2.33)$$

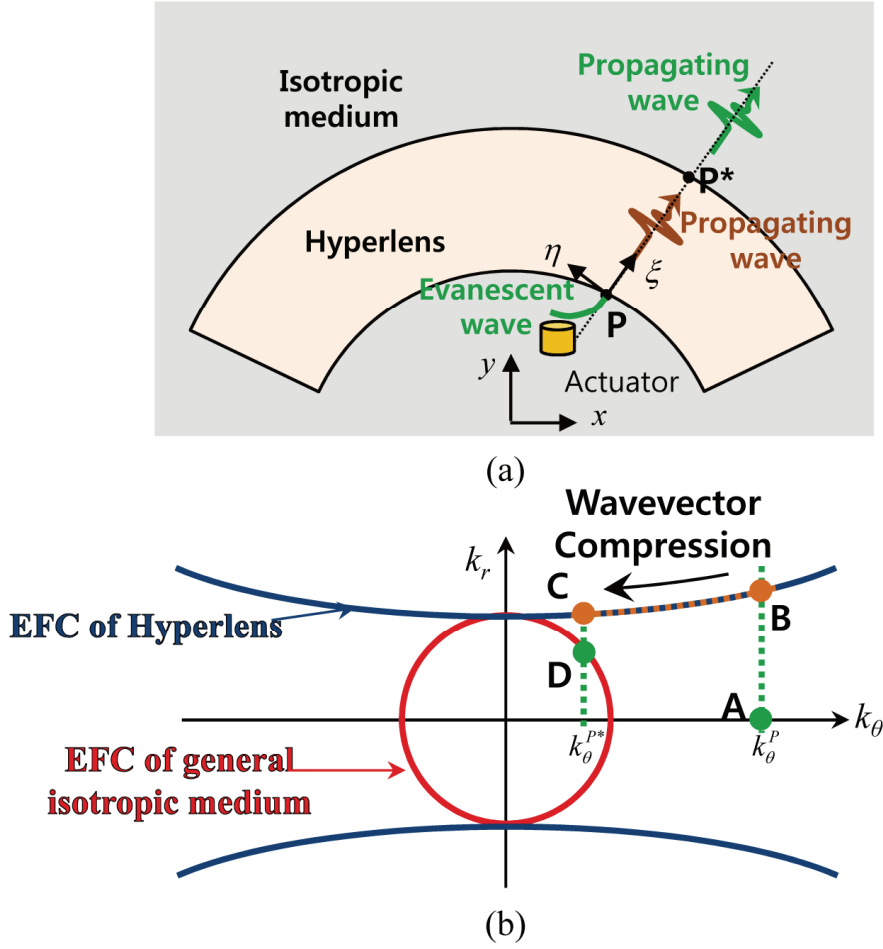


Fig. 2.7 (a) Wave propagating characteristics of evanescent wave incident at inner circle of hyperlens, (b) schematic illustration of wavevector compression inside the hyperlens

where ξ and η denote the normal and tangential direction at point P as illustrated in fig. 2.7 (a). Also, the superscripted *iso* indicate that the wavevector is defined in the isotropic material in fig. 2.7 (a). Accordingly, reflected and transmitted waves at the boundary are written as

$$u^{ref} = u_0^{ref} \exp(i\omega t + k_\xi^{iso} \xi - k_\eta^{iso} \eta) , \quad (2.34a)$$

$$u^{trans} = u_0^{trans} \exp(i\omega t - k_{\xi}^{hyp} \xi - k_{\eta}^{hyp} \eta) . \quad (2.34b)$$

In equation (2.34b), the superscripted *hyp* indicate that the wavevector is defined in the hyperlens. From equation (2.33) and (2.34), the total displacement at point P (where $\xi = 0$) in the isotropic media and hyperlens can be expressed as

$$\text{in isotropic media : } u_0^{inc} \exp(i\omega t - k_{\eta}^{iso} \eta) + u_0^{ref} \exp(i\omega t - k_{\eta}^{iso} \eta), \quad (2.35a)$$

$$\text{in hyperlens : } u_0^{trans} \exp(i\omega t - k_{\eta}^{hyp} \eta) . \quad (2.35b)$$

Now, considering the displacement continuity at point P, the following equation should be satisfied.

$$u_0^{inc} \exp(i\omega t - k_{\eta}^{iso} \eta) + u_0^{ref} \exp(i\omega t - k_{\eta}^{iso} \eta) = u_0^{trans} \exp(i\omega t - k_{\eta}^{hyp} \eta) . \quad (2.36)$$

Since equation (2.36) should be satisfied for all t and η , both exponential terms in left and right sides of equation (2.36) should be identical as

$$i\omega t - k_{\eta}^{iso} \eta = \omega t - k_{\eta}^{hyp} \eta \text{ for all } t \text{ and } \eta . \quad (2.37)$$

Therefore, the following boundary condition can be derived [41];

$$k_{\eta}^{iso} = k_{\eta}^{hyp} . \quad (2.38)$$

For cylindrical arranged hyperlens, η is same as θ everywhere in the hyperlens-isotropic media interfaces. Therefore, the transmitted wave inside the hyperlens has the wavevector (k_r, k_{θ}) corresponding to the point B in fig. 2.7 (b).

After the transmission, wave becomes propagating wave and propagates from point P to P* in fig. 2.7 (a). During the propagation, since none of the wave energy is added or dissipated, the momentum of the wave should be maintained, i.e., equation (2.22) should

be satisfied. Equation (2.22) indicates that k_θ should be reduced as wave propagates through radial direction, which is called wavevector compression. Due to wavevector compression, k_θ is reduced from k_θ^P to $k_\theta^{P^*}$ as

$$k_\theta^{P^*} = \frac{k_\theta^P r^P}{r^{P^*}} \quad (2.39)$$

at the wave reach to the point P*, and the wavevector (k_r, k_θ) becomes that corresponds to the point C in fig. 2.7 (b). As a result, at point P*, k_θ became small enough to be carried by the isotropic media, resulting in the propagating wave which has wavevector (k_r, k_θ) corresponding to the point D in fig. 2.7 (b).

From the above discussion, it is clear that evanescent waves passing through the hyperlens can become propagating waves due to wavevector compression. It should be noted that wavevector compression is not a unique characteristic of hyperlens. Any lens having cylindrical configuration may exhibit wavevector compression phenomenon. In fact, wavevector compression phenomenon has been also applied to superlens to overcome its weak point – sub-wavelength resolution is only possible in near-field. The idea, called far field superlens, was first proposed by Durant *et al.* [42], and realized by Liu *et al.* [43, 44]. Xiong *et al.* [45] developed tunable far field superlens. These far field superlenses allowed far field sub-wavelength resolution but based on the different operating principle compared to hyperlens.

Finally, the issue related to realization of the metamaterial having hyperbolic EFC, called

hyperbolic metamaterial, is addressed. As shown in equation (2.25), hyperbolic metamaterial can be achieved by the material having imaginary wave speed along circumferential direction while real-valued wave speed along radial direction. This requires not only negative parameter but also anisotropy along circumferential and radial direction. Focusing on electromagnetic wave, wave speed of transverse-magnetic waves can be written as

$$c_r = \frac{1}{\sqrt{\mu_0 \varepsilon_0 \varepsilon_\theta}}, \quad c_\theta = \frac{1}{\sqrt{\mu_0 \varepsilon_0 \varepsilon_r}} \quad (2.39)$$

while μ_0 and ε_0 denote permeability and permittivity of air. ε_r and ε_θ denote permittivity of media along radial and circumferential direction, respectively. Thus, to obtain hyperbolic metamaterial, $\varepsilon_\theta > 0$ and $\varepsilon_r < 0$ is required. For electromagnetic wave, negative permittivity can be easily obtained from thin silver layer exhibiting electromagnetic plasmonic resonance. From the metamaterial having negative permittivity, anisotropy is obtained by radially or circumferentially arranged metamaterial-general media composite structure, as shown in fig. 2.8. In fig. 2.8, the width of each layer is much smaller than operating wavelength so the overall composite structure can be regarded as homogenous material. By this structure, hyperbolic electromagnetic metamaterials have been successfully realized.

On the other hand, it is very hard to obtain material having hyperbolic EFC for acoustic/elastic waves. The most critical problem in realizing hyperbolic acoustic/elastic metamaterial is that material exhibiting imaginary wave speed is extremely hard to be obtained for acoustic/elastic wave. Accordingly, the previous realization on

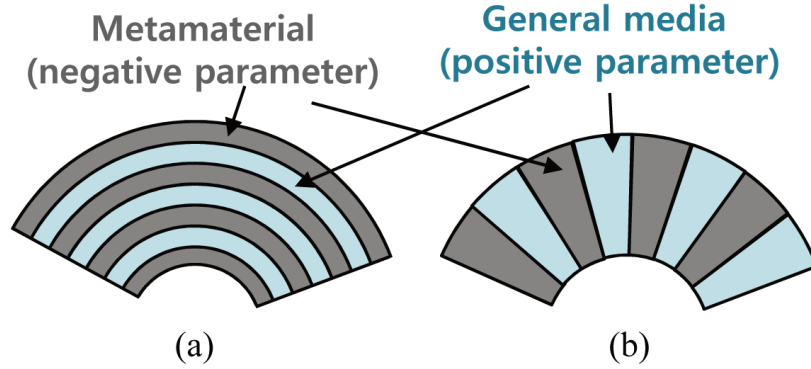


Fig. 2.8 Two representative composite structure with (a) radially and (b) circumferentially arranged layered structure for realization of hyperlens

acoustic/elastic hyperlens have been relied on the elliptic metamaterial, which will be studied in the following section.

2.3.2 Hyperlens with elliptic EFC

Although hyperbolic metamaterial allows theoretically un-limited resolution, it is very hard to be realized in acoustic/elastic waves. As an alternative, elliptic metamaterial which has strongly elliptic EFC has been used for acoustic/elastic hyperlens. Unlike hyperbolic metamaterial which is based on imaginary circumferential wave speed, elliptic metamaterial achieve sub-wavelength resolution by extremely slow circumferential wave speed such that $c \gg c_\theta$ while c denotes wave speed of the environment where hyperlens is embedded. To see the effect of the extremely slow wave, dispersion relation in equation (2.15) is re-written with respect to the k_r as following;

$$k_r = \sqrt{\frac{\omega^2}{c_r^2} - \frac{c_\theta^2}{c_r^2} k_\theta^2} . \quad (2.40)$$

Here, both c_r and c_θ are real value, unlike in hyperbolic metamaterial of which c_θ is purely imaginary. From equation (2.40), it can be seen that k_r is purely imaginary if

$$k_\theta > \omega / c_\theta \text{ or } k_\theta < -\omega / c_\theta . \quad (2.41)$$

Thus, waves having k_θ higher than ω / c_θ should have imaginary k_r and become evanescent waves. Comparing maximum k_θ value of the propagating waves in elliptic metamaterial (which is ω / c_θ) with that in general isotropic media (which is ω / c), it can be seen that elliptic metamaterial can carry waves having higher k_θ since $c \gg c_\theta$. Thus, several high order scattering modes which are evanescent waves in isotropic media can propagate to far field in elliptic metamaterial. This can provide resolution higher than diffraction limit. However, hyperlens based on elliptic metamaterial has obvious resolution limit – very high order scattering modes having k_θ higher than ω / c_θ are evanescent waves and their information cannot be retrieved at far field.

The EFC of elliptic metamaterial clearly show the resolution limit, too. Generally, radial wave speed c_r of elliptic metamaterial is set to be almost same as the wave speed of external media, due to several issues such as impedance problem. Thus, shape of elliptic metamaterial's EFC is generally elliptic, as can be predicted from equation (2.40). Fig. 2.9 shows EFC's of elliptic metamaterial and general isotropic media. In fig. 2.9, only waves having k_θ between $-\hat{k}_\theta$ and \hat{k}_θ (which belongs to the yellow region) can

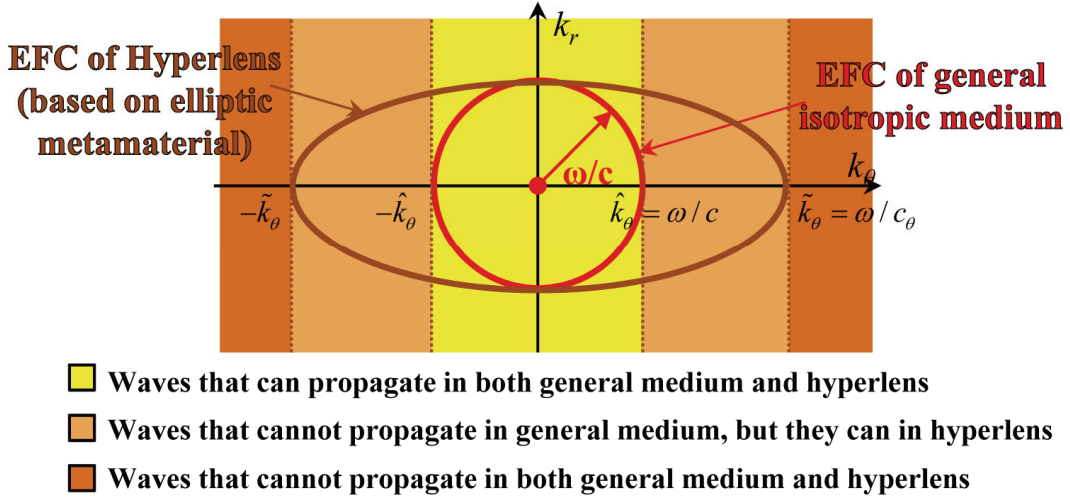


Fig. 2.9 EFC and internal wave characteristics of the hyperlens with elliptic EFC

propagate to far field in general isotropic medium. However, in hyperlens based on elliptic metamaterial, waves having k_θ between $-\tilde{k}_\theta$ and $-\hat{k}_\theta$ or between \hat{k}_θ and \tilde{k}_θ (which belongs to the orange region) can additionally propagate to far field. Nevertheless, waves having k_θ lower than $-\tilde{k}_\theta$ or higher than \tilde{k}_θ (which belongs to the dark orange region) cannot propagate through both hyperlens and isotropic media since there are no contour existing inside the region. This point can be summarized as

$$k_r \text{ is purely real for both isotropic media and elliptic EFC if } \quad (2.42a)$$

$$-\omega/c = -\hat{k}_\theta < k_\theta < \hat{k}_\theta = \omega/c$$

$$k_r \text{ is purely real for elliptic EFC but purely imaginary for isotropic media if } \quad (2.42b)$$

$$-\omega/c_0 = -\tilde{k}_\theta < k_\theta < -\hat{k}_\theta = -\omega/c \text{ or } \omega/c = \hat{k}_\theta < k_\theta < \tilde{k}_\theta = \omega/c_0$$

$$k_r \text{ is purely imaginary for both isotropic media and elliptic EFC if } \quad (2.42c)$$

$$k_\theta < -\tilde{k}_\theta = -\omega/c_0 \text{ or } k_\theta > \tilde{k}_\theta = \omega/c_0$$

The existence of non-propagating region in EFC indicates that perfect imaging cannot be achieved by hyperlens based on elliptic metamaterial. On the other word, hyperlens based on elliptic metamaterial can provide resolution higher than diffraction limit, but it still suffer from certain resolution limit. Generally, hyperlens based on elliptic metamaterial has low performance compared to that based on hyperbolic metamaterial [46].

In addition, the mode shapes of scattering modes in hyperlens with elliptic EFC are calculated. Considering k_θ value of m th order scattering mode in equation (2.29), equation (2.40) can be re-written as

$$k_r^2 = \frac{\omega^2}{c_r^2} - \frac{c_\theta^2}{c_r^2} k_\theta^2 = \frac{\omega^2}{c_r^2} - \frac{c_\theta^2 m^2}{c_r^2 r^2}. \quad (2.43)$$

Thus, k of m th order scattering mode in any arbitrary point (x, y) in hyperlens with elliptic EFC can be expressed as

$$k = \sqrt{k_r^2 + k_\theta^2} = \sqrt{\frac{\omega^2}{c_r^2} - \left(\frac{c_\theta^2}{c_r^2} + 1\right) \frac{m^2}{(x^2 + y^2)}}. \quad (2.44)$$

Substituting equation (2.44) to equation (2.28) yields the mode shapes of scattering modes in hyperlens with elliptic EFC. These mode shapes of scattering modes in elliptic metamaterial are illustrated in fig. 2.10. As those in hyperbolic metamaterials plotted in fig. 2.6, low order scattering modes in elliptic metamaterial are almost same as those in isotropic media. On the other hand, for the high order scattering modes plotted in fig. 2.10 (d-f), correspond to $m = 10, 15$ and 20 , the hollow zone around the origin which were significant in isotropic media become reduced while they still exist for very high

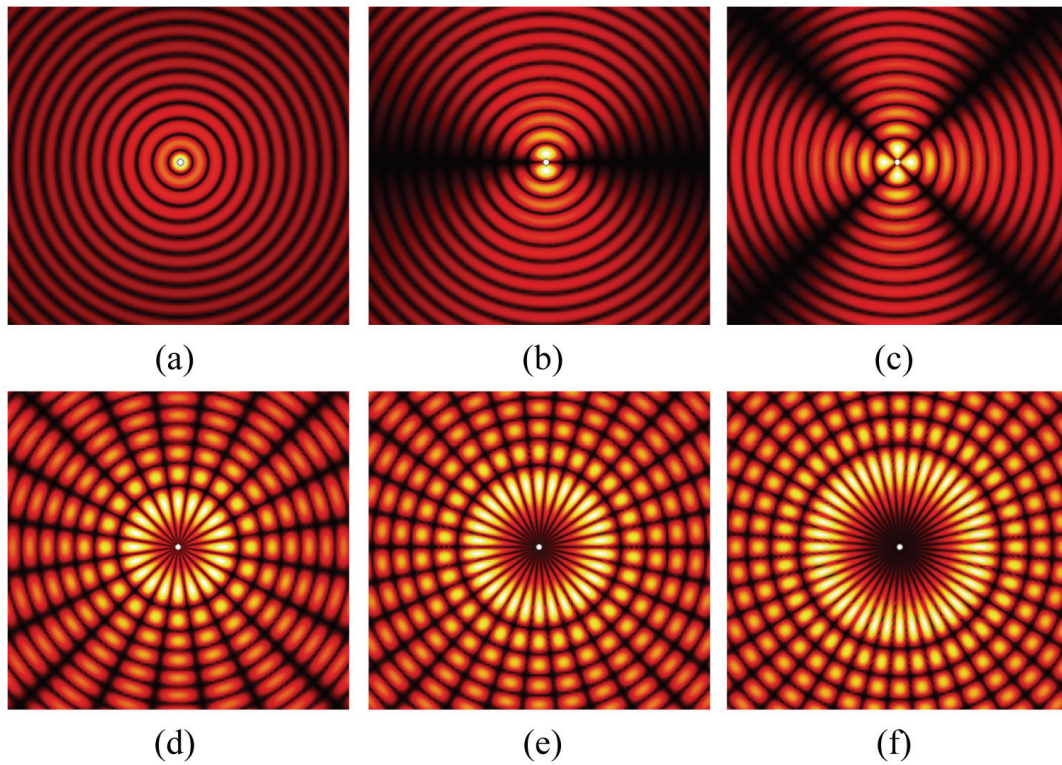


Fig. 2.10 Displacement plot of various scattering modes with the order of (a) 0, (b) 1, (c) 2, (d) 10, (e) 15 and (f) 20 at metamaterials having elliptic EFC

order scattering mode (as in fig. 2.10 (f)). The reduction of hollow zone indicates that the high order scattering modes in elliptic metamaterial have more strong interaction with the central crack than those in isotropic media. However, the interaction is much weaker than those in hyperbolic metamaterial in which hollow zones are disappeared. Thus, incident wave components having high m , corresponding to high order scattering modes, better participate imaging than those in general isotropic media, but still their participation is lower than that in hyperlens with hyperbolic EFC. This investigation also support that elliptic metamaterial may show sub-wavelength resolution but its performance is degraded compared to hyperbolic metamaterial.

As demonstrated in the above discussions, any material having slower wave speed along the circumferential direction than external material can exhibit sub-wavelength resolution. However, since wave speed difference of materials existing in nature is not very significant, resolution improvement would be too small if general material is used for this purpose. Therefore, artificially made metamaterials having extremely slow wave speed along the circumferential direction have been designed for acoustic/elastic hyperlens. These metamaterials were made by circumferentially arrayed (as shown in fig. 2.8 (b)) solid-fluid composite structures – brass-air structure was used for acoustic hyperlens [36] and aluminum-air structure was used for elastic hyperlens [8]. Due to the extreme difference of wave speed between solid and fluid, extremely anisotropic metamaterial having very slow circumferential wave speed have been realized. For example, the previously proposed hyperlens consists of aluminum-air structure and effective material properties can be calculated as [8]

$$C_{\theta\theta}^{eff} = \left(\frac{\bar{V}^{al}}{C_{\theta\theta}^{al}} + \frac{\bar{V}^{air}}{C_{\theta\theta}^{air}} \right)^{-1}, \quad (2.45a)$$

$$C_{rr}^{eff} = \left(\bar{V}^{al} C_{rr}^{al} + \bar{V}^{air} C_{rr}^{air} \right) - \left(\bar{V}^{al} \frac{(C_{r\theta}^{al})^2}{C_{\theta\theta}^{al}} + \bar{V}^{air} \frac{(C_{r\theta}^{air})^2}{C_{\theta\theta}^{air}} \right) + \frac{(C^*)^2}{C_{\theta\theta}^{eff}}, \quad (2.45b)$$

$$C^* = \left(\bar{V}^{al} \frac{C_{r\theta}^{al}}{C_{\theta\theta}^{al}} + \bar{V}^{air} \frac{C_{r\theta}^{air}}{C_{\theta\theta}^{air}} \right) C_{\theta\theta}^{eff}, \quad (2.45c)$$

$$\rho^{eff} = \bar{V}^{al} \rho^{al} + \bar{V}^{air} \rho^{air}, \quad (2.45d)$$

where $C_{\theta\theta}$ and C_{rr} denote stiffness along circumferential and radial direction and ρ is density. Here, wave speed along circumferential and radial direction are defined as

$c_\theta = \sqrt{C_{\theta\theta} / \rho}$ and $c_r = \sqrt{C_{rr} / \rho}$, respectively. Also, \bar{V}^{al} and \bar{V}^{air} denote volume fraction of aluminum and air, respectively. From equation (2.45), wave speed are calculated as $c_r = 5130$ m/s and $c_\theta = 15$ m/s at 100 kHz, showing that the hyperlens is elliptic. Since none of the parameters in equation (2.45) are negative, the previously proposed hyperlens had elliptic EFC. Therefore, these lenses were proven to show sub-wavelength resolution, but they suffer from theoretical resolution limit, as discussed previously.

Chapter 3.

Proposition of new elastic hyperlens based on hyperbolic elastic metamaterial

3.1 Chapter overview

As discussed in the previous chapter, major problems in the previously proposed elastic hyperlens is that it is based on elliptic metamaterial. Since elliptic metamaterial inevitably suffer from certain resolution limit, the previously proposed elastic hyperlens had degraded imaging performance, compared to those in electromagnetic hyperlenses. To overcome the problem and develop a new hyperlens having much higher resolution, therefore, it is essential to design new hyperbolic elastic metamaterial. In this chapter, design issues related to the hyperbolic elastic metamaterial is revealed. In addition, new hyperbolic elastic metamaterial which is tailored for hyperlens application is engineered. By numerical simulation, hyperbolic characteristics of the proposed metamaterial are verified, and its performance of sub-wavelength resolution is shown.

The major problem in proposing new hyperbolic elastic metamaterial is that none of the previously proposed elastic metamaterials is proper for hyperlens application. To achieve hyperbolic metamaterial, imaginary wave speed is essential, i.e., material in which wave cannot propagate circumferentially is required. Generally, materials having imaginary wave speed have been realized by resonance-based metamaterial or phononic band-gap

structures. Resonance-based metamaterial utilize internal-resonance to prohibit wave propagation at certain frequency range. At resonance frequency, internal resonance system absorbs all of wave's energy while the system undergoes resonance and waves cannot propagate at the frequency around the resonance. This type of metamaterial was shown by Liu *et al.* [47]. Liu *et al.* [48] analytically investigated resonance-based metamaterial and Fang *et al.* [49] studied membrane type metamaterial that exhibit negative modulus. Yang *et al.* [50] showed that negative mass can also be achieved by resonance-based metamaterial. In addition, Lee *et al.* [51] and Lai *et al.* [52] showed that metamaterials having simultaneously negative density and modulus can be achieved by resonance-based metamaterial. On the other hand, phononic band-gap structure utilizes periodicity to prohibit wave propagation. For researches related to band-gap phenomena in phononic crystals, see previous researches done by Kushwaha *et al.* [53] and Sigalas *et al.* [54]. However, these metamaterials are not proper for hyperlens applications; the reason is explained in the following section. Thus, new hyperbolic elastic metamaterial should be designed for this research.

After the hyperbolic elastic metamaterials and hyperlens are designed, their wave characteristics such as EFC are calculated by numerical method. Since metamaterial consists of unit cells which is small enough to be considered as homogeneous medium, its effective wave characteristics should be evaluated by proper method. Here, finite element method is formulated and applied in EFC calculation. In addition, capability of sub-wavelength resolution of the proposed hyperlens is verified by numerical simulation, and its performance is compared to that of the previously proposed elastic hyperlens

which is based on elliptic metamaterial.

3.2 Design of hyperbolic elastic metamaterial and hyperlens

3.2.1 Design requirements of proposed hyperbolic elastic metamaterial

Regarding that possible applications of hyperlens is elastic wave based imaging (such as NDE), the proposed hyperlens should satisfy not only capability of sub-wavelength resolution but also additional requirements. Design requirements that the proposed hyperbolic elastic metamaterial and hyperlens should satisfy can be summarized as follows; 1. Exhibiting hyperbolic EFC, 2. Wide operating frequency range with low loss, 3. Low scattering for imaging purpose, 4. Various design variables.

- **Exhibiting hyperbolic EFC**

Although both elliptic and hyperbolic EFC can provide sub-wavelength resolution at far field, hyperbolic EFC is much preferable since it has theoretically un-limited resolution. The hyperbolic EFC indicates that waves in the material can propagate through radial direction but cannot through circumferential direction. This requirement is the most important one since it is the key in much higher resolution in elastic hyperlens, as shown in chapter 2. Note that hyperbolic EFC cannot be obtained in nature, and artificially made hyperbolic metamaterial is required.

One may think that hyperbolic EFC can be easily obtained by imposing several fluid slits along the circumferential direction to forbid elastic wave propagation. However, as shown in previous work [8], hyperbolic EFC cannot be obtained in that way since wave can propagate from solid to fluid or vice versa by solid-fluid interaction. Although the transmission is very low, it cannot be said that wave ‘cannot’ propagate through circumferential direction. Strictly speaking, the structure simply having periodically arranged solid-fluid layers are elliptic metamaterial. Also, one may think that using shear wave mode to periodically arranged solid-fluid layered structure can exhibit hyperbolic EFC, since fluid has zero shear modulus. For this case, however, the structure cannot be seen as hyperlens. The structure is rather wave imaging device having multiple waveguide channel. The resolution of such device is affected by the number and width of aluminum layer, while resolution of hyperlens is affected by its EFC, not by them.

- **Wide operating frequency range with low loss**

Generally, elastic wave based imaging uses pulse-type signal, which consists of various frequency components. Thus, if operating frequency of hyperlens is too narrow, it cannot be effectively used in elastic wave based imaging. Also, if hyperlens suffer from high loss, its possible application would be very narrow. Considering the practical application of elastic hyperlens, the requirement of wide operating frequency range and low loss is essential.

In this point, it can be figured out that previously proposed resonance-based elastic metamaterials are not proper in the hyperlens applications. Since resonance-based metamaterials are based on the wave's energy absorption by internal resonance system at resonance frequency, the prohibition of wave propagation can only be observed at very narrow frequency range around the resonance frequency. Moreover, if there's any loss in the system, the resonance frequency can be shifted [55]. This means that robustness of the system is very low for resonance-based metamaterial. Also, resonance-based elastic metamaterials have very high energy dissipation around resonance frequency, which makes it harder to be used for hyperlens. To see the relation between internal resonance and energy dissipation, see Ref. [56] which studied extremely high energy dissipation at internal resonance frequency. As a result, the resonance-based metamaterial should be avoided in hyperlens engineering.

- **Low scattering for imaging purpose**

If the microstructure forming metamaterial is sufficiently small, the metamaterial can be treated as a homogeneous media. However, if scale of the microstructure is comparable to the operating wavelength, the metamaterial cannot be treated as a homogeneous media. For this case, scattering becomes dominant. Thus, if unit cell of proposed hyperlens is not sufficiently small, the imaging information will be scattered into various directions, which is certainly undesirable in wave based imaging. Therefore, to avoid the problem related to scattering, unit cell of proposed hyperbolic elastic metamaterial should be very

small compared to the operating wavelength.

This is why general phononic crystals cannot be applied to hyperlens. Usually, size of unit cell in general phononic crystal is comparable to that of the operating wavelength, and scattering dominantly takes place inside the phononic crystal. The scattering issue can be clearly seen from fig. 3.1 in which ‘bi-refraction phenomena’ in phononic crystal is plotted. Since scattering is dominant inside phononic crystal, waves inside the phononic crystal can be transmitted along various directions as they pass through the phononic crystal. In fig. 3.1, it can be seen that the single incident wave is refracted along two directions as the wave pass through the phononic crystal prism. Note that two

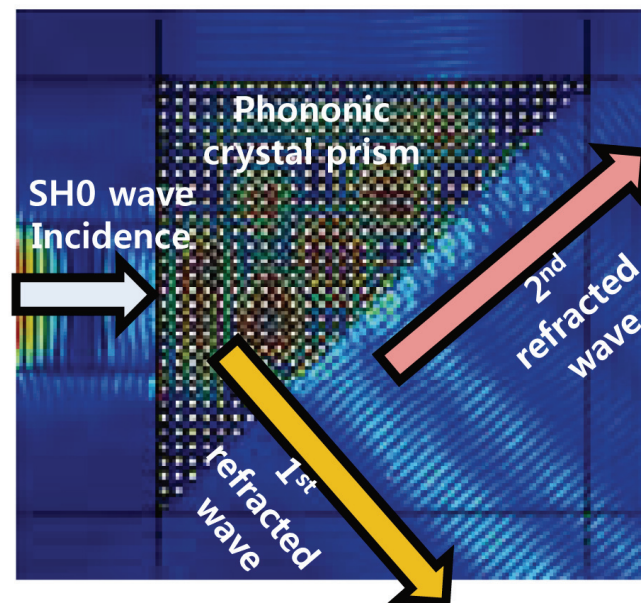


Fig. 3.1 Plot of Von-Mises stress at phononic crystal prism exhibiting bi-refraction phenomenon

refracted waves have exactly same mode and frequency. Although transmitted waves have only two dominant directions in fig. 3.1, theoretically transmitted waves can propagate through more than two directions if the angle of prism is changed. The bi-refraction phenomenon in fig. 3.1 clearly shows why phononic crystal should be avoided in hyperlens engineering.

- **Various design variables**

This requirement is actually not essential, but it could facilitate any further improvement of the proposed hyperlens. For example, the only design parameter in the previously proposed elastic hyperlens [8] was volume fraction, which makes it hard to engineering its performance. For newly-proposed elastic hyperlens, various design parameters are preferred.

If these requirements are met, the newly proposed hyperlens may show much improved performance compared to the previous hyperlenses.

3.2.2. How to obtain the desired hyperbolic elastic metamaterial?

From the design requirements previously shown, the way to design desired hyperbolic elastic metamaterial is investigated. To show how the desired hyperbolic elastic metamaterial can be realized, first let's consider general periodic mass-spring system shown in fig. 3.2 (a). Note that this mass-spring system is usually considered for wave motions inside general phononic crystals. The system in fig. 3.2 (a) can be viewed as 1

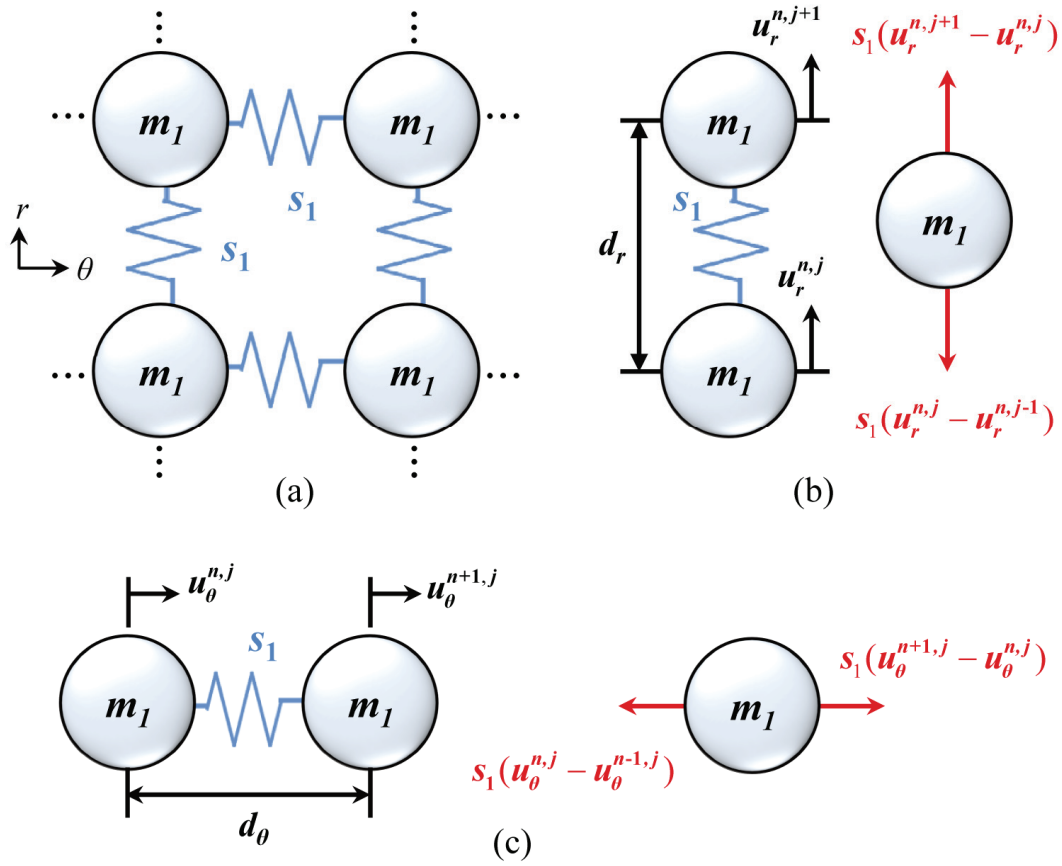


Fig. 3.2 (a) Schematic diagram of mass-spring system for general phononic crystal, and free-body diagrams along (b) radial direction and (c) circumferential direction

dimensional mass-spring system along radial and circumferential direction. Considering mass-spring motion along radial direction, shown in fig. 3.2 (b), the equation of the motion m_1 along radial direction can be written as

$$m_1 \ddot{u}_r^{n,j} = s_1(u_r^{n,j+1} - u_r^{n,j}) - s_1(u_r^{n,j} - u_r^{n,j-1}). \quad (3.1)$$

In equation (3.1), since mass-spring system is periodically arranged, periodic wave solution can be assumed for the displacement field u_r . The assumption of periodic wave solution can be written as following

$$u_r^{n,j} = U_r \exp[i(\omega t - k_r r)]. \quad (3.2)$$

In equation (3.2), it might be strange that assuming periodic wave solution is actually same form as assuming time-harmonic wave solution. In fact, the key in assuming periodic wave solution lies in the assumption of no-reflection condition. Suppose wave incident in n th unit cell. Since unit cell is periodically arranged, the transmitted wave from n th unit cell is same as the incident wave in $(n+1)$ th unit cell. However, since all unit cells should have same physics, the incident wave in $(n+1)$ th unit cell should be same as that in n th unit cell. Thus, reflection in the unit cell can be ignored in periodic wave solution, and only waves propagating through single direction (in equation (3.2), positive circumferential direction) is considered.

Assuming the periodic wave solution given in equation (3.2), $u_r^{n,j}$ can be assumed as $u_r^{n,j} = U_r \exp[i(\omega t - k_r r)]$, and $u_r^{n,j+1}$ and $u_r^{n,j-1}$ can be expressed as

$$u_r^{n,j+1} = \exp(-ik_r d_r) u_r^{n,j}, \quad (3.3a)$$

$$u_r^{n,j-1} = \exp(ik_r d_r) u_r^{n,j}. \quad (3.3b)$$

Substituting the assumption to equation (3.1), the following equation can be derived.

$$\begin{aligned} -m_1 \omega^2 &= s_1 (\exp(-ik_r d_r) - 1) - s_1 (1 - \exp(ik_r d_r)) \\ &= s_1 (\exp(-ik_r d_r) + \exp(ik_r d_r)) - 2s_1 \end{aligned} \quad (3.4)$$

Since $2 \cos x = \exp(-ix) + \exp(ix)$, the dispersion relation can be written as

$$-m_1 \omega^2 = 2s_1 \cos(k_r d_r) - 2s_1 \quad (3.5)$$

or, arranging with respect to k_r ,

$$\cos(k_r d_r) = \frac{2s_1 - m_1 \omega^2}{2s_1} . \quad (3.6)$$

In same manner, considering mass-spring motion along circumferential direction shown in fig. 3.2 (c), the equation of the motion m_1 along circumferential direction is

$$m_1 \ddot{u}_\theta^{n,j} = s_1 (u_\theta^{n+1,j} - u_\theta^{n,j}) - s_1 (u_\theta^{n,j} - u_\theta^{n-1,j}) . \quad (3.7)$$

Along circumferential direction, periodic wave solution can be assumed as

$$u_\theta^{n,j} = U_\theta \exp[i(\omega t - k_\theta \theta)] , \quad (3.8)$$

and accordingly

$$u_\theta^{n+1,j} = \exp(-ik_\theta d_\theta) u_\theta^{n,j} , \quad (3.9a)$$

$$u_\theta^{n-1,j} = \exp(ik_\theta d_\theta) u_\theta^{n,j} . \quad (3.9b)$$

Therefore, equation (3.7) can be re-written as

$$\begin{aligned} -m_1 \omega^2 &= s_1 (\exp(-ik_\theta d_\theta) - 1) - s_1 (1 - \exp(ik_\theta d_\theta)) \\ &= s_1 (\exp(-ik_\theta d_\theta) + \exp(ik_\theta d_\theta)) - 2s_1 = 2s_1 \cos(k_\theta d_\theta) - 2s_1 . \end{aligned} \quad (3.10)$$

Re-arranging equation (3.10) with respect to k_θ results in

$$\cos(k_\theta d_\theta) = \frac{2s_1 - m_1 \omega^2}{2s_1} . \quad (3.11)$$

From equation (3.6) and equation (3.11), it can be seen that $k_r d_r$ and $k_\theta d_\theta$ should be imaginary value for certain frequency ranges where

$$\frac{2s_1 - m_1 \omega^2}{2s_1} > 1 \quad \text{or} \quad \frac{2s_1 - m_1 \omega^2}{2s_1} < -1 . \quad (3.12)$$

However, since $m_1 \omega^2$ is positive value, first condition cannot be satisfied. Thus, only

second condition is considered, and waves propagating inside the periodic structure shown in fig. 3.2 (a) should have imaginary $k_r d_r$ and $k_\theta d_\theta$ for frequencies of

$$m_1 \omega^2 > 4s_1, \quad \omega > 2\sqrt{\frac{s_1}{m_1}}. \quad (3.13)$$

Thus, wave propagation above the frequency given in equation (3.13) should have imaginary wave speed in periodic structure.

In fact, this is physical origin of the formation of band-gap in periodic phononic crystals of which equivalent mass and spring coefficients are m_1 and s_1 , respectively. However, as previously explained, phononic crystals cannot be used in this work since imaginary wave speed is usually achieved in high frequency ranges where wavelength of external materials are comparable to the unit cell size d_r and d_θ . To clearly explain the frequency issue in phononic crystals, wave dispersion relation in general homogeneous material is expressed in the form of mass-spring system shown in fig. 3.2 (a). Since periodicity d_r and d_θ can be considered as zero for general homogeneous material, equation (3.6) and equation (3.11) can be simplified by using assumption $\cos x \approx 1 - x^2 / 2$ for $x \ll 1$ as

$$\cos(kd) \approx 1 - \frac{k^2 d^2}{2} = \frac{2s - m\omega^2}{2s}. \quad (3.14)$$

where variables in equation (3.14) are corresponding to general homogeneous material.

Re-writing equation (3.14) with respect to k results in

$$k = \sqrt{\frac{m}{s}} \frac{\omega}{d}. \quad (3.15)$$

Note that $\sqrt{m/s} = d/c$ where c is wave speed of material. Substituting equation (3.13) and (3.15) shows that wavelength at the frequency where wave speed starts to be imaginary value is

$$k_{\xi} = 2\sqrt{\frac{ms_1}{m_1s}} \frac{1}{d} = 2\sqrt{\frac{c_{\xi}}{c}} \frac{d}{d_{\xi}} \frac{1}{d}. \quad (3.16)$$

where ξ indicates r or θ depending on the considered direction. Here, usually wave speed in general phononic crystals at low frequencies c_{ξ} has same order of magnitude as wave speed in matrix. Thus, equation (3.16) can be approximated as

$$k_{\xi} \sim \frac{2}{d_{\xi}}, \quad (3.17)$$

and corresponding wavelength is

$$\lambda_{\xi} = \frac{2\pi}{k_{\xi}} \sim \pi d_{\xi}. \quad (3.18)$$

This indicates that unit cell size of general phononic crystals is comparable to wavelength of the matrix when wave speed becomes imaginary value. Since this results in high scattering waves, phononic crystals cannot be used in this work.

Then, how to obtain imaginary wave speed at low frequencies by periodicity? In this work, a new idea of imposing very weak mass-spring system along circumferential direction is proposed. The idea is illustrated in fig. 3.3 (a). Comparing fig. 3.3 (a) with fig. 3.2 (a), it can be seen that additional mass-spring system of m_2 and s_2 is considered while m_2 is almost same as m_1 and $s_2 \ll s_1$. In this case, mass-spring motion along

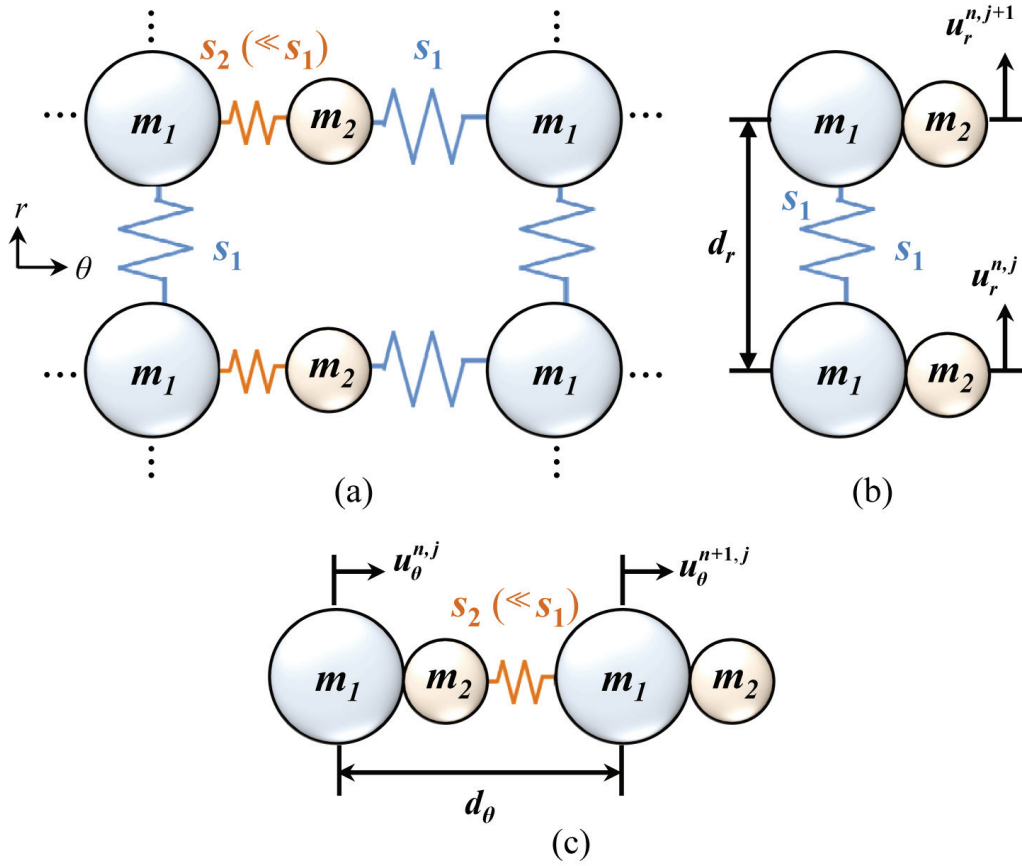


Fig. 3.3 (a) Schematic diagram of newly proposed mass-spring system for desired hyperbolic elastic metamaterial, and free-body diagrams along (b) radial direction and (c) circumferential direction

radial direction (shown in fig. 3.3 (b)) is almost same as that in the previous case. The only difference is that the mass of the system is not m_1 but $m_1 + m_2$. For this case, the equation of motion for mass $m_1 + m_2$ can be written as

$$(m_1 + m_2)\ddot{u}_r^{n,j} = s_1(u_r^{n,j+1} - u_r^{n,j}) - s_1(u_r^{n,j} - u_r^{n,j-1}). \quad (3.19)$$

Assuming periodic wave solution for $u_r^{n,j}$ as in equation (3.2), equation (3.19) becomes

$$\begin{aligned}
-(m_1 + m_2)\omega^2 &= s_1(\exp(-ik_r d_r) - 1) - s_1(1 - \exp(ik_r d_r)) \\
&= s_1(\exp(-ik_r d_r) + \exp(ik_r d_r)) - 2s_1
\end{aligned} \tag{3.20}$$

Using $2 \cos x = \exp(-ix) + \exp(ix)$, equation (3.20) can be simplified as

$$-(m_1 + m_2)\omega^2 = 2s_1 \cos(k_r d_r) - 2s_1, \tag{3.21}$$

or arranging with respect to k_r ,

$$\cos(k_r d_r) = \frac{2s_1 - (m_1 + m_2)\omega^2}{2s_1}. \tag{3.22}$$

Thus, the frequency where wave speed becomes purely imaginary can be calculated from equation (3.15) as

$$\omega > 2\sqrt{\frac{s_1}{(m_1 + m_2)}}. \tag{3.23}$$

Corresponding wavevector at the frequency in equation (3.23) in homogeneous isotropic media is

$$k_r = 2\sqrt{\frac{ms_1}{(m_1 + m_2)s}} \frac{1}{d} = 2\sqrt{\frac{c_r}{c}} \frac{1}{d_r} \tag{3.24}$$

and corresponding wavelength is

$$\lambda_r = \frac{2\pi}{k_r} = \sqrt{\frac{c}{c_r}} \pi d_r. \tag{3.25}$$

Here, c_r denotes wave speed of the mass-spring system in fig. 3.3 (a) along radial direction. In equation (3.25), since m_2 is not very high compared to m_1 , c_r has almost same order compared to c . Therefore, wavevector and unit cell size of the system is comparable to those of the matrix when wave speed becomes imaginary value.

However, unlike wave motion along radial direction, wave motion along circumferential direction becomes significantly altered by the additional mass-spring system of m_2 and s_2 . As shown in fig. 3.3 (c), since $s_2 \ll s_1$, equivalent spring coefficients along circumferential direction can be calculated as

$$s_{eq} = \frac{s_1 s_2}{s_1 + s_2} \simeq \frac{s_1 s_2}{s_1} = s_2. \quad (3.26)$$

Therefore, mass-spring system along circumferential direction can be simplified as in fig. 3.3 (c). From fig. 3.3 (c), equation of motion along circumferential direction can be expressed as

$$(m_1 + m_2)\ddot{u}_\theta^{n,j} = s_2(u_\theta^{n+1,j} - u_\theta^{n,j}) - s_2(u_\theta^{n,j} - u_\theta^{n-1,j}). \quad (3.27)$$

After assuming periodic wave solution given in equation (3.8), equation (3.27) becomes

$$\begin{aligned} -(m_1 + m_2)\omega^2 &= s_2(\exp(-ik_\theta d_\theta) - 1) - s_2(1 - \exp(ik_\theta d_\theta)) \\ &= s_2(\exp(-ik_\theta d_\theta) + \exp(ik_\theta d_\theta)) - 2s_2 = 2s_2 \cos(k_\theta d_\theta) - 2s_2. \end{aligned} \quad (3.28)$$

Equation (3.28) can be expressed with respect to k_θ as

$$\cos(k_\theta d_\theta) = \frac{2s_2 - (m_1 + m_2)\omega^2}{2s_2}. \quad (3.29)$$

Accordingly, frequency where wave speed starts to be imaginary value along circumferential direction is

$$\omega > 2\sqrt{\frac{s_2}{(m_1 + m_2)}}. \quad (3.30)$$

For the frequency in equation (3.30), wavevector in isotropic homogeneous media is

$$k_\theta = 2\sqrt{\frac{ms_2}{(m_1 + m_2)s}} \frac{1}{d} = 2\sqrt{\frac{c_\theta}{c}} \frac{1}{d_\theta}, \quad (3.31)$$

and wavelength in isotropic homogeneous media is

$$\lambda_\theta = \frac{2\pi}{k_\theta} = \sqrt{\frac{c}{c_\theta}} \pi d_\theta. \quad (3.32)$$

Comparing equation (3.31) with equation (3.25), it can be seen that if wave speed starts to be imaginary value along circumferential direction, wavelength in isotropic media is much larger than the size of the unit cell since $s_2 \ll s_1$ and $c_\theta \ll c$. Moreover, because additional mass-spring m_2 and s_2 is only connected along circumferential direction, there exist certain frequency ranges where wave speed along radial direction is real while that along circumferential direction is imaginary. Fig. 3.4 shows the frequency range where the proposed mass-spring system can be used as hyperbolic elastic metamaterial. Therefore, from the analysis of mass-spring system in fig. 3.3 (a), it is shown that the desired elastic metamaterial can be achieved by realizing equivalent elastic structure for the mass-spring system in fig. 3.3 (a).

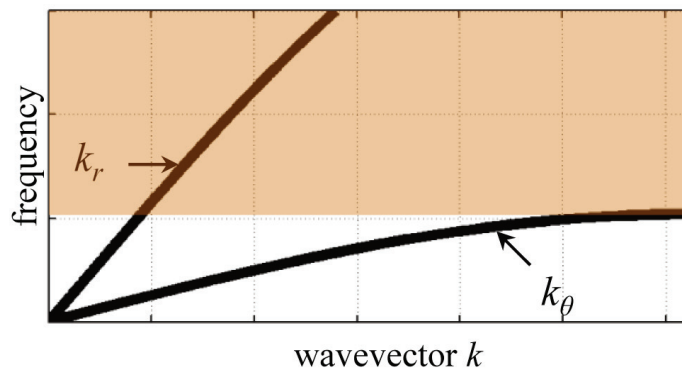


Fig. 3.4 Schematic dispersion curve along circumferential and radial directions of the mass-spring system shown in fig. 3.3 (a)

It should be noted that mass-spring system in fig. 3.3 (a) can also be calculated by taking both springs s_1 and s_2 into consideration and formulating equation of motions for the 2 degree of freedom system. However, only simple approach is made in this chapter to illustrate the main idea in designing hyperbolic elastic metamaterial, i.e., adding additional mass-spring system m_2 and s_2 . The more accurate approach considering both spring coefficients are shown in chapter 5.

3.2.3 Proposition of new hyperbolic elastic metamaterial and hyperlens

Based on the mass-spring model shown in fig. 3.3 (a), the hyperbolic elastic metamaterials which satisfy all 4 requirements are designed as shown in fig. 3.5. From the metamaterial, new elastic hyperlens is also designed. Fig. 3.6 shows the picture of the

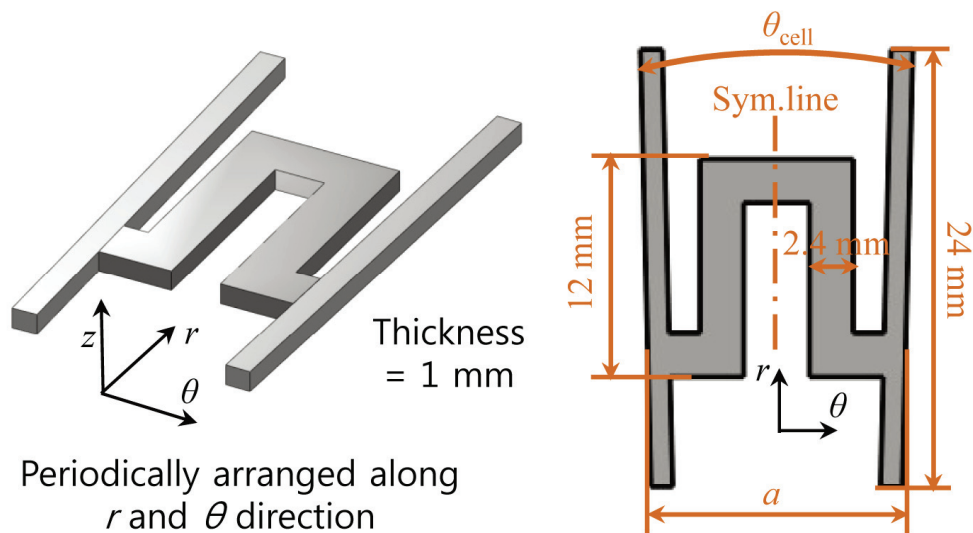


Fig. 3.5 Geometric configuration of the proposed hyperbolic elastic metamaterial

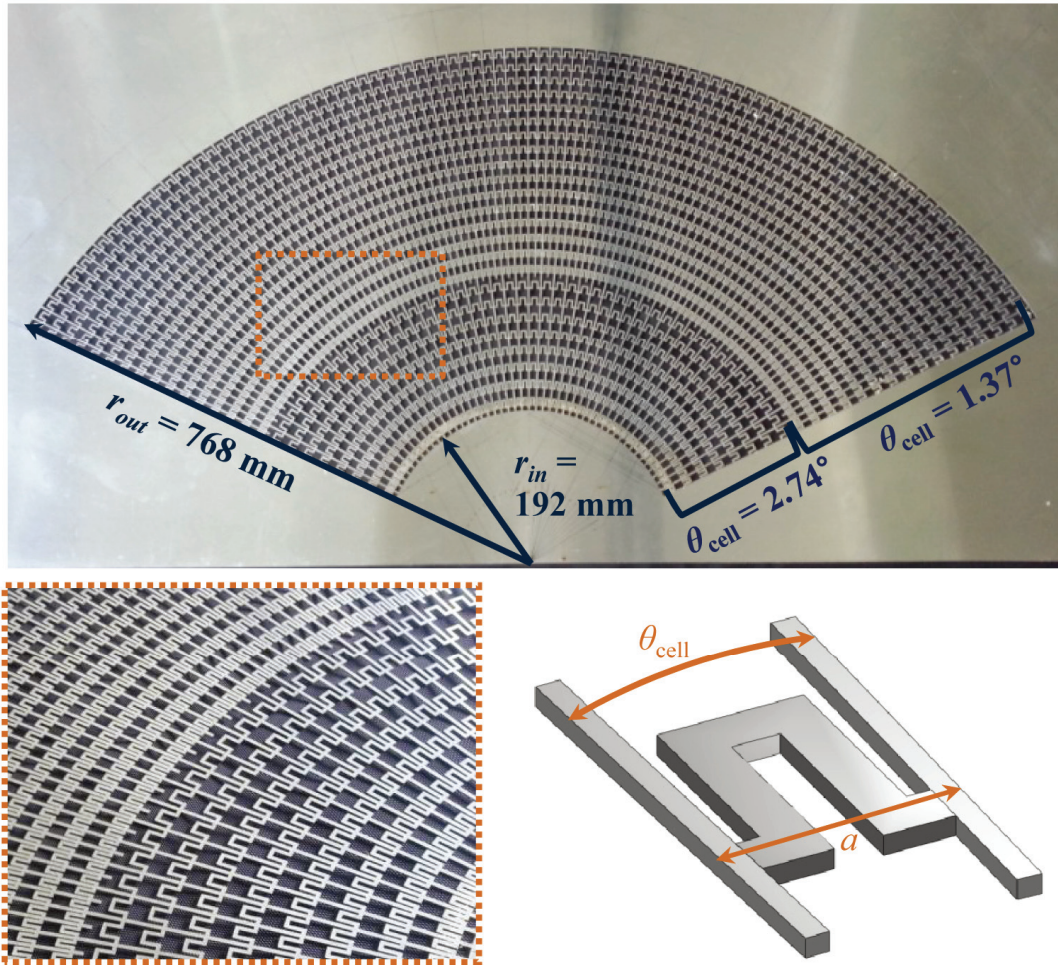


Fig. 3.6 Picture of the proposed hyperlens consists of the proposed elastic metamaterial shown in fig. 3.5

designed elastic hyperlens which is fabricated in 1 mm thick aluminum plate. Here, the metamaterials used in the lens are made by assembly of aluminum segments of 2.4 mm width. To arrange the metamaterials cylindrically, the metamaterial with $a = 9.6 \text{ mm}$ and $\theta_{cell} = 2.74^\circ$ is used at the inner circle of the lens, and a is increased by 1.2 mm as they approaches to the outer circle of the lens. Along the circumferential direction, same metamaterials are arranged as can be seen in fig. 3.6.

In arranging the metamaterial to form hyperlens, the range of the value a would be too wide if the metamaterials are so arranged in the whole lens and it would be very hard to make all EFC of the metamaterials used in the lens hyperbolic. Here, a little trick is used to avoid the problem. If a becomes larger than 19.2 mm, the metamaterial is divided into two metamaterials of which a and θ_{cell} are reduced by half. As a result, only the metamaterials with a from 9.6 mm to 19.2 mm are used in the proposed lens. The magnification ratio, i.e., the ratio between the inner circle and the outer circle of the lens, is 1:4, but higher magnification ratio can also be realized if one repeats the metamaterials as explained.

The key in the proposed hyperbolic elastic metamaterial design is introducing corrugated structure where mode coupling significantly takes place and stiffness is extremely lowered. Reviewing the previous section, resonance-based elastic metamaterial is avoided due to narrow operating frequency range and high loss while phononic crystal is avoided due to scattering originated from large scale of its unit cell. However, as shown in fig. 3.3 (a), introducing structure having extremely low stiffness along circumferential direction can make the relative size of the unit cell much smaller compared to the operating wavelength. This periodic microstructure may not suffer from the scattering problem, and thus can satisfy all 4 requirements. To extremely slow down wave speed, the idea of coupling longitudinal and bending motion is utilized. Since longitudinal stiffness is usually much higher than bending stiffness, coupling of longitudinal and bending motion can significantly lower the longitudinal stiffness of structure. Therefore, the proposed elastic metamaterial is designed to have a corrugated geometry to

effectively couple two deformation modes.

The coupling of longitudinal and bending motion in the proposed elastic metamaterial can be observed from the S0 mode's (lowest order symmetric Lamb wave mode) mode shape of the proposed elastic metamaterial. Fig. 3.7 shows the S0 wave mode's mode shape. From fig. 3.7 (a), it can be seen that internal corrugated structure (indicated by red dotted box) shows accordion-like motion during S0 wave propagation along circumferential direction. Both longitudinal and bending motion can be found in the corrugated structure, proving that the metamaterial shows high coupling between two modes. As a result, the wave speed along the circumferential direction is extremely

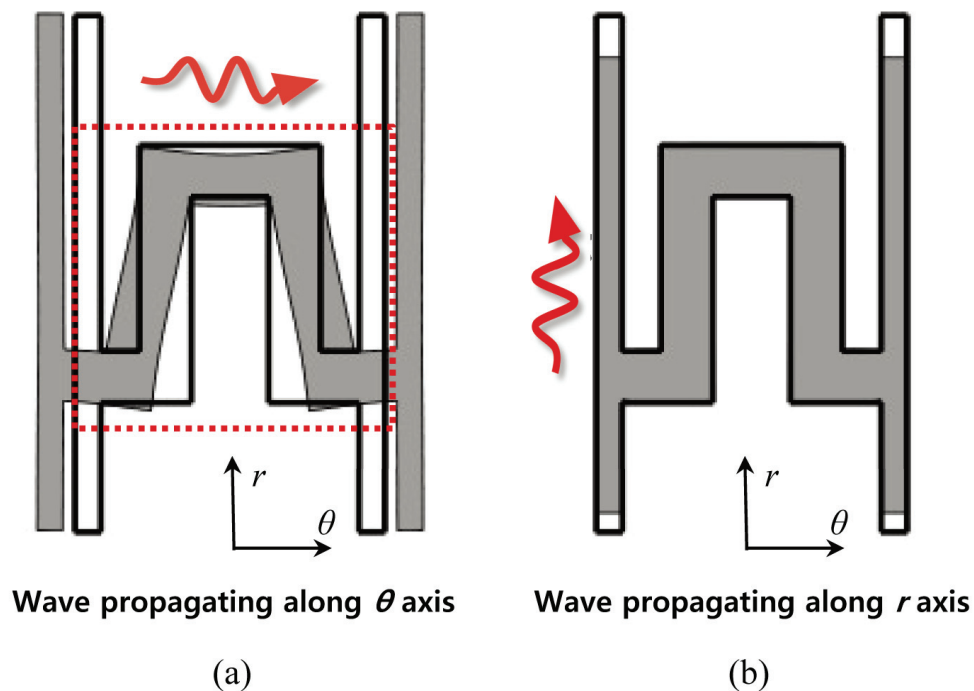


Fig. 3.7 Mode shape of the S0 wave propagating along (a) circumferential and (b) radial direction in the proposed hyperbolic elastic metamaterial

slowed, which results in the band-gap frequency around 15 kHz. In this frequency, the wavelength of S0 wave mode at 1 mm thick aluminum plate is 346.66 mm, which is more than an order larger compared to the size of the unit cell of the proposed metamaterial. Thus, the scattering problem can be avoided and the proposed metamaterial can be treated as homogeneous media.

In summary, the size of the proposed elastic metamaterial is much smaller than the operating wavelength, and requirement 3 is satisfied. Also, there exist various parameters related to the corrugated geometry, and requirement 4 is satisfied, too. In the following section, the satisfaction of requirement 1 and 2 will be shown.

It should be emphasized that although the proposed elastic metamaterial resembles the acoustic coiling-up structures proposed by Liang *et al.* [57], we figured out that the proposed structure cannot be explained by wave-path elongation. Unlike acoustics, bending deformation exists in elastic mediums and bending motion of the structure should be considered to correctly demonstrate the proposed structure. This point will be clearly shown in chapter 5 where analytic modeling of the proposed elastic metamaterial is formulated. For more information about the acoustic metamaterial based on coiling-up space technique, see Ref. [58, 59].

3.3 Numerical verification of hyperbolic elastic metamaterial

3.3.1 Finite element formulation for wave dispersion characteristics of the proposed elastic metamaterial

To figure out that the proposed elastic metamaterial is hyperbolic metamaterial, i.e., has hyperbolic EFC, finite element method is formulated and applied. Among various methods that can calculate wave dispersion characteristics of metamaterials, numerical method based on finite element analysis, proposed by Langlet *et al.* [60], provides fast and accurate results without convergence problem. This method utilizes periodic boundary condition at each boundary of the unit cell and formulates eigenvalue problem to calculate wave dispersion characteristics.

Before proceeding to the detailed finite element formulation procedure, special attention is required that some analytic method cannot be used for calculating wave dispersion characteristics of the proposed elastic metamaterial. For example, the Plane Wave Expansion method (PWE) which was proposed by Kushwaha *et al.* [61,62] cannot be used for the proposed metamaterial. Since PWE assumes series of plane waves inside unit cell, it may lead to wrong results for unit cell in which plane waves cannot be formulated, as in the proposed elastic metamaterial.

Starting from basic elastic equation, the constitutive equation can be written in tensor form as

$$\sigma_{ij} = C_{ijkl} e_{kl} \quad (3.33)$$

where σ , e and C denote stress, strain and elastic stiffness tensor, respectively (here, although general notation of strain is ε , e is used instead for strain to avoid the confusion between strain and electric permittivity). Here, $i, j, k, l = x, y, z$. Also, equation of motion in elastic body without body force is defined as

$$\sigma_{ji,j} = \rho_i \frac{\partial^2 u_i}{\partial t^2}. \quad (3.34)$$

Finally, strain-displacement relation, also called constitutive equation can be written as

$$e_{ij} = \frac{1}{2}(u_{i,j} + u_{j,i}). \quad (3.35)$$

In finite element analysis, it is convenient to use matrix form rather than tensor form. By using matrix form, equation (3.35) can be re-written as

$$\mathbf{e} = \nabla_s \mathbf{U}. \quad (3.36)$$

while each matrix variables are defined as follows;

$$\mathbf{U} = [u_x \quad u_y \quad u_z]^T \quad (3.37a)$$

$$\mathbf{e} = [e_{xx} \quad e_{yy} \quad e_{zz} \quad 2e_{xy} \quad 2e_{yz} \quad 2e_{xz}]^T \quad (3.37b)$$

$$\nabla_s = \begin{bmatrix} \partial/\partial x & 0 & 0 & \partial/\partial y & 0 & \partial/\partial z \\ 0 & \partial/\partial y & 0 & \partial/\partial x & \partial/\partial z & 0 \\ 0 & 0 & \partial/\partial z & 0 & \partial/\partial y & \partial/\partial x \end{bmatrix}^T. \quad (3.37c)$$

As same manner, writing equation (3.33) in matrix form results in the following equation.

$$\boldsymbol{\sigma} = \mathbf{C} \mathbf{e} \quad (3.38)$$

where

$$\boldsymbol{\sigma} = [\sigma_{xx} \quad \sigma_{yy} \quad \sigma_{zz} \quad \sigma_{xy} \quad \sigma_{yz} \quad \sigma_{xz}]^T . \quad (3.39)$$

In equation (3.38), the elastic stiffness matrix \mathbf{C} may differ depends on the material type.

For orthotropic material, it is defined as

$$\mathbf{C} = \begin{bmatrix} C_{xxxx} & C_{xyxy} & C_{xzzz} & 0 & 0 & 0 \\ C_{yyxx} & C_{yyyy} & C_{yyzz} & 0 & 0 & 0 \\ C_{zzxx} & C_{zzyy} & C_{zzzz} & 0 & 0 & 0 \\ 0 & 0 & 0 & C_{xyxy} & 0 & 0 \\ 0 & 0 & 0 & 0 & C_{yzyz} & 0 \\ 0 & 0 & 0 & 0 & 0 & C_{xzxz} \end{bmatrix} . \quad (3.40)$$

For equation of motion shown in equation (3.34), weak-formulation is widely used for matrix form. Imposing virtual work principle in equation (3.34) yields

$$\int_V \sigma_{ji,j} \delta u_i dV = \int_V \rho_i \frac{\partial^2 u_i}{\partial t^2} \delta u_i dV . \quad (3.41)$$

In equation (3.41), the left term can be expanded as

$$\int_V \sigma_{ji,j} \delta u_i dV = \int_V (\sigma_{ij} \delta u_i)_{,j} dV - \int_V \sigma_{ij} \delta u_{i,j} dV . \quad (3.42)$$

Assuming traction free condition, the first term in the right side terms in equation (3.42) can be ignored. Regarding that $\delta u_{i,j} = \delta e_{ij}$, equation (3.41) can be re-written as

$$-\int_V \sigma_{ji} \delta e_{ij} dV = \int_V \rho_i \frac{\partial^2 u_i}{\partial t^2} \delta u_i dV \quad (3.43)$$

which can be expressed in the matrix form as

$$-\int_V \delta \mathbf{e}^T \boldsymbol{\sigma} dV = \int_V \boldsymbol{\rho} \delta \mathbf{U}^T \frac{\partial^2}{\partial t^2} \mathbf{U} dV \quad (3.44)$$

while

$$\boldsymbol{\rho} = \begin{bmatrix} \rho_{xx} & 0 & 0 \\ 0 & \rho_{yy} & 0 \\ 0 & 0 & \rho_{zz} \end{bmatrix}. \quad (3.45)$$

It should be noted that usually $\rho_{xx} = \rho_{yy} = \rho_{zz} = \rho$, anisotropic density is sometimes observed for metamaterials such that $\rho_{xx} \neq \rho_{yy} \neq \rho_{zz}$. Finally, assuming harmonic wave solution for displacement fields such as $\mathbf{U} \sim \mathbf{U} \exp(i\omega t)$, equation (3.44) can be re-written as follow;

$$\int_V \delta \mathbf{e}^T \boldsymbol{\sigma} dV = \omega^2 \int_V \delta \mathbf{U}^T \boldsymbol{\rho} \mathbf{U} dV \quad (3.46)$$

In finite element analysis, the displacement field \mathbf{U} is interpolated by the displacement fields at finite element nodes $\hat{\mathbf{U}}$ with proper shape function \mathbf{N} as

$$\mathbf{U} = \mathbf{N} \hat{\mathbf{U}}. \quad (3.47)$$

For example, in non-dimensional coordinate ξ such that each element is defined in $-1 < \xi < 1$, each variables in equation (3.47) are defined as

$$\hat{\mathbf{U}} = [u_1^1 \quad u_1^2]^T \quad (3.48a)$$

$$\mathbf{N} = \frac{1}{2} [1 - \xi \quad 1 + \xi] \quad (3.48b)$$

where superscripted numbers 1 and 2 denote node number at the element. After discretization, equation (3.36) and (3.38) can be re-written as

$$\mathbf{e} = \nabla_s \mathbf{N} \hat{\mathbf{U}}, \quad (3.49a)$$

$$\boldsymbol{\sigma} = \mathbf{C} \nabla_s \mathbf{N} \hat{\mathbf{U}} \quad (3.49b)$$

respectively. Therefore, following equation can be derived from equation (3.46);

$$\int_V \delta \hat{\mathbf{U}}^T \mathbf{N}^T \nabla_s^T \mathbf{C} \nabla_s \mathbf{N} \hat{\mathbf{U}} dV = \omega^2 \int_V \delta \hat{\mathbf{U}}^T \mathbf{N}^T \boldsymbol{\rho} \mathbf{N} \hat{\mathbf{U}} dV \quad (3.50)$$

In equation (3.50), each integration is made for each element. Extracting virtual displacement term $\delta \hat{\mathbf{U}}$, equation (3.50) can be simplified as

$$\mathbf{K}_{elem} \hat{\mathbf{U}} = \omega^2 \mathbf{M}_{elem} \hat{\mathbf{U}} \quad (3.51)$$

while mass and stiffness matrix of each finite element are defined as [63]

$$\mathbf{M}_{elem} = \int_V \mathbf{N}^T \boldsymbol{\rho} \mathbf{N} dV, \quad (3.52a)$$

$$\mathbf{K}_{elem} = \int_V \mathbf{N}^T \nabla_s^T \mathbf{C} \nabla_s \mathbf{N} dV. \quad (3.52a)$$

Eventually, the mass and stiffness matrix of whole system can be calculated by assembling element's mass and stiffness matrix, as

$$\mathbf{M} = \sum_n \mathbf{M}_{elem}^n, \quad \mathbf{K} = \sum_n \mathbf{K}_{elem}^n. \quad (3.53)$$

In equation (3.53), mass and stiffness matrix of nth element is denoted by \mathbf{M}_{elem}^n and \mathbf{K}_{elem}^n , respectively. As a result, the finite element formulation for whole system is given as

$$\mathbf{K} \hat{\mathbf{U}} = \omega^2 \mathbf{M} \hat{\mathbf{U}} \quad (3.54)$$

To calculate wave dispersion characteristics, periodic boundary condition is imposed on the boundaries 1 to 4, as illustrated in fig. 3.8. The periodic boundary condition in this case can be written as

$$\hat{\mathbf{U}}_2 = \hat{\mathbf{U}}_1 \exp(-ik_x a), \quad \hat{\mathbf{U}}_4 = \hat{\mathbf{U}}_3 \exp(-ik_y h) \quad (3.55a)$$

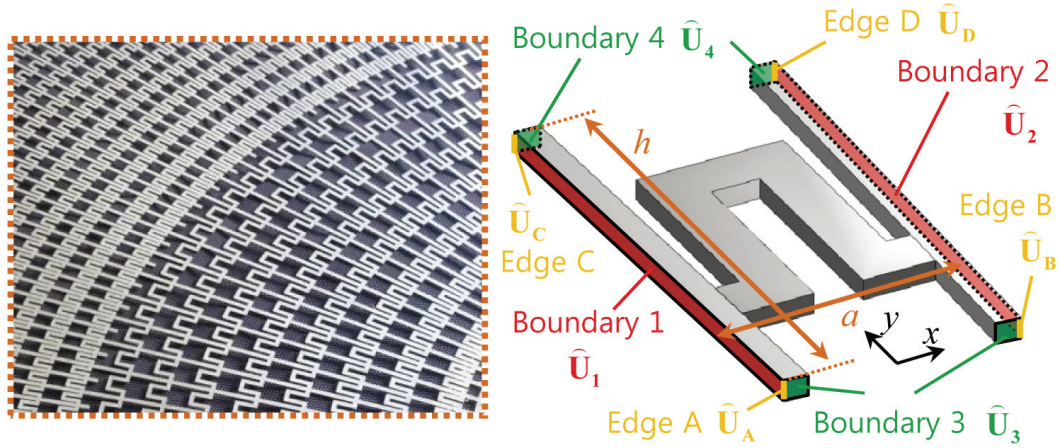


Fig. 3.8 Schematic illustration of the periodic boundary condition imposed for wave dispersion calculation

$$\hat{\mathbf{U}}_B = \hat{\mathbf{U}}_A \exp(-ik_x a), \quad \hat{\mathbf{U}}_C = \hat{\mathbf{U}}_A \exp(-ik_y h), \quad \hat{\mathbf{U}}_D = \hat{\mathbf{U}}_A \exp(-ik_x a - ik_y h) \quad (3.55b)$$

where k_x and k_y are wavevector components along x and y direction, respectively.

The definition of geometric variables a and h are shown in fig. 3.8. The displacement fields $\hat{\mathbf{U}}_1$, $\hat{\mathbf{U}}_2$, $\hat{\mathbf{U}}_3$ and $\hat{\mathbf{U}}_4$ denote the displacement fields in corresponding boundaries, and $\hat{\mathbf{U}}_A$, $\hat{\mathbf{U}}_B$, $\hat{\mathbf{U}}_C$ and $\hat{\mathbf{U}}_D$ denote those in corresponding edges, as shown in fig. 3.8. To explain the imposition of periodic boundary conditions, displacement fields of all nodes in finite element model, $\hat{\mathbf{U}}$, is separately considered as follows :

$$\hat{\mathbf{U}} = [\hat{\mathbf{U}}_1 \quad \hat{\mathbf{U}}_2 \quad \hat{\mathbf{U}}_3 \quad \hat{\mathbf{U}}_4 \quad \hat{\mathbf{U}}_A \quad \hat{\mathbf{U}}_B \quad \hat{\mathbf{U}}_C \quad \hat{\mathbf{U}}_D \quad \hat{\mathbf{U}}_{\text{etc}}]^T. \quad (3.56)$$

In equation (3.56), $\hat{\mathbf{U}}_{\text{etc}}$ is displacement vectors that aren't belongs to the boundaries 1 to 4 or edges A to D in fig. (3.8). Accordingly, the boundary condition shown in equation (3.55) can be expressed as

$$\hat{\mathbf{U}} = \mathbf{P} \left[\hat{\mathbf{U}}_1 \quad \hat{\mathbf{U}}_2 \quad \hat{\mathbf{U}}_A \quad \hat{\mathbf{U}}_{\text{etc}} \right]^T \quad (3.57)$$

while \mathbf{P} is defined as

$$\mathbf{P} = \begin{bmatrix} \mathbf{I}_1 & \mathbf{0} & \exp(-ik_x a) \mathbf{I}_3 & \mathbf{0} & \mathbf{0} \\ \mathbf{0} & \mathbf{I}_2 & \mathbf{0} & \exp(-ik_y h) \mathbf{I}_4 & \mathbf{0} \\ \mathbf{0} & \mathbf{0} & \mathbf{0} & \mathbf{0} & \mathbf{I}_A \\ \mathbf{0} & \mathbf{0} & \mathbf{0} & \mathbf{0} & \mathbf{0} \\ \mathbf{0} & \mathbf{0} & \mathbf{0} & \mathbf{0} & \mathbf{0} \\ \mathbf{0} & \mathbf{0} & \mathbf{0} & \mathbf{0} & \mathbf{0} \\ \exp(-ik_x a) \mathbf{I}_B & \exp(-ik_y h) \mathbf{I}_C & \exp(-ik_x a - ik_y h) \mathbf{I}_D & \mathbf{0} & \mathbf{0} \\ \mathbf{0} & \mathbf{0} & \mathbf{0} & \mathbf{0} & \mathbf{I}_{\text{etc}} \end{bmatrix}^T. \quad (3.58)$$

In equation (3.58), \mathbf{I}_m indicates identity matrix having same number of rows and columns with respect to the length of vector $\hat{\mathbf{U}}_m$ while $m=1, 2, A$ or etc. Also, $\mathbf{0}$ indicates zero matrix of which components are all zero. Substituting equation (3.56) to equation (3.54) yields

$$\bar{\mathbf{P}}^T \mathbf{K} \mathbf{P} \left[\hat{\mathbf{U}}_1 \quad \hat{\mathbf{U}}_2 \quad \hat{\mathbf{U}}_A \quad \hat{\mathbf{U}}_{\text{etc}} \right]^T = \omega^2 \bar{\mathbf{P}}^T \mathbf{M} \mathbf{P} \left[\hat{\mathbf{U}}_1 \quad \hat{\mathbf{U}}_2 \quad \hat{\mathbf{U}}_A \quad \hat{\mathbf{U}}_{\text{etc}} \right]^T \quad (3.59)$$

where $\bar{\mathbf{P}}$ is the conjugated matrix of \mathbf{P} . It should be noted that $\bar{\mathbf{P}}^T$ should be considered in equation (3.59) since virtual displacement term $\delta \hat{\mathbf{U}}$ should also satisfy equation (3.57). From equation (3.59), the mass and stiffness matrix of the whole system under periodic boundary condition are defined as [60]

$$\mathbf{K}^{\text{periodic}} = \bar{\mathbf{P}}^T \mathbf{K} \mathbf{P} \quad (3.60a)$$

$$\mathbf{M}^{\text{periodic}} = \bar{\mathbf{P}}^T \mathbf{M} \mathbf{P} \quad (3.60b)$$

and the overall system equation is

$$\mathbf{K}^{\text{periodic}} \left[\hat{\mathbf{U}}_1 \quad \hat{\mathbf{U}}_2 \quad \hat{\mathbf{U}}_A \quad \hat{\mathbf{U}}_{\text{etc}} \right]^T = \omega^2 \mathbf{M}^{\text{periodic}} \left[\hat{\mathbf{U}}_1 \quad \hat{\mathbf{U}}_2 \quad \hat{\mathbf{U}}_A \quad \hat{\mathbf{U}}_{\text{etc}} \right]^T. \quad (3.61)$$

Thus, solving eigenvalue equation of equation (3.61) provides real valued eigenvalues of ω^2 . The matrix components $\mathbf{K}^{\text{periodic}}$ in equation (3.61) are defined as

$$\mathbf{K}^{\text{periodic}} = \begin{bmatrix} \mathbf{K}_{11}^{\text{periodic}} & \mathbf{K}_{12}^{\text{periodic}} & \mathbf{K}_{1A}^{\text{periodic}} & \mathbf{K}_{1etc}^{\text{periodic}} \\ \bar{\mathbf{K}}_{12}^{\text{periodic}} & \mathbf{K}_{22}^{\text{periodic}} & \mathbf{K}_{2A}^{\text{periodic}} & \mathbf{K}_{2etc}^{\text{periodic}} \\ \bar{\mathbf{K}}_{1A}^{\text{periodic}} & \bar{\mathbf{K}}_{2A}^{\text{periodic}} & \mathbf{K}_{AA}^{\text{periodic}} & \mathbf{K}_{Aetc}^{\text{periodic}} \\ \bar{\mathbf{K}}_{1etc}^{\text{periodic}} & \bar{\mathbf{K}}_{2etc}^{\text{periodic}} & \bar{\mathbf{K}}_{Aetc}^{\text{periodic}} & \mathbf{K}_{etcetc}^{\text{periodic}} \end{bmatrix} \quad (3.62)$$

where each components are

$$\mathbf{K}_{11}^{\text{periodic}} = \mathbf{K}_{11} + \mathbf{K}_{33} \quad (3.63a)$$

$$\mathbf{K}_{12}^{\text{periodic}} = \mathbf{K}_{12} + \exp(-ik_y h)\mathbf{K}_{14} + \exp(ik_x a)\mathbf{K}_{32} + \exp(ik_x a - ik_y h)\mathbf{K}_{34} \quad (3.63b)$$

$$\mathbf{K}_{1A}^{\text{periodic}} = \mathbf{K}_{1A} + \mathbf{K}_{3B} + \exp(-ik_y h)\mathbf{K}_{1C} + \exp(-ik_y h)\mathbf{K}_{3D} \quad (3.63c)$$

$$\mathbf{K}_{1etc}^{\text{periodic}} = \mathbf{K}_{1etc} + \exp(ik_x a)\mathbf{K}_{3etc} \quad (3.63d)$$

$$\mathbf{K}_{22}^{\text{periodic}} = \mathbf{K}_{22} + \mathbf{K}_{44} \quad (3.63e)$$

$$\mathbf{K}_{2A}^{\text{periodic}} = \mathbf{K}_{2A} + \exp(-ik_x a)\mathbf{K}_{2B} + \mathbf{K}_{4C} + \exp(-ik_x a)\mathbf{K}_{4D} \quad (3.63f)$$

$$\mathbf{K}_{2etc}^{\text{periodic}} = \mathbf{K}_{2etc} + \exp(ik_y h)\mathbf{K}_{4etc} \quad (3.63g)$$

$$\mathbf{K}_{AA}^{\text{periodic}} = \mathbf{K}_{AA} + \mathbf{K}_{BB} + \mathbf{K}_{CC} + \mathbf{K}_{DD} \quad (3.63h)$$

$$\mathbf{K}_{Aetc}^{\text{periodic}} = \mathbf{K}_{Aetc} + \exp(ik_x a)\mathbf{K}_{Betc} + \exp(ik_y h)\mathbf{K}_{Cetc} + \exp(ik_x a + ik_y h)\mathbf{K}_{Detc} \quad (3.63i)$$

$$\mathbf{K}_{etcetc}^{\text{periodic}} = \mathbf{K}_{etcetc} \quad (3.63j)$$

where \mathbf{K} is the system's stiffness matrix without periodic boundary condition. Note that in evaluating equation (3.63), stiffness matrix for nodes that are not connected is not considered. For example, \mathbf{K}_{13} or \mathbf{K}_{24} is zero since there is no direct connection between boundary 1 and 3 (or 2 and 4) in fig. 3.8. In same manner, $\mathbf{M}^{\text{periodic}}$ in equation

(3.61) are defined as

$$\mathbf{M}^{\text{periodic}} = \begin{bmatrix} \mathbf{M}_{11}^{\text{periodic}} & \mathbf{M}_{12}^{\text{periodic}} & \mathbf{M}_{1A}^{\text{periodic}} & \mathbf{M}_{1\text{etc}}^{\text{periodic}} \\ \bar{\mathbf{M}}_{12}^{\text{periodic}} & \mathbf{M}_{22}^{\text{periodic}} & \mathbf{K}_{2A}^{\text{periodic}} & \mathbf{M}_{2\text{etc}}^{\text{periodic}} \\ \bar{\mathbf{M}}_{1A}^{\text{periodic}} & \bar{\mathbf{M}}_{2A}^{\text{periodic}} & \mathbf{M}_{AA}^{\text{periodic}} & \mathbf{M}_{A\text{etc}}^{\text{periodic}} \\ \bar{\mathbf{M}}_{1\text{etc}}^{\text{periodic}} & \bar{\mathbf{M}}_{2\text{etc}}^{\text{periodic}} & \bar{\mathbf{M}}_{A\text{etc}}^{\text{periodic}} & \mathbf{M}_{\text{etcetc}}^{\text{periodic}} \end{bmatrix} \quad (3.64)$$

where each components are defined as in equation (3.63). From equation (3.62) and (3.64), it can be observed that $\mathbf{K}^{\text{periodic}}$ and $\mathbf{M}^{\text{periodic}}$ are Hamiltonian matrix that

$$\mathbf{K}^{\text{periodic}} = (\bar{\mathbf{K}}^{\text{periodic}})^T, \quad (3.65a)$$

$$\mathbf{M}^{\text{periodic}} = (\bar{\mathbf{M}}^{\text{periodic}})^T. \quad (3.65b)$$

Since $\mathbf{K}^{\text{periodic}}$ and $\mathbf{M}^{\text{periodic}}$ are Hamiltonian matrix, eigenvalues ω^2 in equation (3.59) is purely real value.

It should be noted that \mathbf{P} , $\mathbf{K}^{\text{periodic}}$ and $\mathbf{M}^{\text{periodic}}$ are functions of the wavevector (k_x, k_y) . From given wavevector sets of (k_x, k_y) , eigenvalue equation (3.61) can be solved. In this way, the relation between angular frequency ω and wavevector $\mathbf{k} = (k_x, k_y)$ can be evaluated.

3.3.2 EFC calculation for the proposed elastic metamaterials

From the finite element formulation in equation (3.61), EFC's of the proposed metamaterials are calculated to figure out whether the proposed metamaterial is hyperbolic or elliptic metamaterial. The procedure of EFC calculation is as follows; First,

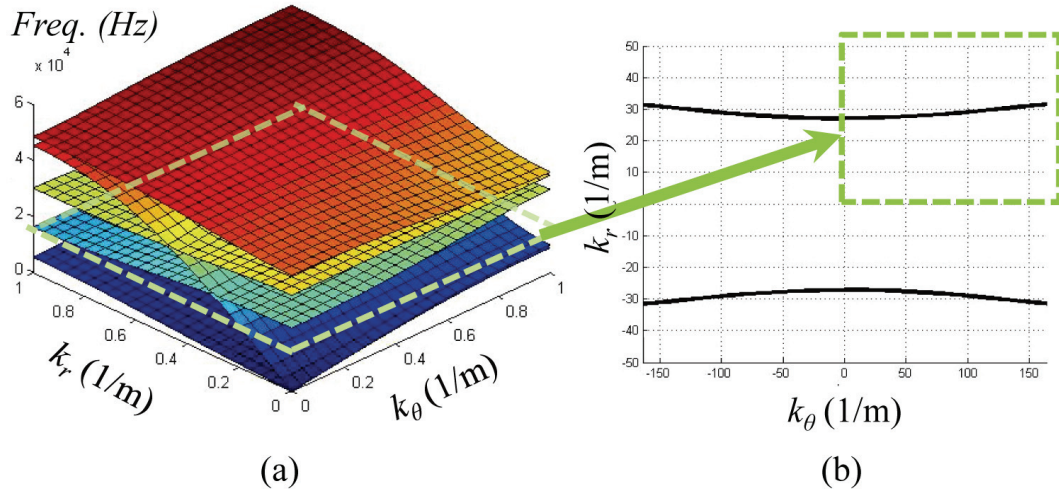


Fig. 3.9 (a) Plot of the calculated dispersion surface, (b) plot of EFC which is extracted from (a) at desired frequency

the eigenvalue equation given in equation (3.61) is solved for various pairs of (k_x, k_y) . From the solution, obtain wave dispersion surface shown in fig. 3.9 (a). EFC of the metamaterial can be obtained from the dispersion surface by drawing cross-section contour of the dispersion surface at desired frequency. For example, drawing cross-section contour for the green plane in fig. 3.9 (a) provides EFC at that frequency shown in fig. 3.9 (b). By this procedure, the EFC's of the proposed elastic metamaterials used in the hyperlens shown in fig. 3.6 are calculated. In calculation, commercial finite element analysis tool COMSOL Multiphysics [64] is used. In simulation, aluminum is considered as a base material of the proposed hyperbolic elastic metamaterial whose material properties are as follows;

$$\text{Young's Modulus } E : 70 \times 10^9 \text{ [Pa]} \quad (3.66a)$$

$$\text{Poisson's ratio } \nu : 0.33 \quad (3.66b)$$

$$\text{density } \rho : 2700 \text{ [kg/m}^3\text{]} \quad (3.66b)$$

First, the EFC's of metamaterials at desired frequency, 15 kHz, are evaluated. In EFC calculation, the elastic metamaterial having the width a from 9.6 mm to 19.2 mm are considered which are used in the proposed hyperlens. Here, although the boundaries of the unit cell along θ direction are not parallel, i.e., θ_{cell} has non-zero value, they are assumed to be parallel (that is, θ_{cell} is assumed to be zero in EFC calculation) since the values of θ_{cell} are very small. Fig. 3.10 shows the EFC's of the elastic metamaterials at 15 kHz. From fig. 3.10, it can be clearly seen that EFC's of the proposed elastic metamaterial are hyperbolic, i.e., not bounded along circumferential axis. Thus, the proposed elastic metamaterials are proven to be hyperbolic metamaterial, which satisfy the requirement 1 previously explained in section 3.2.1.

Note that only EFC of S0 waves are plotted in fig. 3.10, since S0 wave mode is mainly considered in this work. Strictly speaking, the plot of pure S0 wave is not possible since pure modes only exist along geometric symmetric directions in anisotropic material. Nevertheless, it can be still said that the proposed elastic metamaterial is hyperbolic since the mode conversion is very small and SH0 wave mode also exhibits hyperbolic EFC in the considered metamaterials. The other wave mode, A0 wave mode, is not considered through the work since the proposed metamaterials have symmetric geometry along z direction (thickness direction) and A0 wave mode is not coupled with S0 or SH0 wave mode and can be ignored.

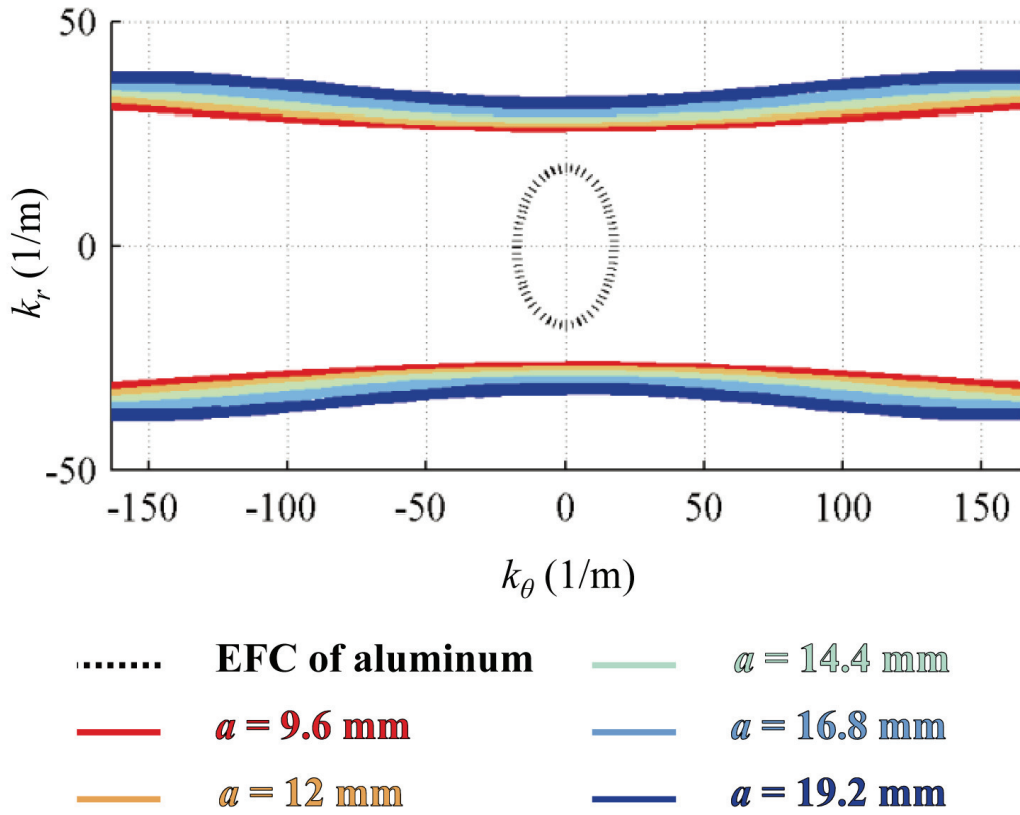


Fig. 3.10 Plot of the EFC's at 15 kHz for varying value of a of the proposed elastic metamaterial

In addition, to see whether the proposed metamaterial satisfy the requirement 2 in section 3.2.1, the EFC's of metamaterials at frequencies around the desired frequency is also checked. Since the proposed metamaterials do not rely on any resonance nature, wide operating frequency ranges can be expected. To check this point, EFC's of the hyperbolic elastic metamaterials are re-calculated for the frequency range from 11.5 kHz to 16 kHz, and the result is plotted in fig. 3.11. From the calculation result shown in fig. 3.11, it is clear that the proposed elastic metamaterial exhibit hyperbolic EFC for very wide frequency ranges. Thus, the requirement 2 is also satisfied by the proposed elastic

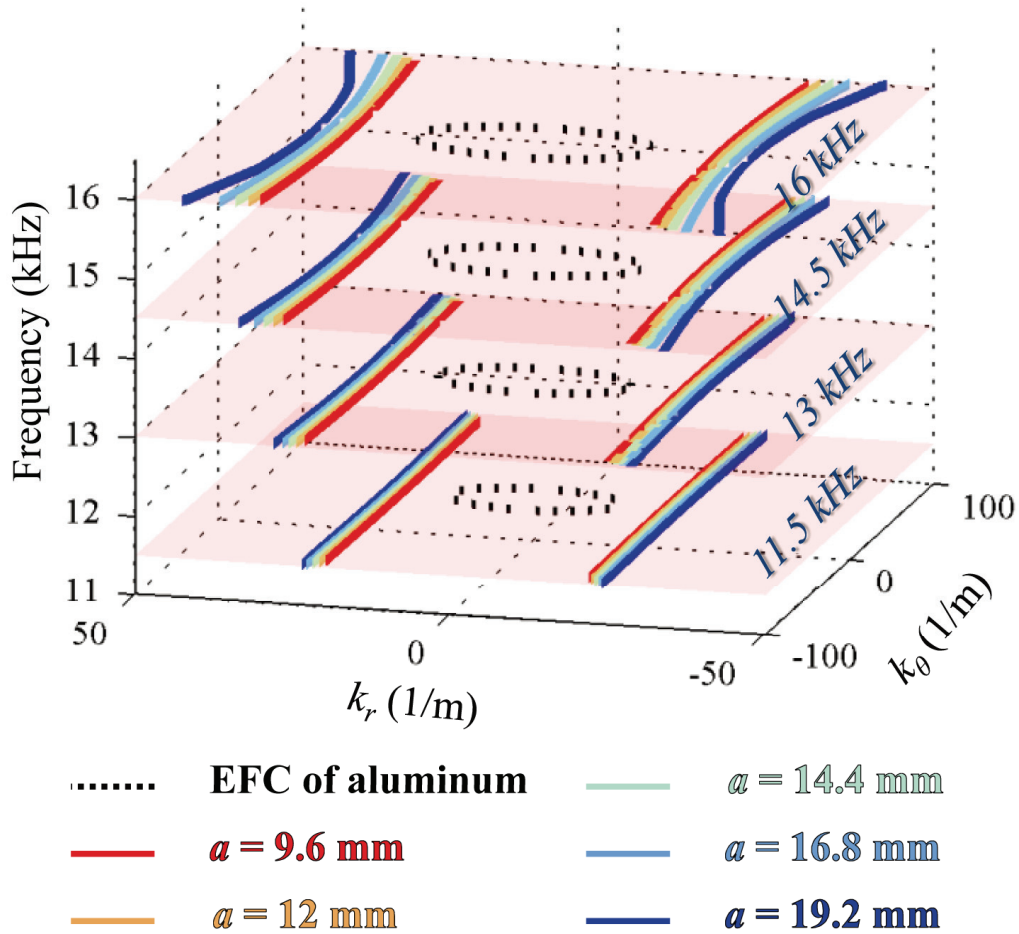


Fig. 3.11 Plot of the EFC's at various frequencies for the elastic metamaterials considered in fig. 3.6

metamaterials.

In conclusion, by EFC calculation, it is shown that the proposed elastic metamaterials satisfy the requirement 1 and 2 explained previously. In addition, it was already shown that the proposed elastic metamaterial satisfy requirement 3 and 4. Therefore, the

proposed elastic metamaterials are proved to satisfy all design requirements, and the hyperlens consists of the proposed elastic metamaterials is expected to show high performances.

3.4 Numerical simulation for the proposed elastic hyperlens

3.4.1 Numerical simulation for sub-wavelength resolution

As the proposed elastic metamaterial is proven to satisfy all design requirements, the performance of the elastic hyperlens which consists of the proposed hyperbolic elastic metamaterial should be checked. To evaluate the proposed hyperlens, capability of sub-wavelength resolution is numerically simulated. The most general and obvious way to evaluate the sub-wavelength resolution capability is imposing two sub-wavelength sources inside the hyperlens. Waves generated by two wave sources whose separation distance is below the half of the operating wavelength can be expressed in infinite series of waves having various k_θ , as scattering wave case. Thus, same physics can be used as in scattering waves which were dealt in chapter. 2. Since wave components having high k_θ , which contain sub-wavelength information, are evanescent wave in general media, two sources cannot be distinguished at far field due to diffraction limit if there is no hyperlens. However, if hyperlens can show sub-wavelength resolution, all wave components can propagate through far field, and two sources can be distinguished at far field. By simulating hyperlens having two sub-wavelength sources inside, the capability of sub-wavelength resolution can be checked.

In finite element analysis, the proposed lens structure shown in fig. 3.6 is modeled and sub-wavelength S0 wave sources of 15 kHz are modeled very closely to the internal circle of the lens, as in fig. 3.12. Each of the S0 wave sources is modeled by the line

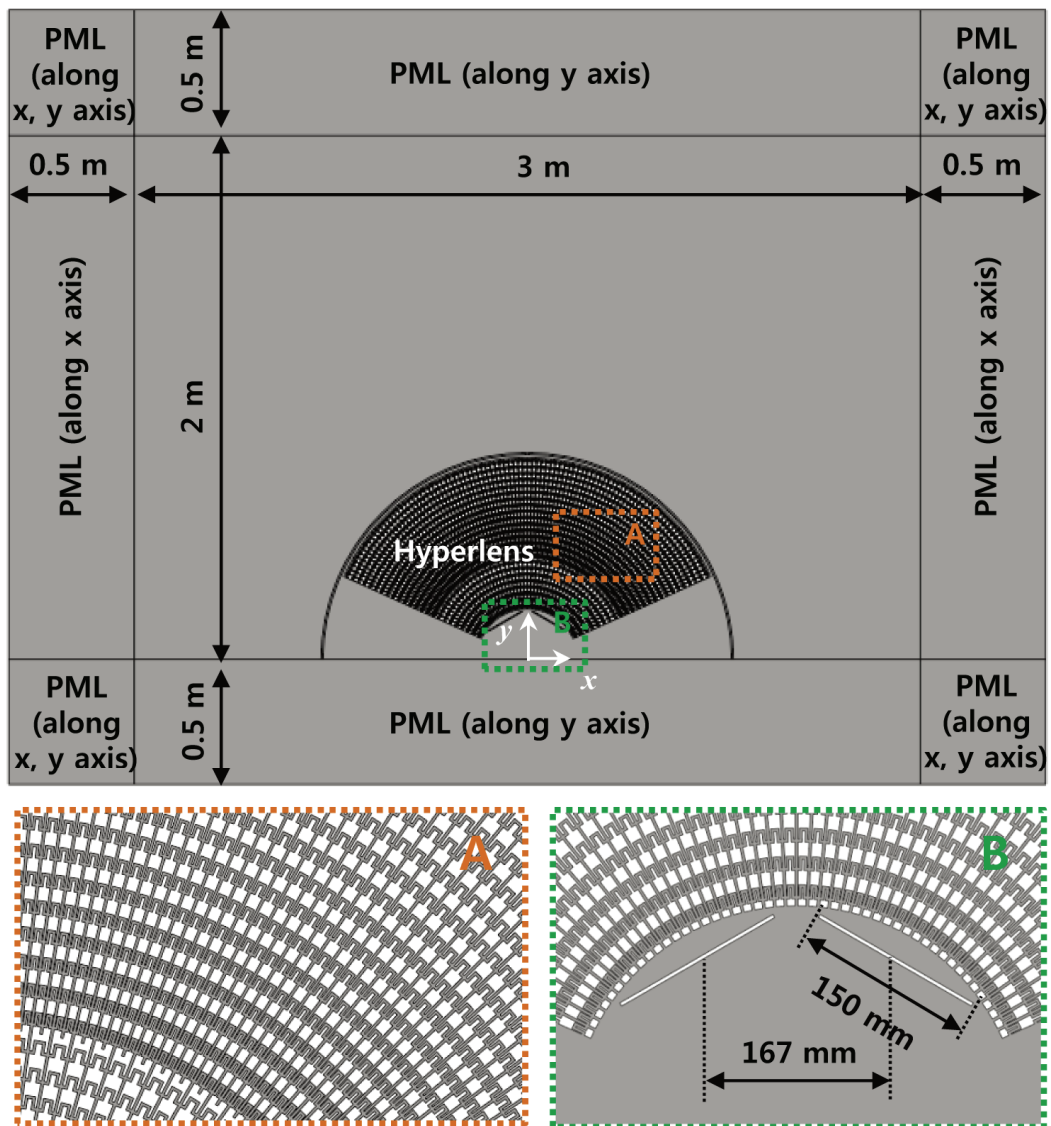


Fig. 3.12 Finite element modeling for sub-wavelength resolution simulation with the proposed hyperlens

source of which the width is 150 mm, which corresponds to almost 0.43λ of the S0 waves at 15 kHz. The distance between the centers of the two sources is set to be 167 mm, which corresponds to almost 0.48λ of the S0 waves at 15 kHz. At the end of the aluminum plate, perfectly matched layer (PML) is modeled. In analysis, the commercial finite element program COMSOL Multiphysics [64] is used and time-harmonic analysis is performed. For material property, aluminum is considered in simulation.

Strictly speaking, full 3-dimensional analysis should be performed since actual elastic metamaterial is 3-dimensional structure having finite thickness. However, since the geometry of the hyperlens is highly complicated, extremely large computational cost and time are required. To reduce the computational cost, 2-dimensional plane stress assumption is used. Since the operating frequency (15 kHz) is extremely lower than cutoff frequencies of S1 and SH1 wave modes, it can be assumed that particle displacement along the thickness direction is same for S0 wave mode, and plane stress assumption can be effectively used here. For plane stress problem, the stiffness matrix \mathbf{C} in equation (3.40) which consists of total 36 components is reduced as

$$\mathbf{C} = \begin{bmatrix} \frac{E}{1-\nu^2} & \frac{\nu E}{1-\nu^2} & 0 \\ \frac{\nu E}{1-\nu^2} & \frac{E}{1-\nu^2} & 0 \\ 0 & 0 & \frac{E}{2(1+\nu)} \end{bmatrix}. \quad (3.67)$$

Accordingly, density matrix $\mathbf{\rho}$ in equation (3.45) is reduced as

$$\mathbf{\rho} = \begin{bmatrix} \rho_{xx} & 0 \\ 0 & \rho_{yy} \end{bmatrix}. \quad (3.68)$$

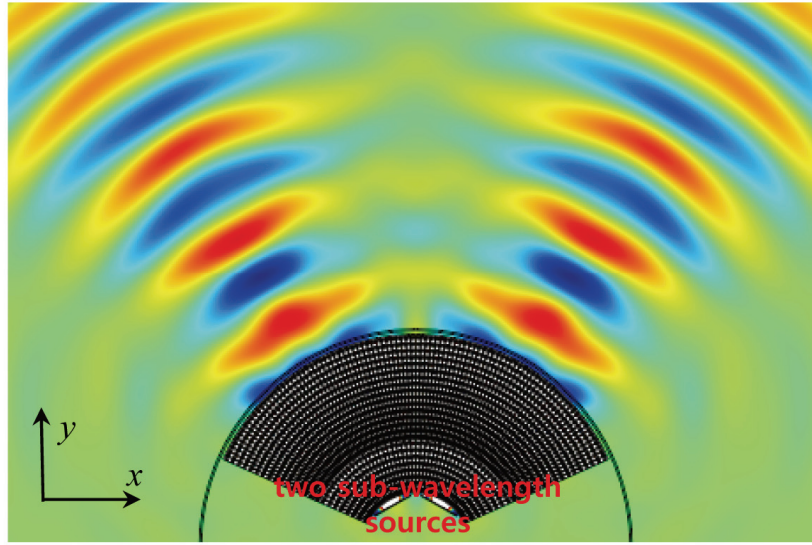
In equation (3.67) and (3.68), material properties are defined in equation (3.66). As a result, the whole system including PML is discretized with almost 730,000 2nd order 2-dimensional plane stress elements, which corresponds to 3,080,000 degrees of freedoms. This 2-dimensional assumption significantly reduced the computational time in this work.

Fig. 3.13 shows the simulation results with and without the proposed hyperbolic elastic lens. From fig. 3.13 (a,b), it can be seen that the waves from two sub-wavelength sources can be distinguished at the far field due to the hyperlens, which cannot be distinguished if there is no lens. Therefore, the capability of sub-wavelength resolution of the proposed elastic hyperlens can be clearly verified from fig. 3.13. In hyperlens, the magnification ratio is defined as

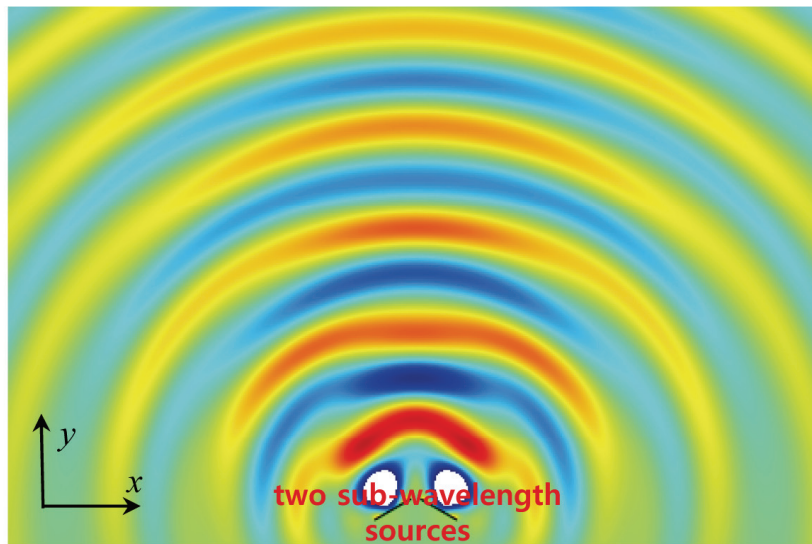
$$\text{Magnification ratio} = r_{in} : r_{out} \quad (3.69)$$

where r_{in} and r_{out} denote inner and outer radius of the hyperlens, as illustrated in fig. 3.6. For the proposed hyperlens, the magnification ratio is 1:4, but higher magnification ratio can be also realized if one repeats the unit cells as expressed previously.

Fig. 3.14 shows the displacement plot of the waves propagating in the proposed hyperlens. As can be seen in fig. 3.14, every wave in the hyperlens propagates dominantly along the radial direction and the circumferential motion inside the hyperlens is almost invisible. In fact, in the considered frequency ranges, the circumferential wave



(a)



(b)

Fig. 3.13 Plot of the S0 wave displacement generated from two sub-wavelength sources (a) with and (b) without the proposed hyperlens

vector component (k_θ) in the proposed elastic metamaterial has extremely high imaginary values. Waves in the hyperlens decay rapidly along the circumferential

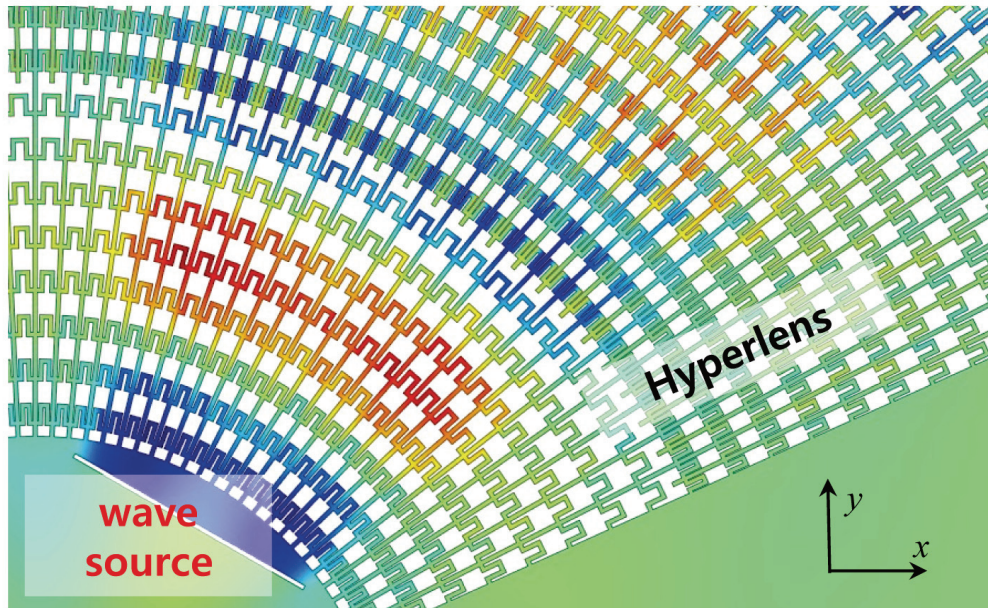
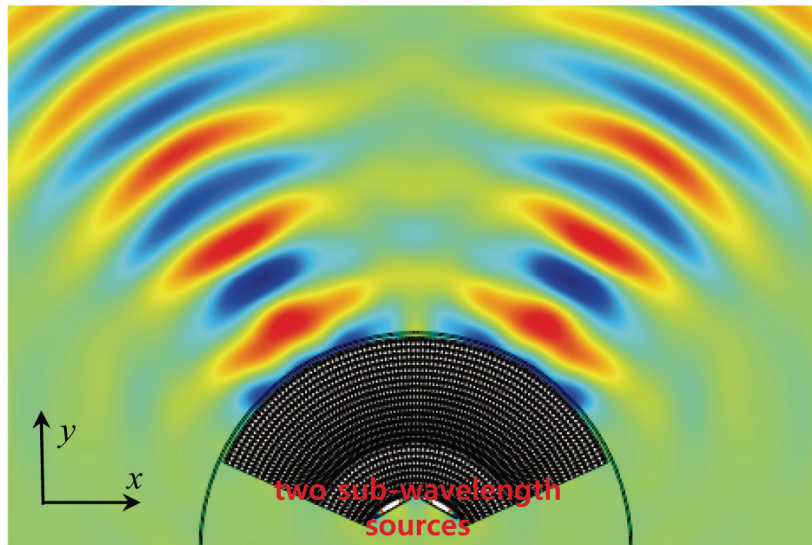


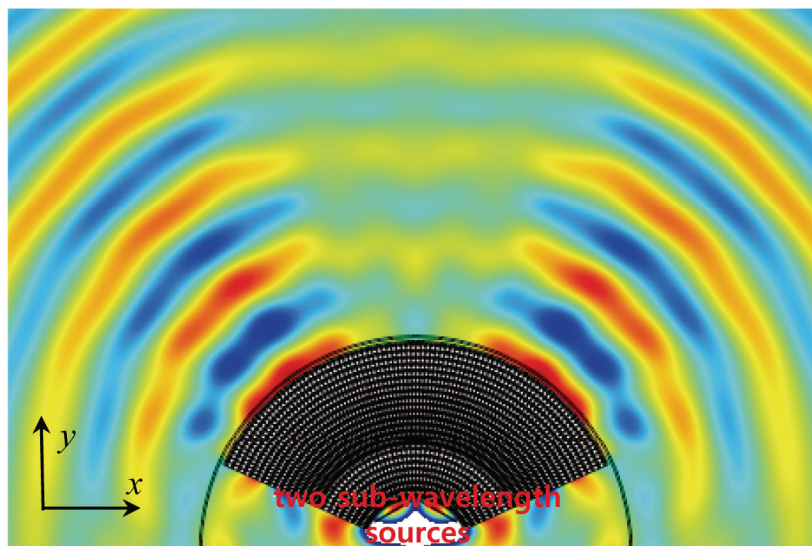
Fig. 3. 14 Plot of the S0 wave displacement inside the proposed hyperlens

direction. This means that only the neighboring unit cells along the circumferential direction are affected during wave propagation inside the hyperlens. Although the unit cells are cylindrically arranged, therefore, the wave motion inside the proposed hyperlens can be approximated in the Cartesian coordinates.

In hyperlens simulation, an important issue related to the source modeling should be addressed. The wave source modeling in sub-wavelength source simulation is one of the most important issues. Due to wave's constructive and destructive interferences, dominant directions of transmitted waves from hyperlens can be more than two based on the source modeling. This phenomenon is not related to sub-wavelength resolution; waves actuated from two sources whose separation distance is longer than the half of the wavelength can have more than two dominant directions. To avoid this phenomenon, the



(a)



(b)

Fig. 3.15 Plot of the hyperlens simulation results (a) with and (b) without the proper treatment of backward waves

sources should have sufficient directivity. This is why the line source with long length of 150 mm is used in the simulation. In addition, backward waves which are inevitably

generated associated with desired waves should be properly treated. In this simulation, very thin slit is introduced at the back of each source to get rid of the backward waves. Fig. 3.15 shows the simulation results with and without the thin slit behind the source. As clearly seen from fig. 3.15 (b), the backward waves from two sources may severely deteriorate the simulation result.

To determine the minimum distance between two sub-wavelength sources that can be successfully distinguished by the proposed hyperlens, additional simulations are performed. In the simulations, the separation distance between two sub-wavelength sources in fig. 3.12 is gradually decreased. Fig. 3.16 shows the numerical simulation results with two sub-wavelength sources of which the minimum separation distance is 3.2 mm. This value is a minimum value that can be simulated without meshing problems. It can be clearly seen that actuated waves from the two sub-wavelength sources can clearly distinguished in a far field even if the separation distance is very small. The present result suggests that if the proposed hyperlens is properly scaled to actuate elastic waves in the frequency range of 100 kHz, cracks having the minimum length of 0.5 mm can be distinguished. Thus, it can be expected that the proposed hyperlens can be applied in NDE applications improve imaging resolution greatly.

3.4.2 Numerical simulation for resolution improvement of the proposed hyperlens

Since the hyperbolic nature and capability of sub-wavelength resolution are all shown,

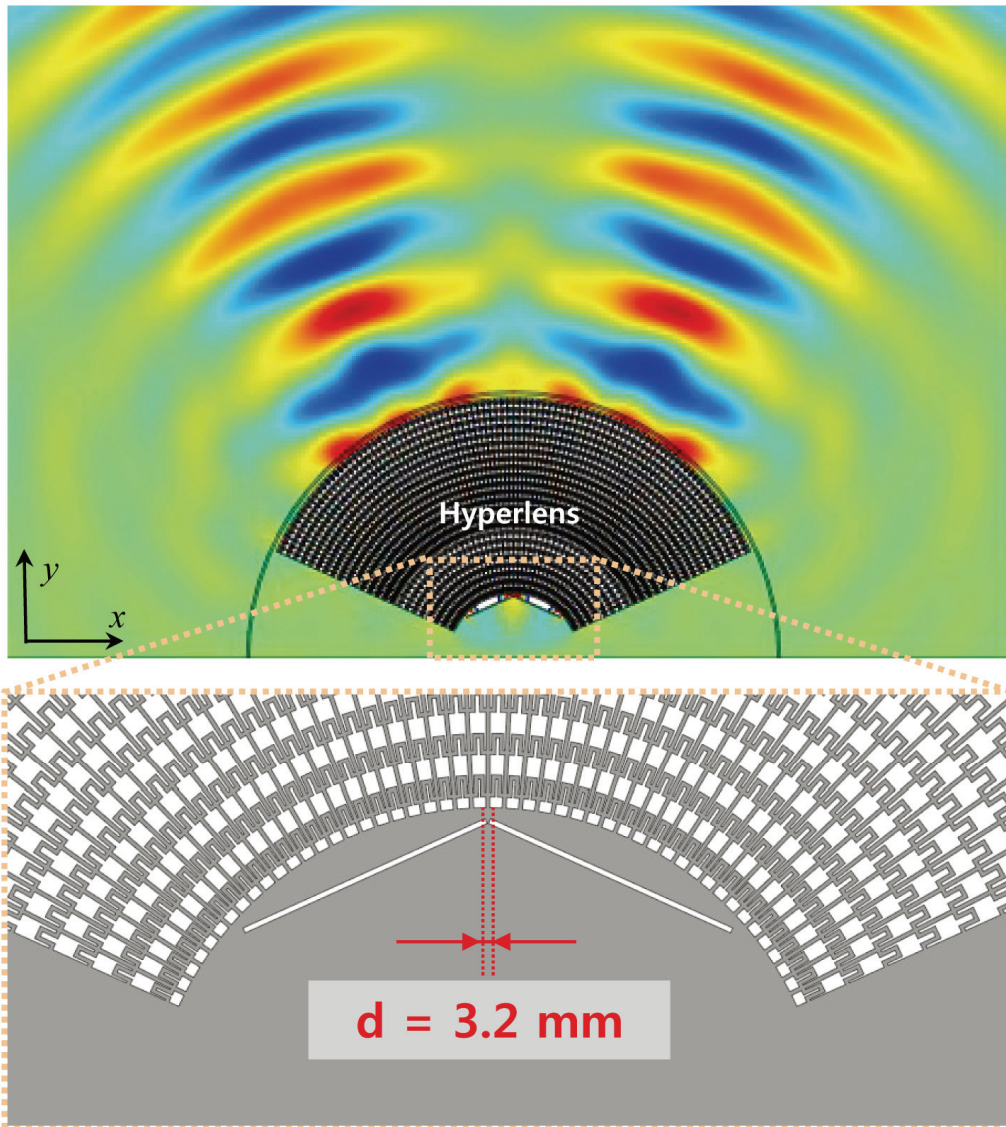


Fig. 3. 16 Plot of the hyperlens simulation result with two sub-wavelength sources whose minimum separation distance d is 3.2 mm

the following question should be answered; ‘Does the proposed elastic hyperlens really show higher resolution compared to the previously proposed one?’. Before providing related simulation results, it should be noted that comparison of two hyperlenses’ resolution is somewhat ambiguous. As previously explained, waves from two sub-

wavelength source or crack can be decomposed into infinite series of waves having various k_θ , and the reason that elliptic metamaterial is inferior than hyperbolic metamaterial is that elliptic one cannot carry waves having very high k_θ . Now, suppose that sub-wavelength sources are placed in two hyperlens – one is based on hyperbolic metamaterial while the other is based on elliptic metamaterial. Considering wave decomposition, there should exist a certain k_θ and corresponding mode number that wave can propagate through one hyperlens but can't through the other. However, in numerical simulation, the observed transmitted waves are sum of the decomposed waves. Although each decomposed waves, after certain mode number, may show drastic difference between two hyperlenses, resultant transmitted waves may not show significant difference because what is observed in simulation is total sum of decomposed waves. This means that it is very hard to perform simulations showing drastic difference such as 'two sub-wavelength sources are only distinguishable for hyperlens with hyperbolic EFC but cannot for hyperlens with elliptic EFC'. The performance of the hyperlenses can be only made by how clearly two sub-wavelength sources are distinguished at far field.

Moreover, resolution of hyperlens can also be affected by its magnification ratio. Since low magnification ratio supplies low wavevector compression, hyperlens based on hyperbolic metamaterial may show lower resolution than elliptic metamaterial if the magnification ration is much small. Thus, same magnification ratio should be used.

Therefore, in this research, the resolution performances of the two hyperlenses – one is newly proposed hyperlens which is based on the proposed hyperbolic metamaterial and the other is previously proposed hyperlens which is based on the elliptic metamaterial – are compared by how clearly two sub-wavelength sources are distinguished. The magnification ratio, i.e., the ratio of outer radius of hyperlens with respect to inner radius, is set to be constant for two hyperlenses. In simulation, three sets of two sub-wavelength sources whose separation distances are 0.48λ , 0.45λ and 0.41λ are considered. For all sources, the length of each sources are set to be constant value of 150 mm (0.43λ) to avoid any possible influence by directivity of wave source. COMSOL Multiphysics [64] is used in simulation and S0 wave of 15 kHz is considered.

Fig. 3.17 shows the wave simulation results of the transmitted waves from hyperlens with elliptic metamaterial (previously proposed by Lee *et al.*[8]) and hyperlens with hyperbolic metamaterial (newly proposed in this work). Although both previously proposed hyperlens and newly proposed hyperlens can distinguish the waves actuated by two sub-wavelength sources, transmitted waves from the newly proposed hyperlens are much more clearly distinguishable than those from the previously proposed one. Accordingly, it can be figured out that the improvement of the image fidelity is obtained by designing the metamaterial which can carry all sub-wavelength information, and this is achieved by hyperbolic EFC.

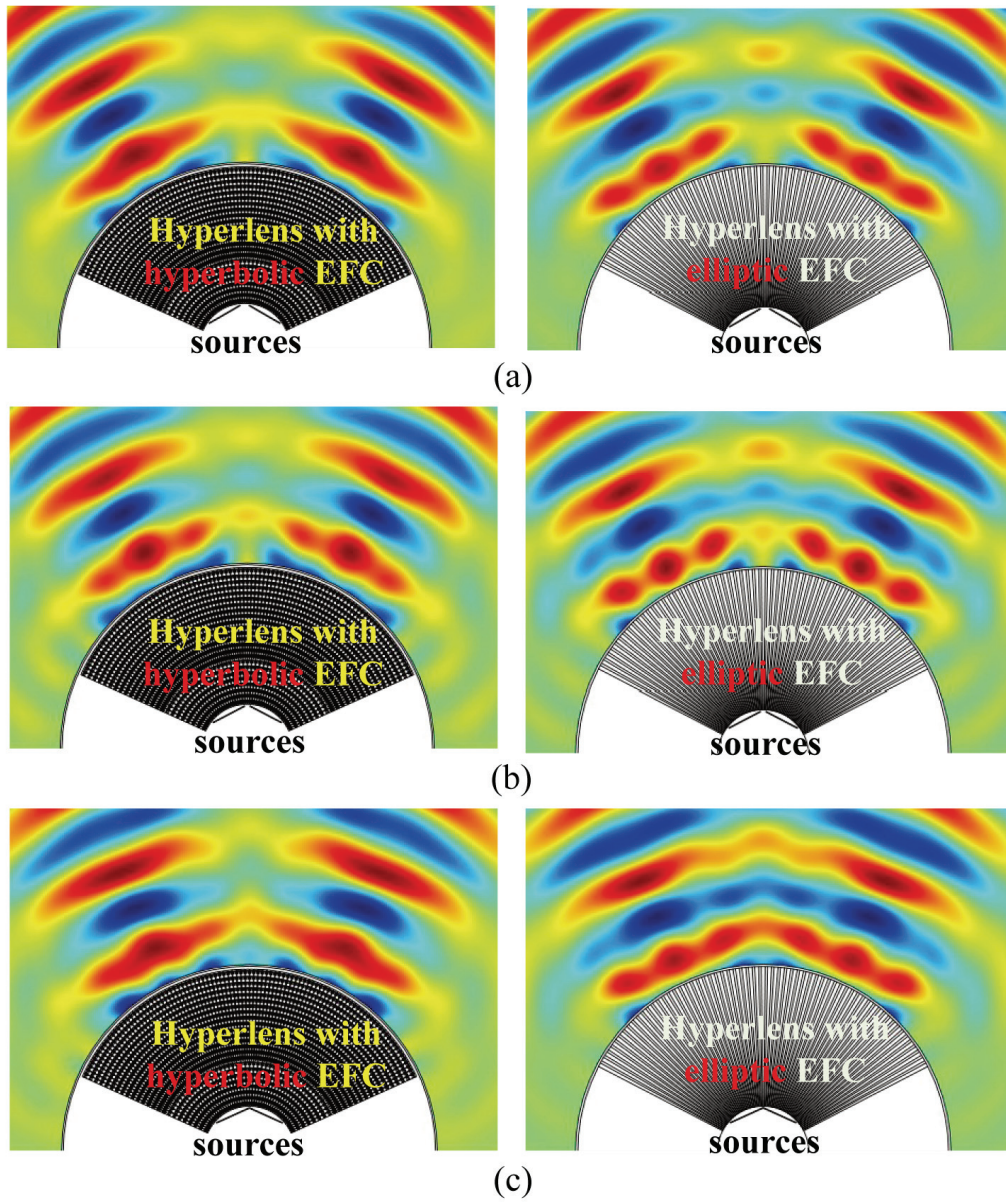


Fig. 3.17 Comparison of the S0 wave's displacement field transmitted from the proposed hyperlens (left) and the previously proposed one by Lee *et al.* [8] (right) while the relative distance between two sub-wavelength sources with respect to the actuation wavelength are (a) 0.48, (b) 0.45 and (c) 0.41, respectively

Chapter 4.

Experimental approach for the proposed elastic hyperlens

4.1 Chapter overview

In this chapter, the sub-wavelength resolution by the proposed elastic hyperlens is experimentally shown. Although the numerical simulation illustrated in the previous chapter well describe high performances of the proposed hyperlens, its realization and experimental verification is essential. The most important reason of the experimental approach is to check the effect of real material's loss. Every material has internal loss which is not considered in the previous simulations. Considering that material loss is generally hard to be exactly simulated, experimental approach is the most effective way in verifying hyperlens' real performance. This chapter is mainly dedicated to the experimental approach of the proposed hyperlens, including experimental setting, post-processing and comparison of the experimental results to those of the numerical results.

Perhaps the most critical issue in the experimental approach is that the operating frequency of 15 kHz is too low to be actuated by ultrasonic devices while it's too high to be actuated by vibration devices. One may consider that the operating frequency can be increased by reducing the overall hyperlens scale. However, if operating frequency is too high, corresponding hyperlens structure would be impossible to be manufactured by conventional machining process. For example, the minimum scale of water-jet cutting, which is used to fabricate the proposed hyperlens structure in this work, is usually ~ 0.5

mm, corresponds to ~ 15 kHz. If higher operating frequency is desired, small scale fabrication technique such as MEMS should be applied, which makes it harder to fabricate and perform experiments. Another issue is related to wave actuation. As explained in the previous section related to the numerical simulation, directivity of the wave source should be sufficiently high to successfully carry out experiments. This requires large source (almost 0.43λ , as in the simulation) having high directivity. The problem is that commercially available elastic wave actuators generally do not satisfy the requirements. The most generally used actuators, piezoelectric transducers, are hard to be applied in the experiments due to its low directivity. Another actuators, magnetostrictive transducers [65-70], have good directivity but usually have very small size and cannot be utilized in the experiment. Perhaps, EMAT [71] can be considered, but generated wave power is usually very low.

The issue related to the wave actuation is overcome in this work by developing new elastic wave actuator – called Giant Magnetostrictive Patch-type Transducer (G-MPT). To deal with the low frequency issue, input signal used in the wave actuation is modified, and normalization of measured signal is added in post-processing procedure. As a result, the sub-wavelength resolution of the proposed hyperlens is successfully shown by experiments.

4.2 Development of new elastic wave actuator for the experiment

Fig. 4.1 shows the schematic diagram of the proposed G-MPT. It consists of 5 pairs of

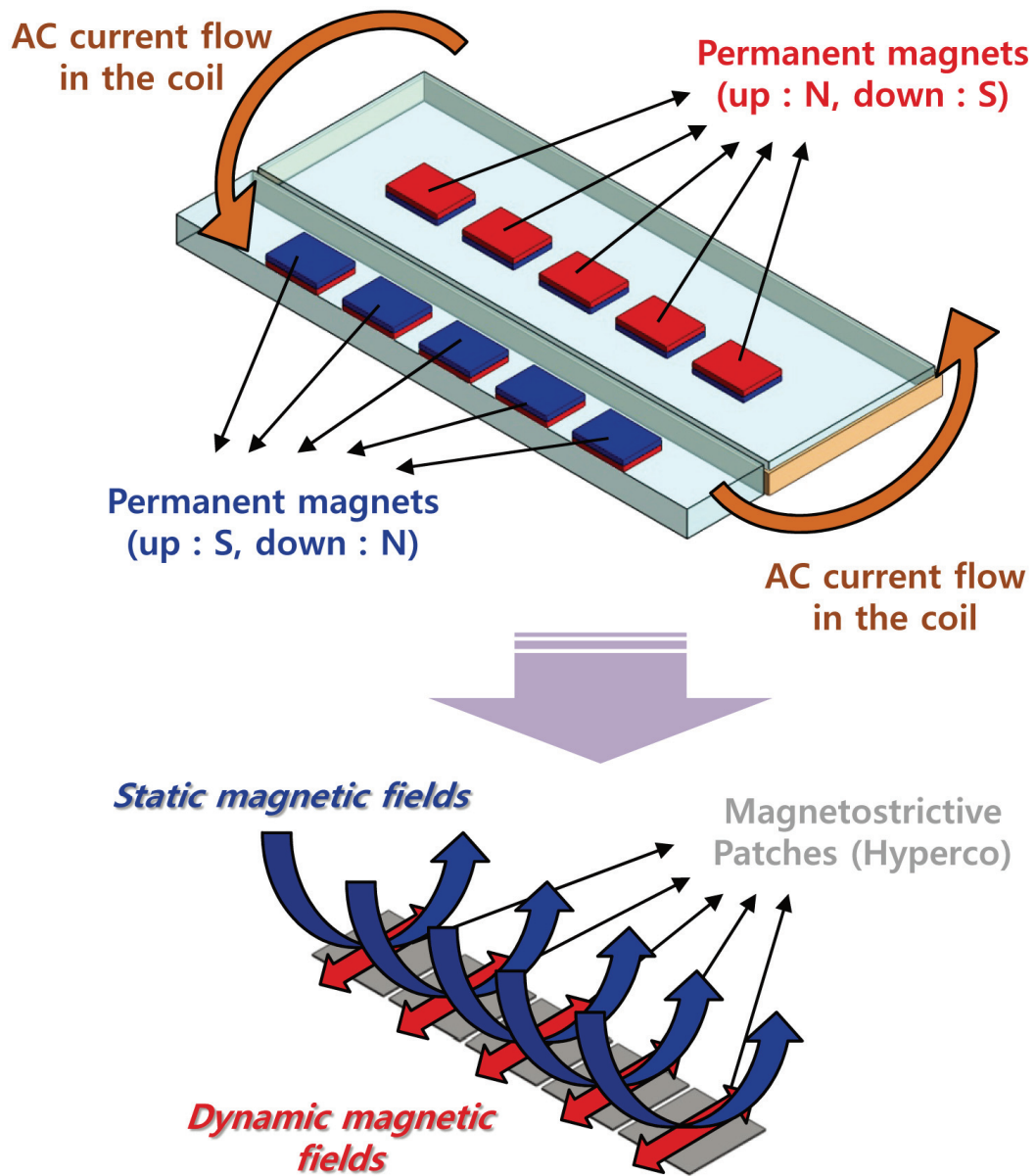


Fig. 4.1 Schematic illustration of the proposed G-MPT and its operating principle

permanent magnets and big coil loop where actuation current flows through. The magnets and coils are placed on the 5 magnetostrictive patches (in this work, Hyperco) each of which are $30 \times 30 \times 0.15$ mm bonded on the waveguide to actuate 15 kHz S0

wave mode to the hyperlens. Basically, G-MPT relies on the same operating principle with previously developed magnetostrictive patch-type transducers (MPT) [65-70]. It is based on magnetostriction effect [72, 73] which indicates coupling phenomena between elastic and magnetic field. If material has magnetostriction effect, it deforms when external magnetic field is applied, and its magnetization changes as stress is induced in the material.

The detailed operating principle of G-MPT is as follows. As actuation current flows through the coil loop, corresponding dynamic magnetic field is generated around the coil. Whenever a dynamic magnetic field is applied to each of the patch, a time-varying elastic deformation will be developed in the patch due to the magnetostrictive effect. Since the patch is bonded to a plate waveguide, the patch-bonded region of the waveguide will also dynamically deform. The resulting deformation then produces elastic wave propagating in the waveguide. Since the dynamic magnetic field is applied to each of the patch simultaneously, 5 magnetostrictive patches generate same amount of elastic wave at same time and same phase. Here, static magnetic field is applied to each of the patch by permanent magnets to facilitate the deformation due to magnetostriction. For more details about the physics behind general magnetostrictive patch-type transducers, see Ref. [74].

To give a full explanation of the operating principle of G-MPT, it is worth to see the physics related to magnetostriction. Imagine that both external magnetic flux density $d\mathbf{B}$ and mechanical strain $d\mathbf{e}$ are induced to a magnetostrictive material with unit

volume. For this case, the change of the internal energy can be calculated as [72]

$$dU^{tot} = dW^{elastic} + dW^{magnetic} = \boldsymbol{\sigma}^T d\mathbf{e} + \mathbf{H}^T d\mathbf{B} \quad (4.1)$$

where \mathbf{H} denotes magnetic field. On the other hand, Gibbs free energy G_{MS} of the magnetostrictive material at adiabatic condition can be expressed as

$$G_{MS} = U^{tot} - \boldsymbol{\sigma}^T \mathbf{e} - \mathbf{H}^T \mathbf{B}. \quad (4.2)$$

Differentiating equation (4.2) yields

$$dG_{MS} = dU^{tot} - d\boldsymbol{\sigma}^T \mathbf{e} - \boldsymbol{\sigma}^T d\mathbf{e} - d\mathbf{H}^T \mathbf{B} - \mathbf{H}^T d\mathbf{B}. \quad (4.3)$$

Substituting equation (4.1) to equation (4.3) results in following equation;

$$dG_{MS} = -d\boldsymbol{\sigma}^T \mathbf{e} - d\mathbf{H}^T \mathbf{B}. \quad (4.4)$$

From equation (4.4), the following equations can be derived as

$$e_{ij} = -\frac{\partial G_{MS}}{\partial \sigma_{ij}}, \quad B_i = -\frac{\partial G_{MS}}{\partial H_i}. \quad (4.5)$$

As can be seen in equation (4.5), if one differentiate e_{ij} with respect to H_i and B_i with respect to σ_{ij} , two results should be identical, i.e.,

$$\frac{\partial e_{ij}}{\partial H_i} = \frac{\partial B_i}{\partial \sigma_{ij}} = -\frac{\partial^2 G_{MS}}{\partial \sigma_{ij} \partial H_i} = d \quad (4.6)$$

In equation (4.6), d is a linear coupling coefficient which is called magnetostrictive coupling coefficient, or piezomagnetic coefficients.

From equation (4.6), it is obvious that both e_{ij} and B_i are functions of σ_{ij} and H_i .

This can be written as

$$\mathbf{e} = \mathbf{e}(\boldsymbol{\sigma}, \mathbf{H}), \quad \mathbf{B} = \mathbf{B}(\boldsymbol{\sigma}, \mathbf{H}) \quad (4.7)$$

Differentiating equation (4.7) yields

$$de_{ij} = \frac{\partial e_{ij}}{\partial \sigma_{kl}} d\sigma_{kl} + \frac{\partial e_{ij}}{\partial H_m} dH_m, \quad (4.8a)$$

$$dB_i = \frac{\partial B_i}{\partial \sigma_{jk}} d\sigma_{jk} + \frac{\partial B_i}{\partial H_l} dH_l. \quad (4.8b)$$

From elasticity and electromagnetic, it is already known that

$$\frac{\partial e_{ij}}{\partial \sigma_{kl}} = S_{ijkl}, \quad \frac{\partial B_i}{\partial H_l} = \mu_{il} \quad (4.9)$$

while S_{ijkl} and μ_{il} are compliance and permeability tensor, respectively. Substituting equation (4.9), (4.6) and (4.8), the following equation can be derived;

$$de_{ij} = S_{ijkl} d\sigma_{kl} + d_{ijm} dH_m, \quad (4.10a)$$

$$dB_i = d_{ijk} d\sigma_{jk} + \mu_{il} dH_l. \quad (4.10b)$$

Equation (4.10) is called linear magnetostrictive equation, or piezomagnetic equation. For small variation in mechanical or magnetic field, equation (4.10) can be used to describe the magnetostrictive material's behavior. Regarding that MPT is operated by small dynamic variation by the actuation signal of which amplitude is H_D under large static bias magnetic field H_S , equation (4.10) can be used without derivation operator for MPT. Therefore, equation (4.10) can be re-written in matrix form as

$$\mathbf{e} = \mathbf{S}\boldsymbol{\sigma} + \mathbf{d}^T \mathbf{H}_D, \quad (4.11a)$$

$$\mathbf{B}_D = \mathbf{d}\boldsymbol{\sigma} + \boldsymbol{\mu} \mathbf{H}_D. \quad (4.11b)$$

where stress and strain matrix are defined in equation (3.39) and (3.37b) while other matrix are defined as

$$\mathbf{S} = \mathbf{C}^{-1}, \quad (4.12a)$$

$$\mathbf{H}_D = [H_{Dx} \quad H_{Dy} \quad H_{Dz}]^T, \quad (4.12b)$$

$$\mathbf{B}_D = [B_{Dx} \quad B_{Dy} \quad B_{Dz}]^T, \quad (4.12c)$$

$$\boldsymbol{\mu} = \begin{bmatrix} \mu_{xx} & 0 & 0 \\ 0 & \mu_{yy} & 0 \\ 0 & 0 & \mu_{zz} \end{bmatrix}. \quad (4.12d)$$

Since equation (4.11) is defined for small variation around H_S , \mathbf{S} , \mathbf{d} and $\boldsymbol{\mu}$ should be function of H_S . However, changes of \mathbf{S} and $\boldsymbol{\mu}$ with respect to H_S are usually ignorable. Thus, only piezomagnetic coefficients \mathbf{d} are treated as a function of H_S .

Assuming plane magnetic field distribution for H_S , i.e., $H_{Sz} = 0$, \mathbf{d} is defined as [74]

$$\mathbf{d} = \begin{bmatrix} d_{11} & d_{12} & d_{13} & 0 & 0 & d_{16} \\ d_{21} & d_{22} & d_{23} & 0 & 0 & d_{26} \\ 0 & 0 & 0 & d_{34} & d_{35} & 0 \end{bmatrix}. \quad (4.13)$$

The related approach for detailed components in equation (4.13) is shown in Appendix.

Now, to see the wave generation mechanism by MPT, consider actuating signal flowing through the coil in fig. 4.1 generates dynamic magnetic field around the coil. Assuming time-harmonic signal, the generated dynamic magnetic field can be assumed to be harmonic function as

$$\mathbf{H}_D \approx \mathbf{H}_D \exp(i\omega t). \quad (4.14)$$

Here, since the overall system's scale is extremely smaller than the wavelength of electromagnetic wave in air, steady-state harmonic solution is assumed and wavevector

of electromagnetic wave is not considered in equation (4.14). Substituting equation (4.14) to equation (4.11a) yields

$$\mathbf{e} = \mathbf{S}\boldsymbol{\sigma} + \mathbf{d}^T \mathbf{H}_D \exp(i\omega t), \quad (4.15)$$

which can re-written with respect to $\boldsymbol{\sigma}$ as

$$\boldsymbol{\sigma} = (\mathbf{S})^{-1} \mathbf{e} - (\mathbf{S})^{-1} \mathbf{d}^T \mathbf{H}_D \exp(i\omega t). \quad (4.16)$$

Now, considering dynamic equation of motions in elasticity, following equation should be satisfied;

$$\boldsymbol{\rho} \frac{\partial^2 \mathbf{u}}{\partial t^2} - \bar{\nabla} \boldsymbol{\sigma} = 0 \quad (4.17)$$

while

$$\bar{\nabla} = \begin{bmatrix} \frac{\partial}{\partial x} & 0 & 0 & 0 & \frac{\partial}{\partial z} & \frac{\partial}{\partial y} \\ 0 & \frac{\partial}{\partial y} & 0 & \frac{\partial}{\partial z} & 0 & \frac{\partial}{\partial x} \\ 0 & 0 & \frac{\partial}{\partial x} & \frac{\partial}{\partial y} & \frac{\partial}{\partial z} & 0 \end{bmatrix} \quad (4.18)$$

In equation (4.17), $\boldsymbol{\rho}$ is density matrix and \mathbf{u} is displacement vector. Substituting equation (4.16) in equation (4.17), following equation can be derived;

$$\boldsymbol{\rho} \frac{\partial^2 \mathbf{u}}{\partial t^2} - \bar{\nabla} \cdot (\mathbf{S})^{-1} [\mathbf{e} - \mathbf{d}^T \mathbf{H}_D \exp(i\omega t)] = 0. \quad (4.19)$$

Re-arranging equation (4.19) yields

$$\boldsymbol{\rho} \frac{\partial^2 \mathbf{u}}{\partial t^2} - \bar{\nabla} \cdot (\mathbf{S})^{-1} \mathbf{e} = -\bar{\nabla} \cdot (\mathbf{S})^{-1} \mathbf{d}^T \mathbf{H}_D \exp(i\omega t). \quad (4.20)$$

From equation (4.20), it can be seen that magnetostrictive material under the dynamic magnetic field $\mathbf{H}_D \exp(i\omega t)$ can be treated as a mechanical system with external force

\mathbf{f}_{MS} defined as

$$\mathbf{f}_{MS} = -\bar{\nabla} \cdot (\mathbf{S})^{-1} \mathbf{d}^T \mathbf{H}_D \exp(i\omega t). \quad (4.21)$$

Therefore, elastic waves having angular frequency of ω are generated from the magnetostrictive material. This physical investigation clearly shows the operating principle of general MPT's, including G-MPT.

The major difference between G-MPT and the previous MPT's are that the proposed G-MPT can realize the S0 wave line source having 150 mm width by simultaneously actuating 5 magnetostrictive patches. Previous MPT's only have used one patch, which corresponds to the source size of almost 30 mm. Generally figure-of-eight coil is used in MPT's, but here only a single loop of coil is used since two G-MPT should be installed inside the hyperlens with very small separation distance, as in fig. 4.2. The number of

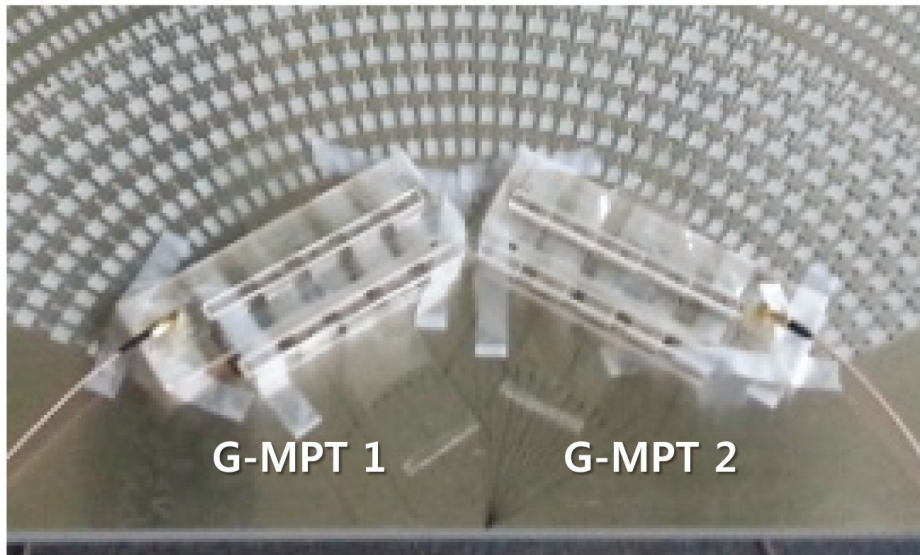


Fig. 4.2 Picture of two G-MPT installed inside the fabricated hyperlens

turns in the coil loop in the G-MPT is set to be 100 to strongly generate the actuation signal in the hyperlens structure. Note that usually 10~15 turns of coils were used in previous MPT's since higher coil turns rather reduce amplitude of generated waves. Since higher coil turns may provide high resistivity, the power of the actuation signal may not be sufficiently applied to the transducer due to the high impedance mismatch. However, for the hyperlens experiments, the actuation frequency is very low and impedance mismatch does not highly affect the overall energy transmission. Thus, high numbers of coil turns are used here. As a result, line sources having 150 mm with 15 kHz S₀ wave source can be successfully realized by G-MPT.

Note that G-MPT's are used for actuation only, and sensing is made by general MPT having figure-of-eight coil and single patch. For sensing, the large size of G-MPT does not provide accurate sensing at certain point. Also, the high number of coil turns in G-MPT makes it extremely weak to induction signal, which is unavoidable in experiments. It is shown that the use of G-MPT's in actuation and MPT in sensing allows effective experimental approach for the hyperlens.

4.3 Experimental procedure

4.3.1 Experimental setting

The detailed experimental setting for the hyperlens experiments is shown in fig. 4.3. As in fig. 4.3, two G-MPT's are placed directly inside the hyperlens as the S₀ wave sources

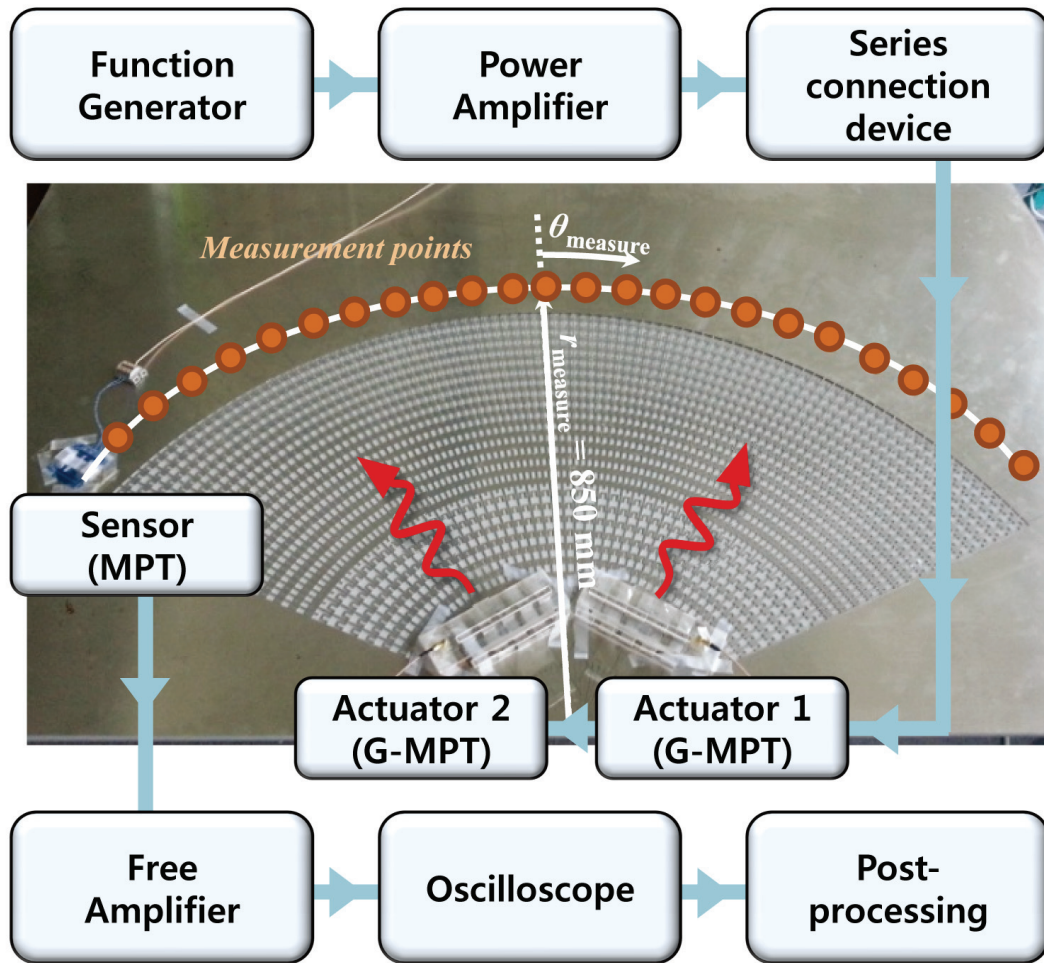


Fig. 4.3 Schematic diagram of the experimental procedure

modeled in the simulation. The detailed experimental procedures are as follows. First, the actuation signal is generated by function generator. The generated actuation signal is amplified in the power amplifier, and transferred to the G-MPT's to actuate elastic S0 wave. To make the wave generation at two G-MPT same, two G-MPT's are connected in series by series connection device. The transmitted S0 waves are measured by the MPT with $30 \times 30 \times 0.15 \text{ mm}$ patch at the measurement points which are arranged at $r_{\text{measure}} = 850 \text{ mm}$ away from the origin of the lens and every θ_{measure} of 5° from 0° to

120°, as shown in fig.4.3. After the measurements, each measured signals is re-amplified by free amplifier, and recorded by oscilloscope.

Since it is almost impossible to make two G-MPT's having exactly same electric property, the wave generation from two G-MPT's can be different from each other if each G-MPT is independently connected to the power amplifier. However, if two G-MPT's are connected in series, the amplitude of actuation signal transferred to each G-MPT (which is the amplitude of current flow in the coil of each G-MPT) is same regardless of difference between electric properties of two G-MPT's. Thus, the series connection device which connect two G-MPT's serially is essential in the hyperlens experiments. Fig. 4.4 shows the realized series connection device. Note that although the series connection device is self-made due to its inevitable need, the realized series connection device is somewhat crude. High loss and high noise are shown to be resulted from the device, and it would be preferred to use well-made series connection device if one tries to perform

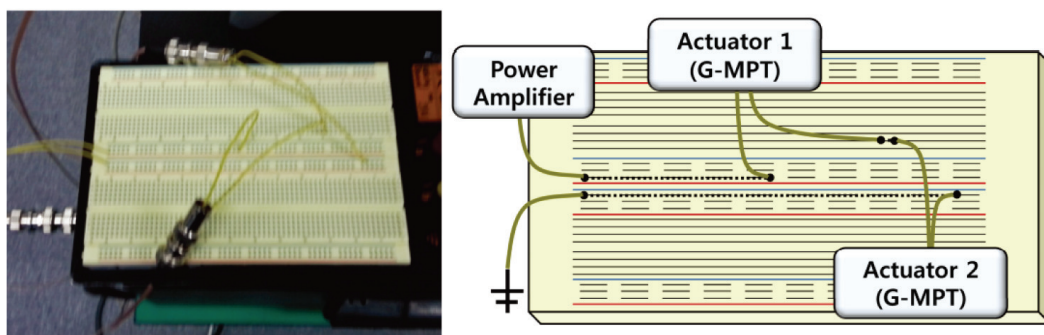


Fig. 4.4 Picture of the series connection device used in the experiment (left) and circuit configuration of the series connection device (right)

the hyperlens experiments.

The pulse-based experiments require information related to the arrival time, which means the time required for elastic wave from actuator to sensor. Usually, wave's arrival time $t_{arrival}$ can be analytically calculated as

$$t_{arrival} = l_{act-sens} / c_g \quad (4.22)$$

where $l_{act-sens}$ is the distance between actuator and sensor, and c_g is the wave's group velocity at the operating frequency. Since c_g can be analytically evaluated and $l_{act-sens}$ is given for experimental setting, $t_{arrival}$ can be analytically calculated by equation (4.22). In the hyperlens experiments, however, waves propagating radially inside the hyperlens experience various elastic metamaterials having different structure for each layer. Therefore, c_g varies radially and the evaluation of the arrival time is hard to be obtained by analytic calculation in equation (4.22). Thus, in this work, transient analysis is performed to figure out the arrival time. For S0 wave in 15 kHz, the arrival time of the S0 wave is figured out to be $230 \mu s$.

In the hyperlens experiments, input signal should be also carefully chosen. In general, following Gabor pulse is widely used in pulse-type elastic wave experiments as

$$u_{signal}(t) = \exp\left(\frac{-t^2}{2\bar{\sigma}^2}\right) \cos(2\pi t f_{center}) . \quad (4.23)$$

In equation (4.23), f_{center} is the center frequency, and $\bar{\sigma}$ is the constant which is related to the number of peaks in a pulse. Generally, $\bar{\sigma}$ is set to be almost 0.75,

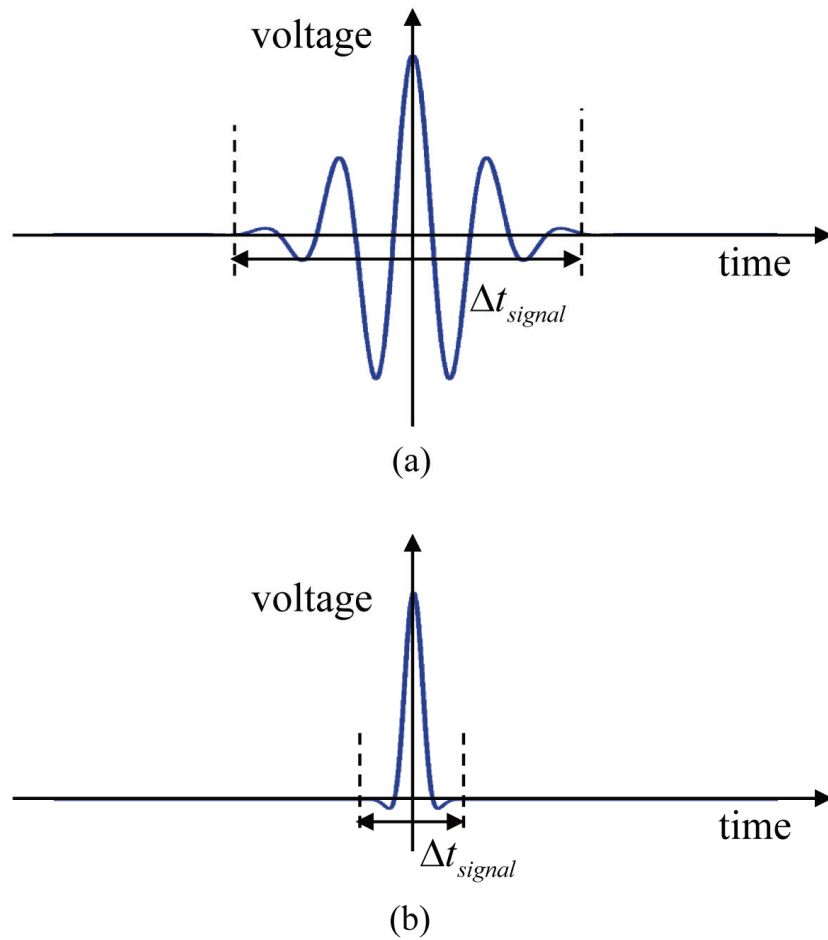


Fig. 4.5 (a) Plot of modulated Gaussian pulse generally used in ultrasonic elastic wave based inspection, (b) tailored modulated Gaussian pulse used in the hyperlens experiment

corresponds to 5 peaks in a pulse as shown in fig. 4.5 (a). However, this type of Gabor pulse cannot be used in the hyperlens experiments, due to induction signal. Since signal generation and amplification is based on high-voltage electric process, generation of dynamic electromagnetic field due to the signal generation and amplification is always accompanied. This dynamic electromagnetic field is also measure in sensor, resulting in induction signal. Since the generation and sensing of the dynamic electromagnetic field

is almost simultaneous process (speed of the dynamic electromagnetic field is usually same as the speed of the light), induction signal occurs around $t = 0$. For Gabor pulse of $\bar{\sigma} = 0.75$ with the center frequency f_{center} of 15 kHz, the length of the signal Δt_{signal} is more than $300 \mu s$. Since the arriving time of the actuated wave from actuator to sensor is $230 \mu s$, the input signal is still generated when wave started to be measured at sensor. Thus, the measured signal and induction signal are overlapped (note that this is not the case for general ultrasonic wave experiments where f_{center} is larger than ~ 100 kHz). By this reason, the Gabor pulse with $\bar{\sigma} = 0.15$, which is plotted in fig. 4.5 (b), is used instead, whose length Δt_{signal} is almost $70 \mu s$.

It should be emphasized that post-processing is essential in the hyperlens experiment. As $\bar{\sigma}$ becomes lower, the signal's frequency property becomes worse. In other word, Gabor pulse with low $\bar{\sigma}$ has wider frequency components. The signal of $\bar{\sigma} = 0.15$ with the center frequency f_{center} of 15 kHz consists of extremely wide frequency components. Thus, post-processing that decompose measured time signal $u(t)$ into frequency domain $U(f)$ as

$$U(f) = \int u(t) \exp(-i2\pi tf) dt \quad (4.24)$$

is required. Also, since it is extremely hard to actuate such a low frequency signal by ultrasonic device, post-processing is required to eliminate other possible noise in measured time signal.

4.3.2 Signal post-processing

Due to the wide frequency components of the actuating signal previously explained, post-processing of the measured signal is essential. After the transmitted waves from the hyperlens are measured at each measurement points, each measured signal is decomposed by short-time Fourier Transformation (STFT). For measured signal $u(t)$, STFT is performed as

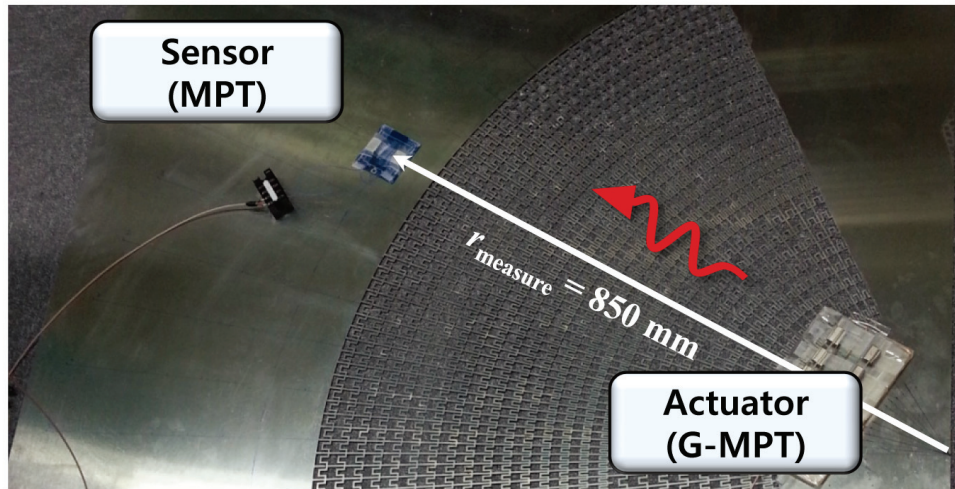
$$U(t, f) = \int u(\tau)g(\tau - t)\exp(-i2\pi\tau f)d\tau \quad (4.25)$$

where $g(t)$ is window function which is defined as

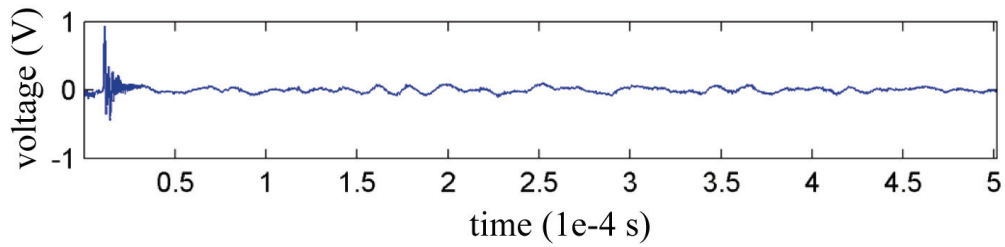
$$g(t) = \exp(-t^2 / 2\zeta). \quad (4.26)$$

Here, ζ is a constant that is given for STFT to control the size of window. If large window is used, frequency resolution of STFT increases while sacrificing time resolution. On the other hand, use of small window provides high time resolution but frequency resolution is lowered. Since the frequency ranges considered in the hyperlens experiments are very low, very large window size should be used.

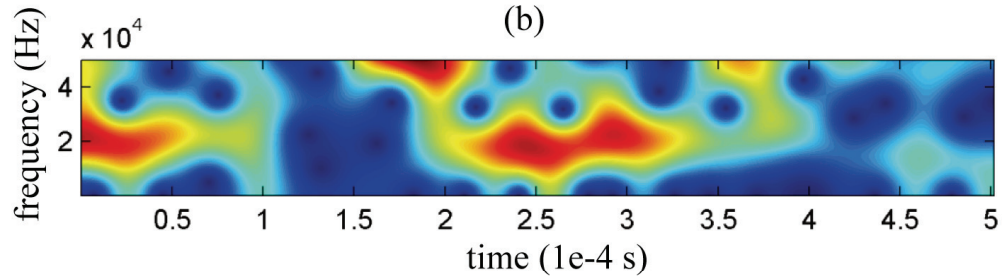
The detailed post-processing procedure is given in fig. 4.6. From the measured raw data, data calibration by averaging signal and STFT is performed. After STFT, signal of the desired frequency (in this research, 15 kHz) is extracted. Finally, the maximum values around the arrival time are evaluated at every measurement points.



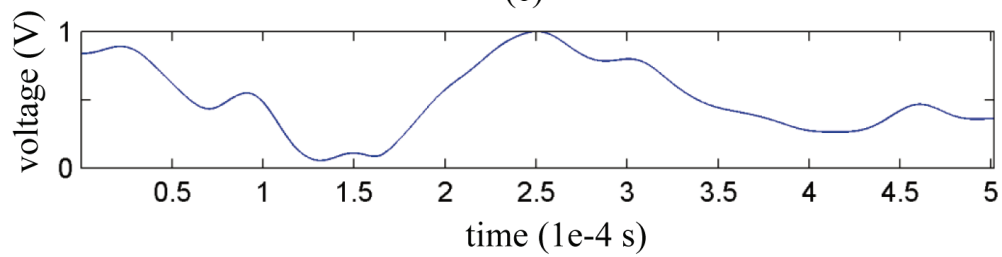
(a)



(b)



(c)



(d)

Fig. 4.6 (a) Picture of S0 wave measurement that transmitted from the hyperlens, (b) measured raw data from the sensor in (a), (c) plot of STFT results of the raw data in (b), (d) extracted data from STFT results in (c) at 15 kHz

The most important issue in the post-processing is data calibration by averaging. During signal recording by oscilloscope, the measured voltage values always have offset values ΔV_{offset} , as illustrated in fig. 4.7 (a). This offset value is originated from external setting of oscilloscope, and is constant independent of time. However, since STFT has limited frequency resolution, ΔV_{offset} tends to be decomposed into large amount of low frequency components. Thus, in the lower figure in fig. 4.7 (a), ΔV_{offset} may overlap the measured data. Note that if the window size is increased during STFT, frequency resolution may be improved and disturbance by ΔV_{offset} can be insignificant. However, increasing window size results in low resolution in time domain. Thus, the measured signal should be calibrated to get rid of ΔV_{offset} by following calculation,

$$f_{measured}^{calib}(t) = f_{measured}(t) - \frac{\int_0^{t'} f_{measured}(t) dt}{t'} . \quad (4.27)$$

where $f_{measured}(t)$ is the measured raw data at the measurement point and $f_{measured}^{calib}(t)$ is the resulting calibrated data. t' indicates the maximum time of the measurement. Equation (4.27) can be understood by compensating ΔV_{offset} with the averaged value of the measured raw signal.

The calibration shown in equation (4.27) seems simple, but it significantly reduces effect of ΔV_{offset} in STFT. In fig. 4.7 (b), STFT results after the calibration in equation (4.27) is plotted. Comparing the results in fig. 4.7 (a) in which calibration is not applied, fig. 4.7 (b) provides clear STFT result. As can be observed in fig. 4.7, data calibration plays

important role in post-processing of the hyperlens experiments.

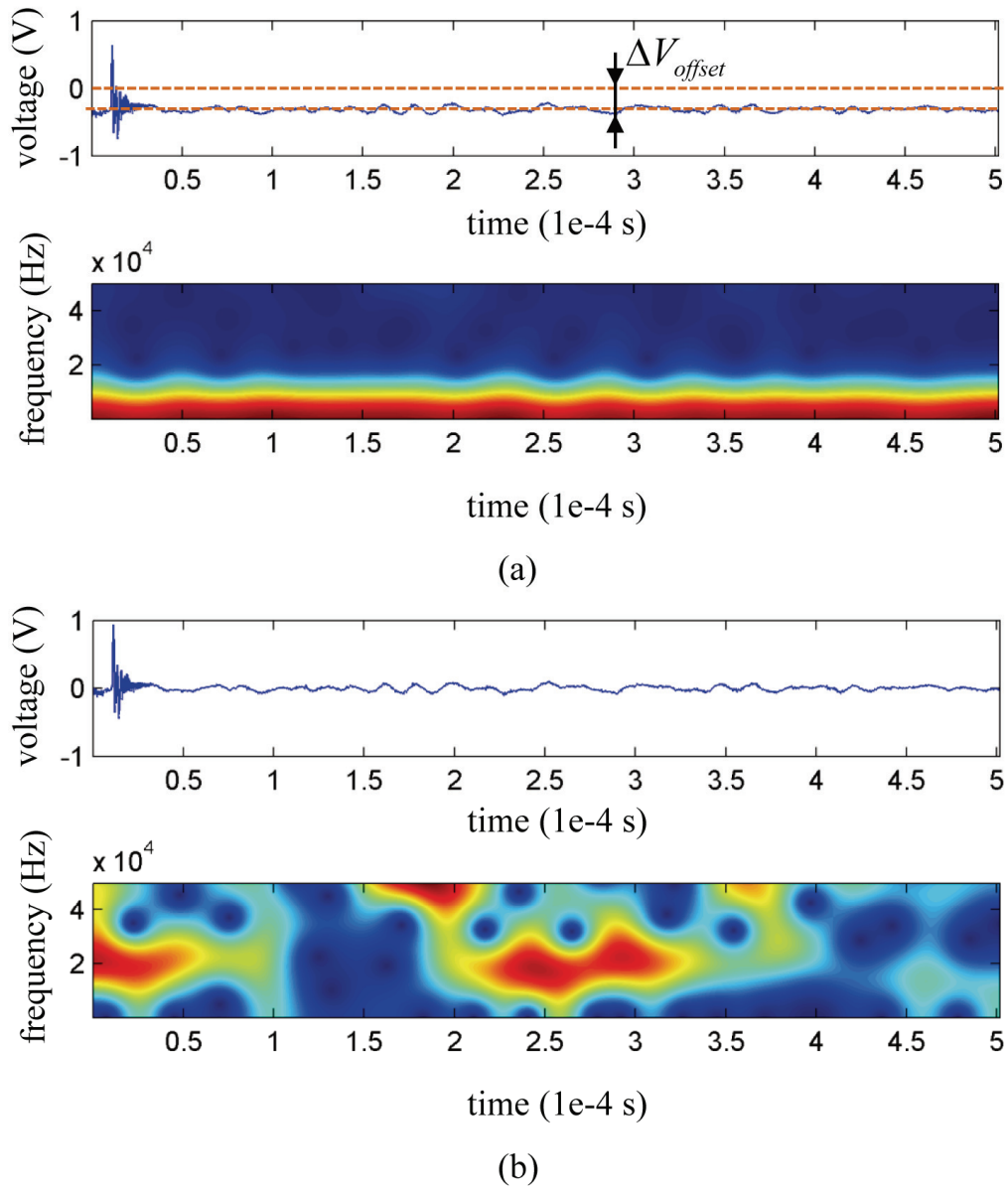


Fig. 4.7 (a) STFT results without data calibration, (b) improved STFT results after data calibration

4.4 Experimental results

From the experimental procedure discussed previously, experimental approach for the hyperlens with sub-wavelength sources is performed. The experimental results are then compared with the simulation results. As pointed out in Ref. [74], results obtained from harmonic simulation are usually multi-modal and displacement field of the desired mode should be extracted. In other word, there exists not only S0 wave but also SH0 wave in displacement fields calculated by harmonic simulation. In experiments, each wave mode has unique group velocity and thus can be distinguished in time domain. However, in time-harmonic simulation, wave speed difference has no meaning and thus each wave mode should be distinguished. For waves propagating along radial direction, radial displacement component u_r corresponds to S0 wave mode as shown in [74]. Thus, only S0 wave transmission from the hyperlens can be measured in simulation and comparison between experimental and simulation results can be made.

Fig. 4.8 shows the plot of the simulation and experimental results. Good agreements can be observed between two results, except those results in $\theta_{\text{measure}} = 90^\circ$. The disagreement in $\theta_{\text{measure}} = 90^\circ$ is due to the unavoidable side lobes of transducer. As shown in Refs. [68,69,74], transducers based on magnetostriction dominantly generate guided waves along certain direction, but also slightly generate waves along the direction normal to the dominant direction. Nevertheless, the results in fig. 4.8 show that sub-wavelength resolution at far field can be obtained by the proposed elastic hyperlens.

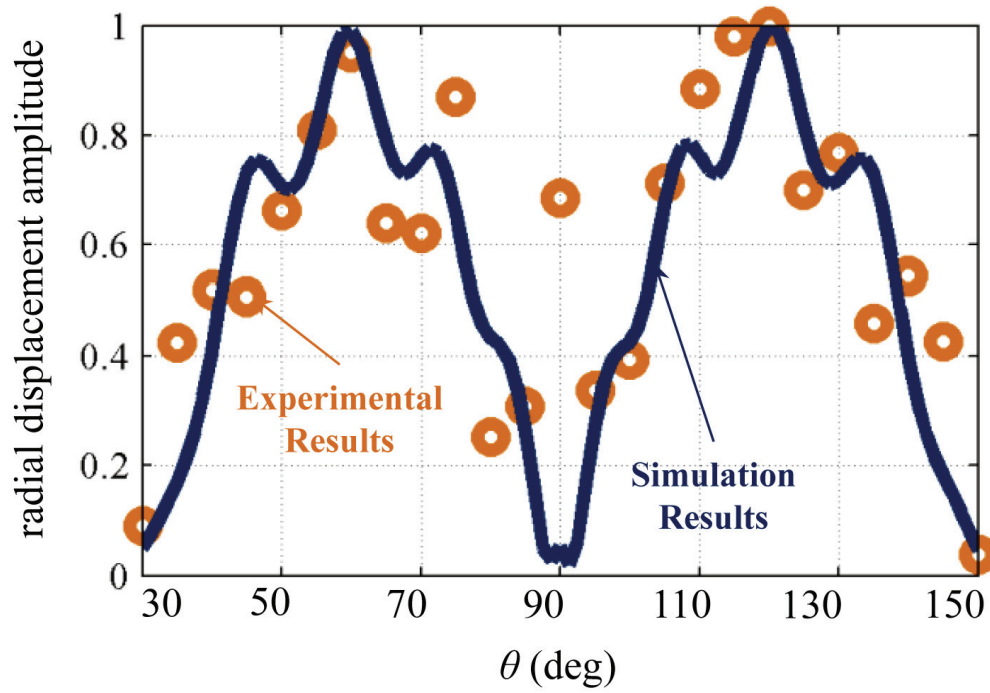


Fig. 4.8 Comparison of the numerical and experimental results of the S0 wave displacements at the measurement points

Chapter 5.

Analytic approach for the proposed elastic hyperlens

5.1 Chapter overview

This chapter is mainly dedicated to establishing analytic modeling for the proposed hyperbolic elastic metamaterial and elastic hyperlens. In the previous chapters, the elastic hyperlens having much improved resolution than previous one is proposed, and its performance is verified by both numerical simulation and experiments. However, effect of each design parameters in the proposed hyperbolic elastic lens is still unknown. To see the effect of each design parameters, analytic modeling for the proposed hyperbolic elastic metamaterial should be formulated. The analytic modeling can show the relation between overall wave characteristics and design variables. Accordingly, further researches such as design optimization are expected to be carried out based on the analytic method.

As a first step for analytic approach of the proposed hyperlens, a schematic mass-spring model is introduced to analytically illustrate the operating principle of the proposed hyperlens. Although basic mass-spring modeling is already considered in chapter 3, the analytic investigation made in this chapter is much more tailored for the proposed hyperbolic metamaterial. The considered mass-spring system is illustrated in fig. 5.1. By assuming periodic wave solution, wave dispersion characteristics can be calculated analytically as the functions of spring coefficients and mass coefficients. Here, the

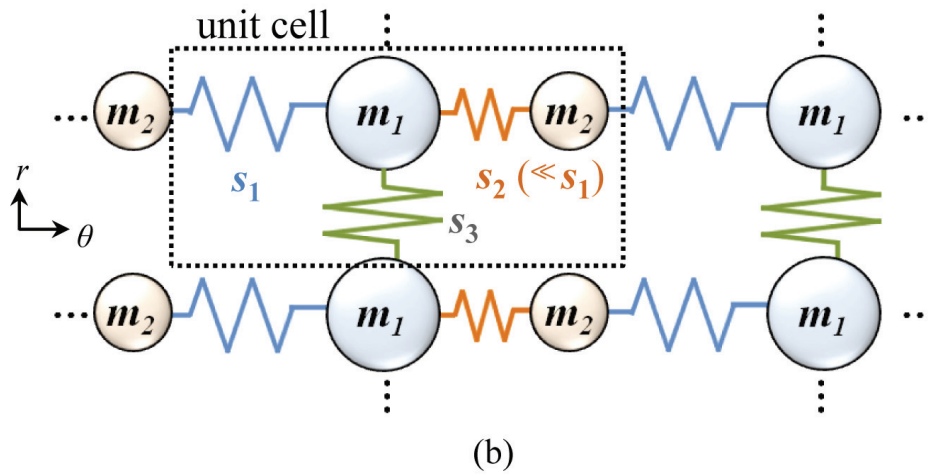
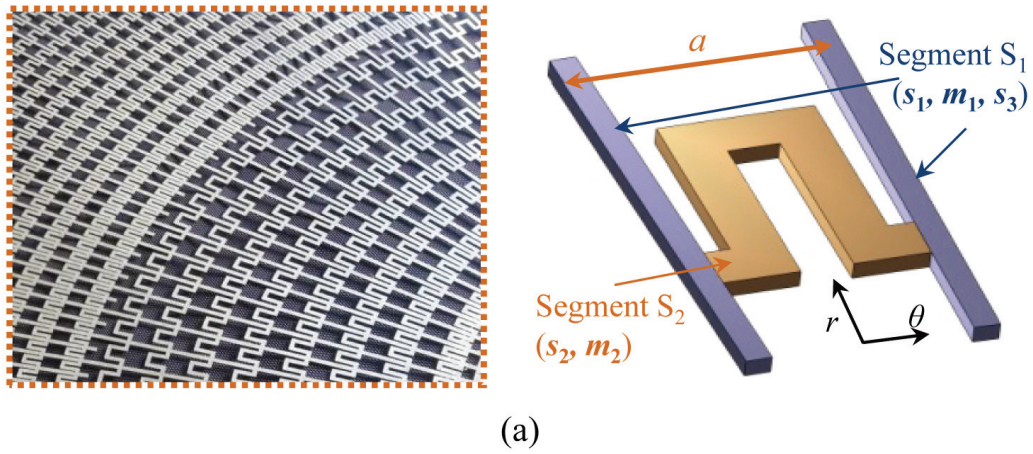


Fig. 5.1 (a) Definition of Segment S_1 and S_2 , (b) equivalent mass-spring model for analytic investigation of the proposed elastic metamaterial

different mass-spring modeling should be established along two different directions since different physics take place. Along circumferential direction, periodicity of two different mass and springs are major physical factor [75], while along radial direction, shear-resonance plays dominant role [76]. From the analysis, the physics behind the proposed hyperbolic elastic metamaterial can be revealed out.

Consequently, the equivalent mass and spring coefficients are derived from the geometric variables of the hyperbolic elastic metamaterial. Due to the corrugated configuration of the proposed hyperbolic elastic metamaterial, it is quite complicated to evaluate equivalent spring coefficients by calculating all reaction inside the structure. Instead, energy method is applied in calculating spring coefficients. From partial derivatives of the total elastic energy of the structure, and by properly imposing boundary conditions, the equivalent spring coefficients can be calculated. Finally, based on the established analytic modeling, basic design problem of the hyperbolic elastic metamaterial will be given. Similar to the sample design problem dealt in this chapter, the analytic modeling of the proposed hyperbolic elastic metamaterial and hyperlens can provide a new insight in related design and optimization problems.

5.2 Analytic modeling along circumferential directions

5.2.1 Analytic calculation of the dispersion relation of mass-spring model along circumferential directions

From the mass-spring system shown in fig. 5.1, consider wave propagation along circumferential direction. Note that unlike in chapter 3, both springs s_1 and s_2 will be considered simultaneously here. Along circumferential direction, the mass-spring system can be seen as a 2-degree of freedom system as shown in fig. 5.2 (a). Considering the free-body diagram shown in fig. 5.2 (b,c), the equation of the motion for each mass m_1 and m_2 can be written as

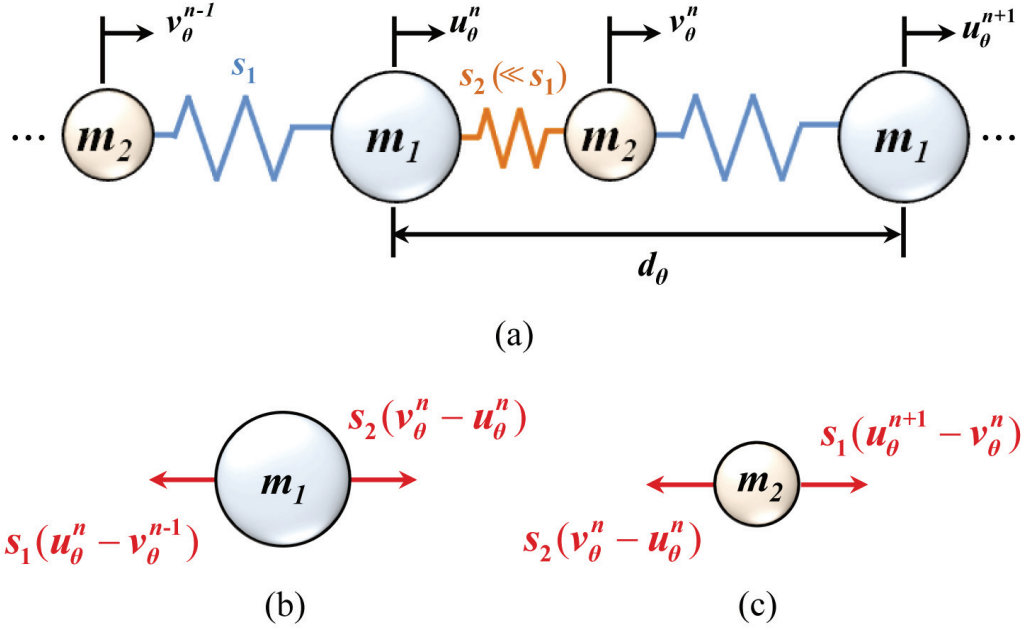


Fig. 5.2 (a) Equivalent mass-spring model for circumferential direction, and corresponding free-body diagrams of (b) m_1 and (c) m_2

$$m_1 \ddot{u}_\theta^n = s_2(v_\theta^n - u_\theta^n) - s_1(u_\theta^n - v_\theta^{n-1}) \quad (5.1a)$$

$$m_2 \ddot{v}_\theta^n = s_1(u_\theta^{n+1} - v_\theta^n) - s_2(v_\theta^n - u_\theta^n). \quad (5.1b)$$

Now, to calculate wave dispersion relation of the mass-spring system, periodic wave solution is assumed as

$$u_\theta^n = U_\theta \exp[i(\omega t - k_\theta \theta)], \quad (5.2a)$$

$$v_\theta^n = V_\theta \exp[i(\omega t - k_\theta \theta)]. \quad (5.2b)$$

From equation (5.2), u_θ^{n+1} and v_θ^{n-1} can be expressed as $u_\theta^{n+1} = \exp(-ik_\theta d_\theta) u_\theta^n$ and $v_\theta^{n-1} = \exp(ik_\theta d_\theta) v_\theta^n$. Therefore, equation (5.1) can be re-written as

$$-\omega^2 m_1 u_\theta^n = s_2(v_\theta^n - u_\theta^n) - s_1(u_\theta^n - \exp(ik_\theta d_\theta) v_\theta^n) \quad (5.3a)$$

$$-\omega^2 m_2 v_\theta^n = s_1 (\exp(-ik_\theta d_\theta) u_\theta^n - v_\theta^n) - s_2 (v_\theta^n - u_\theta^n). \quad (5.3b)$$

Here, it is more convenient to express the equation (5.3) as a matrix form in evaluating the dispersion relation as

$$\mathbf{A} \begin{bmatrix} u_\theta^n \\ v_\theta^n \end{bmatrix} = 0, \quad \mathbf{A} = \begin{bmatrix} m_1 \omega^2 - (s_1 + s_2) & \exp(ik_\theta d_\theta) s_1 + s_2 \\ \exp(-ik_\theta d_\theta) s_1 + s_2 & m_2 \omega^2 - (s_1 + s_2) \end{bmatrix}. \quad (5.4)$$

From equation (5.4), the dispersion relation can be obtained by $\det(\mathbf{A}) = 0$, which can be written as

$$m_1 m_2 \omega^4 - (m_1 + m_2)(s_1 + s_2) \omega^2 + (s_1 + s_2)^2 - [s_1^2 + s_1 s_2 \{\exp(ik_\theta d_\theta) + \exp(-ik_\theta d_\theta)\} + s_2^2] = 0. \quad (5.5)$$

Equation (5.5) can be more simplified by using $2 \cos x = \exp(-ix) + \exp(ix)$ as following.

$$-m_1 m_2 \omega^4 + (m_1 + m_2)(s_1 + s_2) \omega^2 = 2s_1 s_2 (1 - \cos(k_\theta d_\theta)) \quad (5.6)$$

As a result, the following dispersion relation with respect to k_θ is derived

$$k_\theta = \cos^{-1} \left[\frac{m_1 m_2 \omega^4 - (m_1 + m_2)(s_1 + s_2) \omega^2}{2s_1 s_2} + 1 \right] / d_\theta \quad (5.7)$$

By using equation (5.7), the dispersion curve along circumferential direction can be calculated analytically by calculating k_θ for given frequencies ω [75].

Now, consider wave propagation at low frequency where ω is very low. In very low frequency, equation (5.6) is simplified as following

$$1 - \cos(k_\theta d_\theta) = \frac{-m_1 m_2 \omega^4 + (m_1 + m_2)(s_1 + s_2) \omega^2}{2s_1 s_2}. \quad (5.8)$$

In equation (5.8), the first term which is the function of 4th order of ω can be ignored which results in

$$1 - \cos(k_\theta d_\theta) \approx \frac{(m_1 + m_2)(s_1 + s_2)}{2s_1 s_2} \omega^2. \quad (5.9)$$

Also, since $s_2 \ll s_1$, equation (5.9) can be re-arranged as

$$1 - \cos(k_\theta d_\theta) \approx \frac{(m_1 + m_2)}{2s_2} \omega^2. \quad (5.10)$$

It is interesting that equation (5.10) is exactly same for equation (3.21), where only s_2 is considered. In fact, for low frequency, both springs s_1 and s_2 exhibit in-phase motions and equivalent single spring assumption made in chapter 3 is available. However, as frequency increases, the significance of 4th order term in equation (5.8) becomes high, and equation (3.21) may show low accuracy.

5.2.2 Calculation of the equivalent mass/spring coefficients along circumferential directions

To see equivalence between the proposed unit cell shown in fig. 5.1 (a) and the mass-spring system shown in fig. 5.1 (b), the equivalent mass and spring coefficients of the proposed unit cell should be calculated. As explained previously, θ_{cell} is assumed to be zero since $\theta_{\text{cell}} \ll 1$ and x - y Cartesian coordinate is used in analytic calculation, i.e., r axis is assumed to be same as y axis and θ axis is assumed to be same as x axis.

Starting from equivalent mass coefficient, since there are no resonators inside each

segment, the equivalent mass coefficients are almost constant with respect to frequency change and they can be evaluated as

$$m_1 = \rho V_A, \quad m_2 = \rho V_B \quad (5.11)$$

where V_A and V_B indicate the volume of Segment S_1 and S_2 , respectively, and ρ is the density of the material (aluminum for this work).

Also, considering the wave propagation in the Segment S_1 along y direction, the Segment S_1 can be viewed as a bar structure under compression as in figs. 5.3 (a). For the structure shown in figs. 5.3 (a), the structure should satisfy the boundary condition which is given as

$$\sigma_{zz} = e_{yy} = 0 \quad (5.12)$$

while σ and e denote stress and strain, respectively. To evaluate the equivalent spring coefficient from equation (5.12), general 3-dimensional stress-strain relation is reduced to proper 1-dimensional equation. Start from the boundary condition $\sigma_{zz} = 0$, 3-dimensional stress-strain relation is reduced to well known 2-dimensional stress-strain relation under plane stress condition as

$$\begin{bmatrix} E/(1-\nu^2) & -\nu E/(1-\nu^2) & 0 \\ -\nu E/(1-\nu^2) & E/(1-\nu^2) & 0 \\ 0 & 0 & G \end{bmatrix} \begin{bmatrix} e_{xx} \\ e_{yy} \\ e_{xy} \end{bmatrix} = \begin{bmatrix} \sigma_{xx} \\ \sigma_{yy} \\ \sigma_{xy} \end{bmatrix}. \quad (5.13)$$

In equation (5.13), E , G and ν denote Young's modulus, shear modulus and Poisson's ratio, respectively. Applying other boundary condition $e_{yy} = 0$ yields following 1-dimensional stress-strain relation;

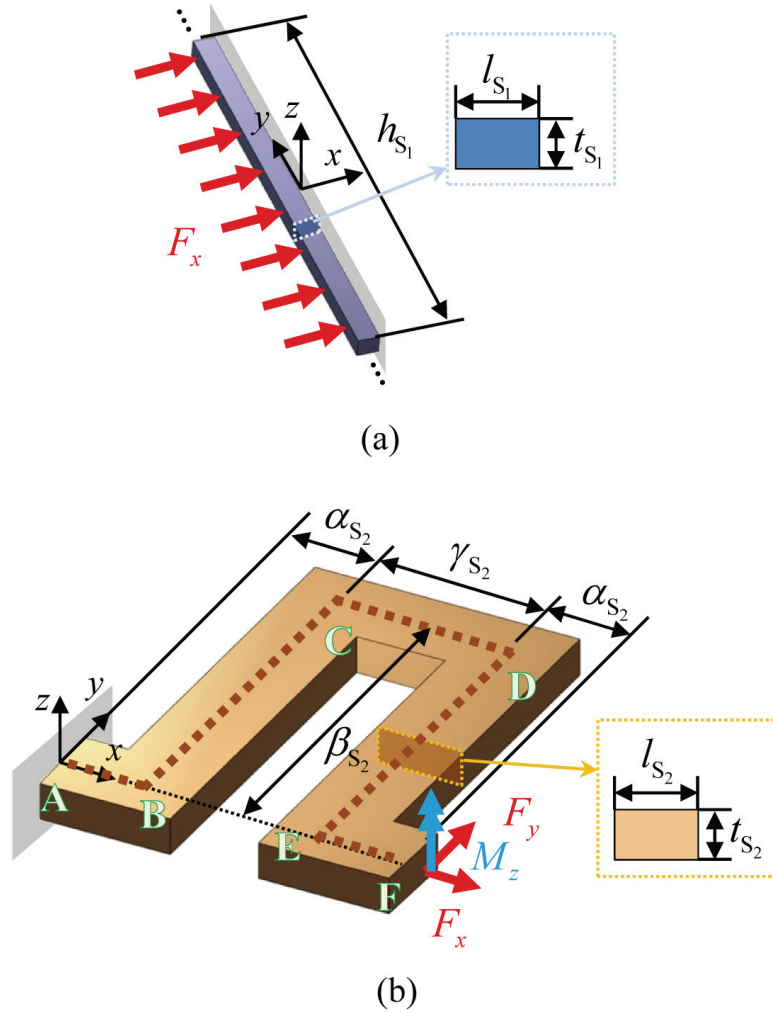


Fig. 5.3 Mechanical models for stiffness analysis of (a) Segment S_1 and (b) Segment S_2

$$\frac{E}{(1-\nu^2)} e_{xx} = \sigma_{xx} \quad (5.14)$$

To calculate equivalent spring coefficient from equation (5.14), following 1-dimensional equilibrium and strain-displacement relation are used;

$$\sigma_{xx} = F / (h_{S_1} t_{S_1}), \quad e_{xx} = u / l_{S_1} \quad (5.15)$$

where geometric variables h_{s_1} , t_{s_1} and l_{s_1} is defined in fig. 5.3 (a). Substituting equation (5.15) to equation (5.14), the equivalent spring coefficient s_1 can be derived as

$$s_1 = \frac{Eh_{s_1}t_{s_1}}{l_{s_1}(1-\nu^2)}. \quad (5.16)$$

On the other hand, Segment S_2 has complex configuration and should be considered as an assembly of several beam structures. To calculate s_2 , the energy method proposed by Kim *et al.* [77] is applied. Here, total elastic energy inside the Segment S_2 under the induction of forces F_x , F_y and moment M_z is calculated. For the beam segments (beam A-B, B-C, C-D, D-E and E-F in fig. 5.3 (b)) constituting Segment S_2 , the elastic energies due to the induced forces and moments are

$$U_{AB} = \int_0^{\alpha_{s_2}} \frac{[F_y(\gamma_{s_2} + 2\alpha_{s_2} - x) + M_z]^2}{2EI_{s_2}} dx \quad (5.17a)$$

$$U_{BC} = \int_0^{\beta_{s_2}} \frac{[F_x y + F_y(\gamma_{s_2} + \alpha_{s_2}) + M_z]^2}{2EI_{s_2}} dy \quad (5.17b)$$

$$U_{CD} = \int_0^{\gamma_{s_2}} \frac{[F_x \beta_{s_2} + F_y(\gamma_{s_2} + \alpha_{s_2} - x) + M_z]^2}{2EI_{s_2}} dx \quad (5.17c)$$

$$U_{DE} = \int_0^{\beta_{s_2}} \frac{[F_x y + F_y \alpha_{s_2} + M_z]^2}{2EI_{s_2}} dy \quad (5.17d)$$

$$U_{EF} = \int_0^{\alpha_{s_2}} \frac{[F_y(\alpha_{s_2} - x) + M_z]^2}{2EI_{s_2}} dx \quad (5.17e)$$

where $I_{s_2} = l_{s_2} t_{s_2}^3 / 12$ is the moment of inertia of each beam segment. Note that

compressive motion of each segment is ignored since spring coefficient related to the compression is much larger than that related to the bending motion.

From equations (5.17), the displacements δ_x , δ_y and θ_z at point F can be derived by the partial derivatives of the total energy $U_{tot} = U_{AB} + U_{BC} + U_{CD} + U_{DE} + U_{EF}$ with respect to the external forces [78], as

$$\begin{aligned}\delta_x &= \frac{\partial U_{tot}}{\partial F_x} \\ &= \left[\left(\frac{2}{3} \beta_{S_2}^3 + \beta_{S_2}^2 \gamma_{S_2} \right) F_x \right. \\ &\quad + \left[\frac{(\gamma_{S_2} + 2\alpha_{S_2}) \beta_{S_2}^2}{2} + \frac{\{(\gamma_{S_2} + \alpha_{S_2})^2 - \alpha_{S_2}^2\} \beta_{S_2}}{2} \right] F_y \\ &\quad \left. + (\beta_{S_2}^2 + \beta_{S_2} \gamma_{S_2}) M_z \right] / EI_{S_2}\end{aligned}\quad (5.18a)$$

$$\begin{aligned}\delta_y &= \frac{\partial U_{tot}}{\partial F_y} \\ &= \left[\left[\frac{(\gamma_{S_2} + 2\alpha_{S_2}) \beta_{S_2}^2}{2} + \frac{\{(\gamma_{S_2} + \alpha_{S_2})^2 - \alpha_{S_2}^2\} \beta_{S_2}}{2} \right] F_x \right. \\ &\quad + \left[\frac{(\gamma_{S_2} + 2\alpha_{S_2})^3}{3} + \{(\gamma_{S_2} + \alpha_{S_2})^2 + \alpha_{S_2}^2\} \beta_{S_2} \right] F_y \\ &\quad \left. + \left[\frac{(\gamma_{S_2} + 2\alpha_{S_2})^2}{2} + (\gamma_{S_2} + 2\alpha_{S_2}) \beta_{S_2} \right] M_z \right] / EI_{S_2}\end{aligned}\quad (5.18b)$$

$$\begin{aligned}\theta_z &= \frac{\partial U_{tot}}{\partial M_z} \\ &= \left[(\beta_{S_2}^2 + \beta_{S_2} \gamma_{S_2}) F_x \right. \\ &\quad + \left[\frac{(\gamma_{S_2} + 2\alpha_{S_2})^2}{2} + (\gamma_{S_2} + 2\alpha_{S_2}) \beta_{S_2} \right] F_y \\ &\quad \left. + (2\alpha_{S_2} + 2\beta_{S_2} + \gamma_{S_2}) M_z \right] / EI_{S_2}\end{aligned}\quad (5.18c)$$

Now, to calculate s_2 , Castigliano theorem is used along with the boundary conditions at point F such that $\delta_y = 0$ and $\theta_z = 0$. From the condition, following conditions that relate forces F_x , F_y and moment M_z to satisfy the boundary condition can be derived from equation (5.18b) and (5.18c) as follows;

$$\begin{aligned} & \left[\frac{(\gamma_{s_2} + 2\alpha_{s_2})^3}{3} + \{(\gamma_{s_2} + \alpha_{s_2})^2 + \alpha_{s_2}^2\} \beta_{s_2} \right] \frac{F_y}{F_x} \\ & + \left[\frac{(\gamma_{s_2} + 2\alpha_{s_2})^2}{2} + (\gamma_{s_2} + 2\alpha_{s_2}) \beta_{s_2} \right] \frac{M_z}{F_x} \\ & = -\frac{(\gamma_{s_2} + 2\alpha_{s_2}) \beta_{s_2}^2}{2} - \frac{\{(\gamma_{s_2} + \alpha_{s_2})^2 - \alpha_{s_2}^2\} \beta_{s_2}}{2} \end{aligned} \quad (5.19a)$$

$$\begin{aligned} & \left[\frac{(\gamma_{s_2} + 2\alpha_{s_2})^2}{2} + (\gamma_{s_2} + 2\alpha_{s_2}) \beta_{s_2} \right] \frac{F_y}{F_x} + (2\alpha_{s_2} + 2\beta_{s_2} + \gamma_{s_2}) \frac{M_z}{F_x} \\ & = -\beta_{s_2}^2 - \beta_{s_2} \gamma_{s_2} \end{aligned} \quad (5.19b)$$

Based on equations (5.19a) and (5.19b), the spring coefficients s_2 can be calculated from equation (5.18a) as

$$\begin{aligned} \frac{1}{s_2} &= \frac{\delta_x}{F_x} \\ &= \left[\frac{2}{3} \beta_{s_2}^3 + \beta_{s_2}^2 \gamma_{s_2} + \left[\frac{(\gamma_{s_2} + 2\alpha_{s_2}) \beta_{s_2}^2}{2} \right. \right. \\ & \quad \left. \left. + \frac{\{(\gamma_{s_2} + \alpha_{s_2})^2 - \alpha_{s_2}^2\} \beta_{s_2}}{2} \right] \frac{F_y}{F_x} + (\beta_{s_2}^2 + \beta_{s_2} \gamma_{s_2}) \frac{M_z}{F_x} \right] / EI_{s_2} \end{aligned} \quad (5.20)$$

where F_y / F_x and M_z / F_x can be evaluated by solving equations (5.19) as following;

$$\begin{aligned}
& \begin{bmatrix} \frac{(\gamma_{s_2} + 2\alpha_{s_2})^3}{3} + \{(\gamma_{s_2} + \alpha_{s_2})^2 + \alpha_{s_2}^2\}\beta_{s_2} & \frac{(\gamma_{s_2} + 2\alpha_{s_2})^2}{2} + (\gamma_{s_2} + 2\alpha_{s_2})\beta_{s_2} \\ \frac{(\gamma_{s_2} + 2\alpha_{s_2})^2}{2} + (\gamma_{s_2} + 2\alpha_{s_2})\beta_{s_2} & 2\alpha_{s_2} + 2\beta_{s_2} + \gamma_{s_2} \end{bmatrix} \begin{bmatrix} \frac{F_y}{F_x} \\ \frac{M_z}{F_x} \end{bmatrix} \\
& = \begin{bmatrix} -\frac{(\gamma_{s_2} + 2\alpha_{s_2})\beta_{s_2}^2}{2} - \frac{\{(\gamma_{s_2} + \alpha_{s_2})^2 - \alpha_{s_2}^2\}\beta_{s_2}}{2} \\ -\beta_{s_2}^2 - \beta_{s_2}\gamma_{s_2} \end{bmatrix} \quad (5.21)
\end{aligned}$$

From equation (5.20) and (5.21), the equivalent spring coefficient s_2 can be explicitly calculated from geometric variables.

It should be emphasized that in calculating longitudinal spring coefficient s_2 , Euler beam theory is used. This can be admitted since the bending occurred in the shorter beam segments (A-B, C-D and E-F in fig. 5.3 (b)) is almost ignorable compared to that in the longer beam segments (B-C and D-E in fig. 5.3 (b)). For beam segments of B-C and D-E, it was found that shear deformation can be ignored during bending motion and Euler beam theory can be used. If bending in the shorter beam becomes dominant, as will be seen in the next section, Euler beam theory cannot be used anymore since dominant shear deformation take place during the bending of the shorter beams.

5.2.3 Verification of the analytic modeling along circumferential directions

To verify the proposed analytic modeling, the wave dispersion curve analytically calculated by the proposed mass-spring system is compared with that calculated by numerical method. In analysis, the proposed hyperbolic elastic metamaterials having a of

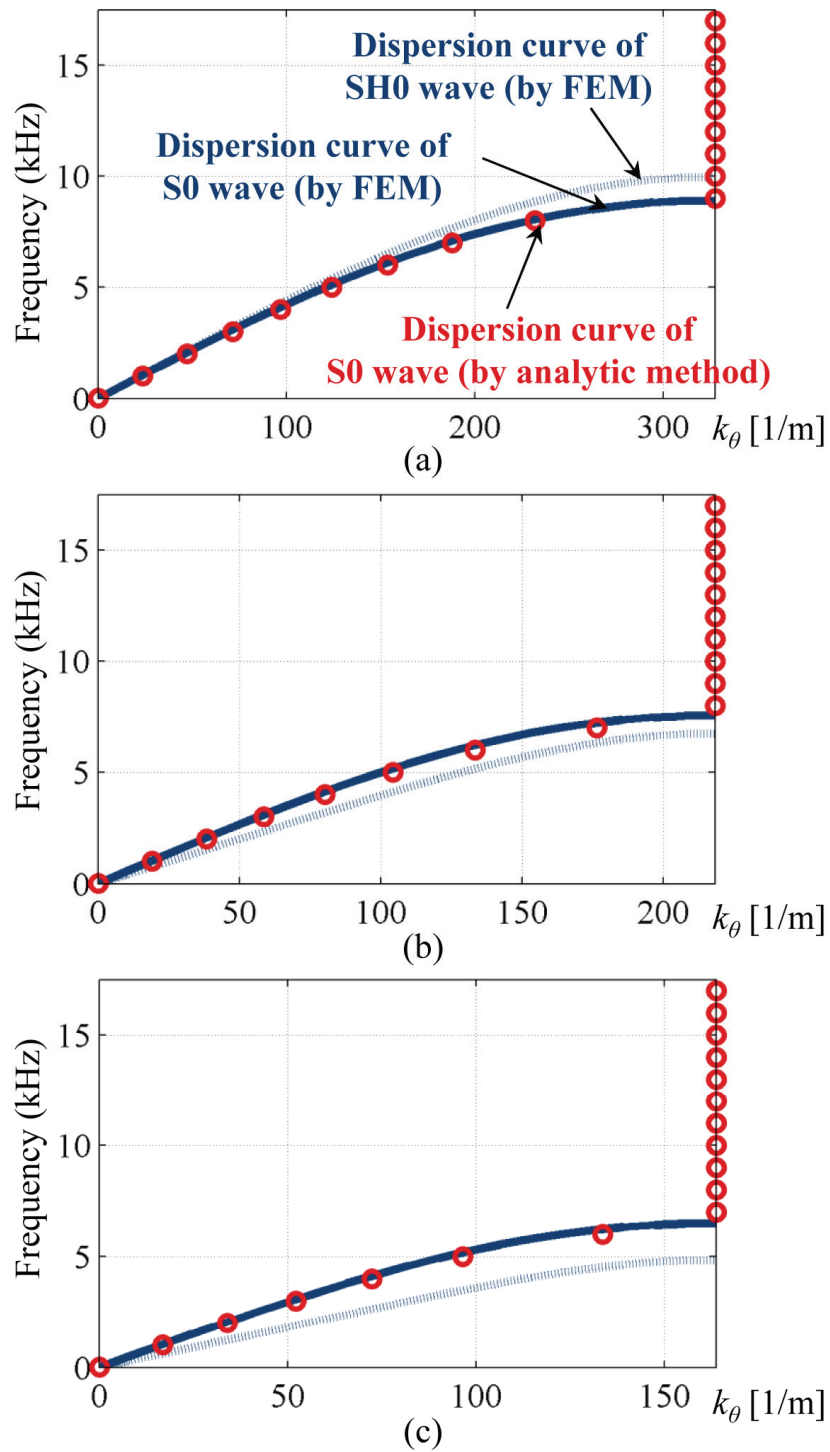


Fig. 5.4 Comparison of circumferential dispersion curves computed from the developed analytical model and the finite element model for metamaterials with $a =$ (a) 9.6 mm, (b) 14.4 mm and (c) 19.2 mm.

9.6 mm, 14.4 mm and 19.2 mm are considered. The comparison results are shown in fig. 5.4. In fig. 5.4, good agreements can be observed between the results obtained by the proposed analytic modeling and those by numerical simulations. From the comparison, the proposed analytic modeling can be verified.

It should be noted that only lower branch is considered here. Since motion of two springs become different at higher branches, the proposed analytic modeling is not appropriate for calculating higher branches. It was found that for higher branches, Segment S_1 should be significantly thick to provide proper boundary condition on Segment S_2 to use the proposed analytic modeling for higher branches. Furthermore, to predict branches higher than second branches, new mass-spring model which consists of more than three masses and springs should be newly proposed. However, considering that the operating frequency range of the proposed hyperlens is very low, only lowest branch in wave dispersion curve is considered in this work.

5.3 Analytic modeling along radial directions

5.3.1 Analytic calculation of the dispersion relation of mass-spring model along radial directions

Fig. 5.5 (a) shows the mass-spring system along radial direction. Note that spring s_1 and s_2 don't affect the motion along radial direction. In this case, the mass-spring system can be viewed as 1 dimensional system, and the free-body diagram of the n th mass can

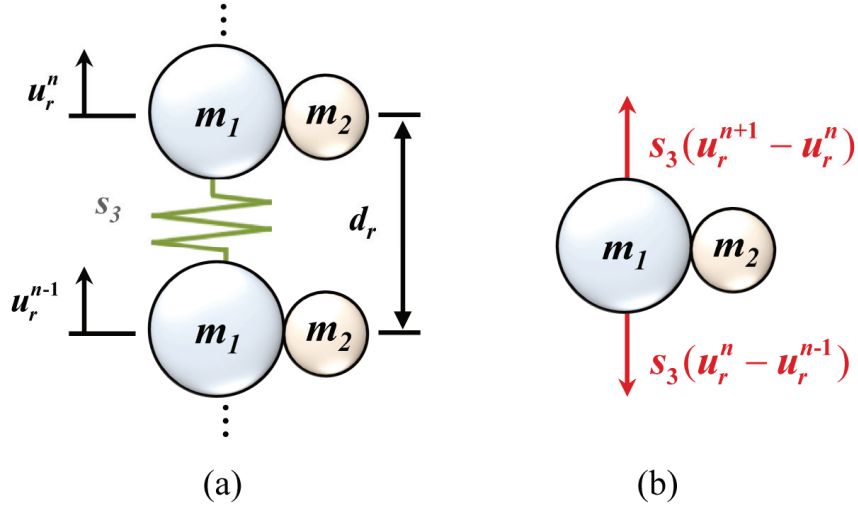


Fig. 5.5 (a) Equivalent mass-spring model for radial direction, (b) corresponding free-body diagram

be plotted as fig. 5.5 (b). The wave motion for this case is already calculated in chapter 3, but it is worth to briefly revisit the analytic procedure. The equation of the motion can be written as

$$(m_1 + m_2)\ddot{u}_r^n = s_3(u_r^{n+1} - u_r^n) - s_3(u_r^n - u_r^{n-1}). \quad (5.22)$$

Assuming periodic wave solution $u_r^n = U_r \exp[i(\omega t - k_r r)]$, u_r^{n+1} and u_r^{n-1} can be expressed as $u_r^{n+1} = \exp(-ik_r d_r)u_r^n$ and $u_r^{n-1} = \exp(ik_r d_r)u_r^n$. Substituting the assumption to equation (5.22), the following equation can be derived.

$$-(m_1 + m_2)\omega^2 = s_3(\exp(-ik_r d_r) - 1) - s_3(1 - \exp(ik_r d_r)). \quad (5.23)$$

Since $2 \cos x = \exp(-ix) + \exp(ix)$, following dispersion relation is derived.

$$\omega^2 = \frac{2(1 - \cos(k_r d_r))}{(m_1 + m_2)} s_3 \quad (5.24)$$

For low frequencies, almost below 20 kHz, the equation shown in equation (5.24) is enough to calculate wave dispersion curve with high accuracy. However, at the frequencies above 20 kHz, the proposed mass-spring modeling cannot well describe the wave dispersion characteristics. The problem occurred in the frequency above 20 kHz is that there exist certain resonance frequency that Segment S_2 acts as a dynamic damper and absorbs all wave energy which propagate to radial direction. Since Segment S_2 not only has longitudinal spring s_2 but also has shear spring, Segment S_2 has a shear-resonant frequency which affect radial wave propagation in Segment S_1 .

To additionally consider this effect, the shear spring of the Segment S_2 is added in the mass-spring model in fig. 5.5 (a), as shown in fig. 5.6 (a). Here, two masses m_3 and m_4 are re-defined later. From the free body diagram shown in fig. 5.6 (b), the equation of motion for each mass element can be written as

$$m_3 \ddot{u}_r^{n,j} = s_3(u_r^{n+1,j} - u_r^{n,j}) - s_3(u_r^{n,j} - u_r^{n-1,j}) + s_4(v_r^{n,j} - u_r^{n,j}) - s_4(u_r^{n,j+1} - v_r^{n,j}) \quad (5.25a)$$

$$m_4 \ddot{v}_r^{n,j} = s_4(u_r^{n,j+1} - v_r^{n,j}) - s_4(v_r^{n,j} - u_r^{n,j}). \quad (5.25b)$$

Assuming periodic wave solution as $u_r^{n,j} = U_r \exp[i(\omega t - k_r r)]$ and $v_r^{n,j} = V_r \exp[i(\omega t - k_r r)]$, it can be seen that $u_r^{n,j} = u_r^{n,j-1} = u_r^{n,j+1}$ and $v_r^{n,j} = v_r^{n,j-1} = v_r^{n,j+1}$.

Substituting the periodic wave assumptions to equation (5.25) yields

$$-\omega^2 m_3 u_r^{n,j} = s_3(\exp(-ik_r d_r) - 2 + \exp(ik_r d_r))u_r^{n,j} + 2s_4(v_r^{n,j} - u_r^{n,j}) \quad (5.26a)$$

$$-\omega^2 m_4 v_r^{n,j} = 2s_4(u_r^{n,j} - v_r^{n,j}). \quad (5.26b)$$

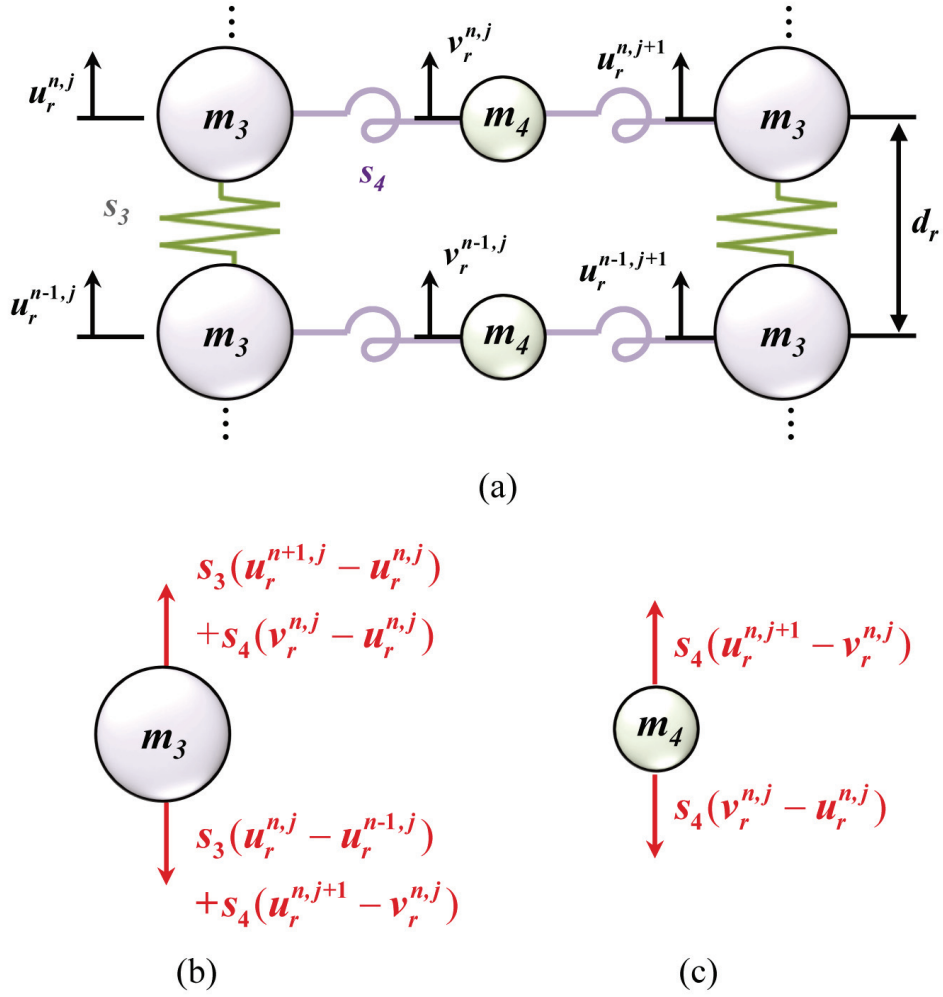


Fig. 5.6 (a) Equivalent mass-spring model for radial direction with additional shear spring s_4 , and corresponding free-body diagrams of (b) m_3 and (c) m_4

Equation (5.26a) and (5.26b) can be re-written in matrix form as

$$\hat{\mathbf{A}} \begin{bmatrix} u_r^n \\ v_r^n \end{bmatrix} = 0, \quad \hat{\mathbf{A}} = \begin{bmatrix} m_3 \omega^2 + (\exp(-ik_r d_r) + \exp(ik_r d_r) - 2)s_3 - 2s_4 & 2s_4 \\ 2s_4 & m_4 \omega^2 - 2s_4 \end{bmatrix}. \quad (5.27)$$

To calculate wave dispersion relation from equation (5.27), $\det(\hat{\mathbf{A}}) = 0$ should be calculated which can be written as

$$m_3 m_4 \omega^4 + [(\exp(-ik_r d_r) + \exp(ik_r d_r) - 2)m_4 s_3 - 2(m_3 + m_4)s_4] \omega^2 - 2(\exp(-ik_r d_r) + \exp(ik_r d_r) - 2)s_3 s_4 = 0 \quad (5.28)$$

Using $2 \cos x = \exp(-ix) + \exp(ix)$, equation (5.28) can be simplified as following.

$$m_3 m_4 \omega^4 + 2[(\cos(k_r d_r) - 1)m_4 s_3 - (m_3 + m_4)s_4] \omega^2 - 4(\cos(k_r d_r) - 1)s_3 s_4 = 0. \quad (5.29)$$

Re-arranging equation (5.29) with respect to k_r results in wave dispersion equation along radial direction as

$$k_r = \cos^{-1} \left[\frac{m_3 m_4 \omega^4 + 2s_4(m_3 + m_4)\omega^2}{4s_3 s_4 - 2s_3 m_4 \omega^2} + 1 \right] / d_r. \quad (5.30)$$

It should be noted that the dispersion calculation in equation (5.30) is extremely similar with that in internal resonance structures, as in Ref. [76]. To explain the point, let's consider mass-spring system having internal resonances, as shown in fig. 5.7. For the internal resonance system, the equation of motion for each mass can be written as

$$m'_3 \ddot{u}^n = s'_3 (u^{n+1} - 2u^n + u^{n-1}) + s'_4 (v^n - u^n) \quad (5.31a)$$

$$m'_4 \ddot{v}^n = s'_4 (u^n - v^n). \quad (5.31b)$$

Assuming periodic wave solutions, equations (5.31) become as

$$-\omega^2 m'_3 u^n = s'_3 (\exp(-ikd') - 2 + \exp(ikd')) u^n + s'_4 (v^n - u^n) \quad (5.32a)$$

$$-\omega^2 m'_4 v^n = s'_4 (u^n - v^n). \quad (5.32b)$$

Equation (5.32) is exactly same form as equation (5.26) if we set $2s_4 = s'_4$. The only difference between mass-spring models shown in fig. 5.7 (a) and fig. 5.6 (a) is that fig. 5.7 (a) can be applied to electromagnetic and acoustic waves while fig. 5.6 (a) can only be used for elastic waves, due to the existence of shear spring. Nevertheless, related

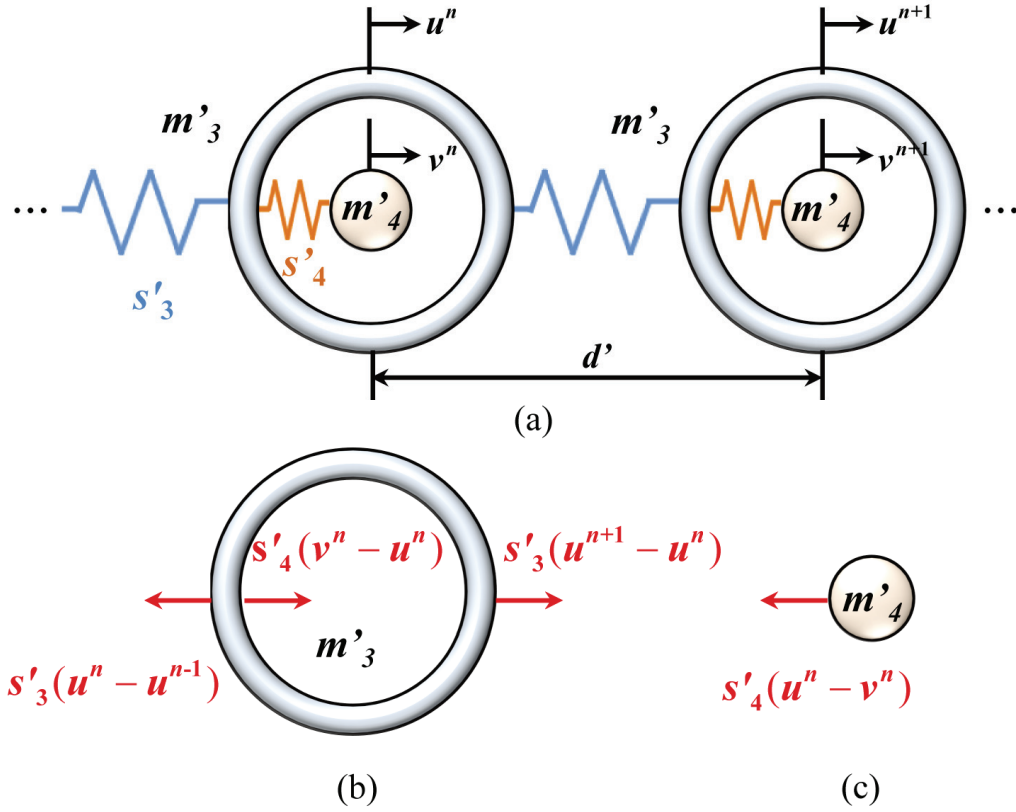


Fig. 5.7 (a) Equivalent mass-spring model for general internal resonant structures, and corresponding free-body diagrams of (b) m'_3 and (c) m'_4

physics of the mass-spring model in fig. 5.6 (a) are very similar to those in the internal resonance structures, if wave only propagates through radial direction. For wave propagation along various directions, equation (5.26) cannot be derived from equation (5.25) since $u_r^{n,j} = u_r^{n,j-1} = u_r^{n,j+1}$ and $v_r^{n,j} = v_r^{n,j-1} = v_r^{n,j+1}$ are not valid.

As shear spring is considered for the mass-spring system along radial direction, it can also be considered for mass-spring system along circumferential direction. However, the equivalent shear spring for Segment S_1 is relatively stiff, and does not highly affect the

overall wave characteristics along circumferential direction for the frequency ranges considered in this work. Thus, only the shear spring for Segment S_2 which affects the wave propagation along only radial direction is considered in this work.

5.3.2 Calculation of the equivalent mass/spring coefficients along radial directions

First, let's focus on derivation of equivalent spring coefficient s_3 . Considering wave motion along radial direction, the Segment S_1 can be viewed as a bar structure under compression as in figs. 5.8 (a). The major difference between calculating s_1 is that the boundary condition of the beam in this case is different from the previous one; it can be written as

$$\sigma_{zz} = \sigma_{xx} = 0 \quad (5.33)$$

The structure satisfying boundary condition of equation (5.33) is simply 1-dimensional bar structure, whose stress-strain relation can be written as simply

$$Ee_{yy} = \sigma_{yy} . \quad (5.34)$$

Therefore, the equivalent spring coefficient s_3 can be easily calculated as

$$s_3 = \frac{El_{S_1} t_{S_1}}{h_{S_1}} , \quad (5.35)$$

which is same as equivalent spring coefficient in 1-dimensional bar structure [55].

Now, to calculate shear spring coefficient s_4 of the Segment S_2 , the structure shown in

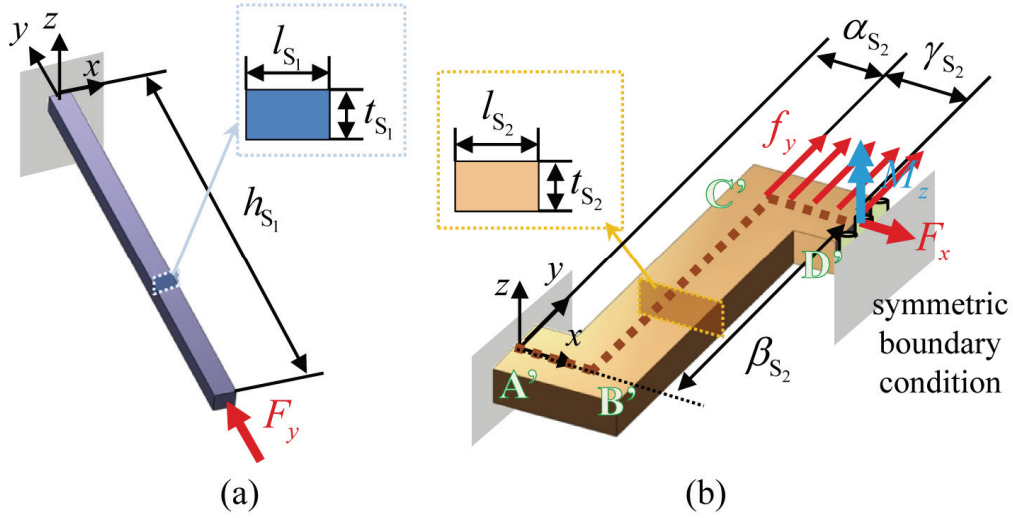


Fig. 5.8 Mechanical models for stiffness analysis of (a) Segment S_1 and (b) Segment S_2

fig. 5.8 (b) is considered. In fig. 5.8 (b), only the half of the Segment S_2 is considered with symmetric boundary condition at point D' . To calculate s_4 , external force F_y is uniformly-distributed along beam segment $C' - D'$, i.e., uniformly-distributed y -directional force $f_y = F_y / \gamma_{S_2}$ is applied along beam segment $C' - D'$. It should be emphasized that in calculating shear spring coefficient s_4 , the bending is dominantly occurred for the beam segments $A' - B'$ and $C' - D'$ in fig. 5.8. Since the bending of shorter beam segments $A' - B'$ and $C' - D'$ accompany significant shear deformations, Timoshenko beam theory [79] should be used in calculating s_4 . Assuming Timoshenko beams for all beam segments, elastic energy stored in each beam segments are

$$U_{A'B'} = \int_0^{\alpha_{S_2}} \left[\frac{[f_y(\gamma_{S_2}^2 / 2 + \gamma_{S_2} x) + M_z - F_x \beta_{S_2}]^2}{2EI_{S_2}} + \frac{(f_y \gamma_{S_2})^2}{2GA_{S_2} \kappa} \right] dx \quad (5.36a)$$

$$U_{B'C'} = \int_0^{\beta_{s_2}} \left[\frac{[f_y(\gamma_{s_2}^2 / 2) + M_z - F_x x]^2}{2EI_{s_2}} + \frac{F_x^2}{2GA_{s_2} \kappa} \right] dy \quad (5.36b)$$

$$U_{C'D'} = \int_0^{\gamma_{s_2}} \left[\frac{[f_y(x^2 / 2) + M_z]^2}{2EI_{s_2}} + \frac{(f_y x)^2}{2GA_{s_2} \kappa} \right] dx \quad (5.36c)$$

where G and κ denote shear modulus and shear correction factor, and $A_{s_2} = l_{s_2} t_{s_2}$ is cross-section area of each beam segments. In this study, $\kappa = 5/6$ is used as in general Timoshenko beam having rectangular cross-section.

From elastic energy shown in equation (5.36), applying same procedure [78] as previous approach for s_2 provides following equations for δ_x , δ_y and θ_z at point D',

$$\begin{aligned} \delta_x &= \frac{\partial U_{tot}}{\partial F_x} \\ &= \left[\left(\frac{\beta_{s_2}^3}{3} + \beta_{s_2}^2 \alpha_{s_2} \right) F_x + \left[-\frac{(\gamma_{s_2} + \alpha_{s_2}) \alpha_{s_2} \beta_{s_2}}{2} - \frac{\gamma_{s_2} \beta_{s_2}^2}{4} \right] \gamma_{s_2} f_y \right. \\ &\quad \left. + \left(-\alpha_{s_2} \beta_{s_2} - \frac{\beta_{s_2}^2}{2} \right) M_z \right] / EI_{s_2} + \frac{F_x \beta_{s_2}}{GA_{s_2} \kappa} \end{aligned} \quad (5.37a)$$

$$\begin{aligned} \delta_y &= \frac{\partial U_{tot}}{\partial F_y} = \frac{1}{\gamma_{s_2}} \frac{\partial U_{tot}}{\partial f_y} \\ &= \left[\left[-\frac{(\gamma_{s_2} + \alpha_{s_2}) \alpha_{s_2} \beta_{s_2}}{2} - \frac{\gamma_{s_2} \beta_{s_2}^2}{4} \right] F_x \right. \\ &\quad \left. + \left[\frac{(2\alpha_{s_2} + 3\gamma_{s_2}) \alpha_{s_2}^2}{6} + \frac{(\alpha_{s_2} + \beta_{s_2}) \gamma_{s_2}^2}{4} + \frac{\gamma_{s_2}^3}{20} \right] \gamma_{s_2} f_y \right. \\ &\quad \left. + \left[\frac{\alpha_{s_2}^2}{2} + \frac{(\alpha_{s_2} + \beta_{s_2}) \gamma_{s_2}}{2} + \frac{\gamma_{s_2}^2}{6} \right] M_z \right] / EI_{s_2} + \frac{\gamma_{s_2} f_y}{GA_{s_2} \kappa} \left(\alpha_{s_2} + \frac{\gamma_{s_2}}{3} \right) \end{aligned} \quad (5.37b)$$

$$\begin{aligned}
\theta_z &= \frac{\partial U_{tot}}{\partial M_z} \\
&= \left[(-\alpha_{S_2} \beta_{S_2} - \frac{\beta_{S_2}^2}{2}) F_x + \left[\frac{\alpha_{S_2}^2}{2} + \frac{(\alpha_{S_2} + \beta_{S_2}) \gamma_{S_2}}{2} + \frac{\gamma_{S_2}^2}{6} \right] \gamma_{S_2} f_y \right. \\
&\quad \left. + (\alpha_{S_2} + \beta_{S_2} + \gamma_{S_2}) M_z \right] / EI_{S_2}
\end{aligned} \tag{5.37c}$$

Subsequently, Castigliano theorem is used along with the boundary conditions at point

D' such that $\delta_x = 0$ and $\theta_z = 0$. The resulting condition can be written as

$$\begin{aligned}
\left(\frac{\beta_{S_2}^3}{3} + \beta_{S_2}^2 \alpha_{S_2} + \frac{EI_{S_2}}{GA_{S_2} \kappa} \beta_{S_2} \right) \frac{F_x}{f_y} + \left(-\alpha_{S_2} \beta_{S_2} - \frac{\beta_{S_2}^2}{2} \right) \frac{M_z}{f_y} \\
= \frac{(\gamma_{S_2} + \alpha_{S_2}) \alpha_{S_2} \beta_{S_2} \gamma_{S_2}}{2} + \frac{\gamma_{S_2}^2 \beta_{S_2}^2}{4}
\end{aligned} \tag{5.38a}$$

$$\begin{aligned}
\left(-\alpha_{S_2} \beta_{S_2} - \frac{\beta_{S_2}^2}{2} \right) \frac{F_x}{f_y} + (\alpha_{S_2} + \beta_{S_2} + \gamma_{S_2}) \frac{M_z}{f_y} \\
= -\frac{\alpha_{S_2}^2 \gamma_{S_2}}{2} - \frac{(\alpha_{S_2} + \beta_{S_2}) \gamma_{S_2}^3}{2} - \frac{\gamma_{S_2}^3}{6}
\end{aligned} \tag{5.38b}$$

As a result, the equivalent spring coefficient s_4 can be analytically calculated as

$$\begin{aligned}
\frac{1}{s_4} &= \frac{\delta_y}{F_y} = \frac{1}{\gamma_{S_2}} \frac{\delta_y}{f_y} \\
&= \left[\frac{(2\alpha_{S_2} + 3\gamma_{S_2}) \alpha_{S_2}^2}{6} + \frac{(\alpha_{S_2} + \beta_{S_2}) \gamma_{S_2}^2}{4} + \frac{\gamma_{S_2}^3}{20} \right. \\
&\quad \left. + \left[-\frac{(\gamma_{S_2} + \alpha_{S_2}) \alpha_{S_2} \beta_{S_2}}{2\gamma_{S_2}} - \frac{\beta_{S_2}^2}{4} \right] \frac{F_x}{f_y} + \left[\frac{\alpha_{S_2}^2}{2\gamma_{S_2}} + \frac{\alpha_{S_2} + \beta_{S_2}}{2} + \frac{\gamma_{S_2}}{6} \right] \frac{M_z}{f_y} \right] / EI_{S_2} \\
&\quad + \frac{1}{GA_{S_2} \kappa} \left(\alpha_{S_2} + \frac{\gamma_{S_2}}{3} \right)
\end{aligned} \tag{5.39}$$

where F_x / f_y and M_z / f_y can be evaluated by solving equations (5.38) as following;

$$\begin{aligned}
& \begin{bmatrix} \frac{\beta_{s_2}^3}{3} + \beta_{s_2}^2 \alpha_{s_2} + \frac{EI_{s_2}}{GA_{s_2} \kappa} \beta_{s_2} & -\alpha_{s_2} \beta_{s_2} - \frac{\beta_{s_2}^2}{2} \\ -\alpha_{s_2} \beta_{s_2} - \frac{\beta_{s_2}^2}{2} & \alpha_{s_2} + \beta_{s_2} + \gamma_{s_2} \end{bmatrix} \begin{bmatrix} \frac{F_x}{f_y} \\ \frac{M_z}{f_y} \end{bmatrix} \\
& = \begin{bmatrix} \frac{(\gamma_{s_2} + \alpha_{s_2}) \alpha_{s_2} \beta_{s_2} \gamma_{s_2} + \frac{\gamma_{s_2}^2 \beta_{s_2}^2}{4}}{2} \\ -\frac{\alpha_{s_2}^2 \gamma_{s_2}}{2} - \frac{(\alpha_{s_2} + \beta_{s_2}) \gamma_{s_2}^3}{2} - \frac{\gamma_{s_2}^3}{6} \end{bmatrix}. \quad (5.40)
\end{aligned}$$

Although Timoshenko beam modeling well calculate the equivalent spring coefficient s_4 , its accuracy may be worse as the width of the unit cell a becomes shorter. Especially, for $a = 9.6$ mm (which corresponds to the minimum width that used in the proposed hyperlens), length of the beam segments A'-B' and C'-D' are shorter than the thickness l_{s_2} and Timoshenko beam modeling may no more valid. For the case, pure shear modeling (in which only shear terms in equation (5.36) are considered) can be used for better accuracy. However, Timoshenko beam modeling is shown to provided sufficiently accurate results for the proposed hyperlens in this work.

In calculating the equivalent mass coefficients of m_3 and m_4 , deformed shape should be considered. At the resonance frequency, beam segment A'-B' are dominantly deformed while deformation in other beam segments is relatively small. Thus, in the viewpoint of resonance, beam segment A'-B' can be treated as spring element and others can be treated as mass element. In other word, the mass of beam segment A'-B' only slightly affects resonance frequency. Thus, only the mass of beam segments B'-C'

and C'-D' is considered in the equivalent mass coefficient m_4 which is related to the resonance frequency. Accordingly, the total mass of Segment S_1 and beam segment A'-B' is set to be m_3 .

5.3.3 Verification of the analytic modeling along radial directions

From the equivalent spring and mass coefficients, wave dispersion curve along radial direction can be analytically calculated. As in the previous section, verification of the proposed analytic approach is made by comparing the wave dispersion curve from analytic and numerical methods. Same as the previous comparison, the proposed hyperbolic elastic metamaterials having a of 9.6 mm, 14.4 mm and 19.2 mm are considered. For analytic method, both equation (5.24) which does not consider shear spring and equation (5.30) which considers shear spring are applied. The comparison results are shown in fig. 5.9. As can be seen from fig. 5.9, both equations provide accurate results for low frequency ranges. For the high frequency ranges, however, the analytic model without shear spring cannot describe well the wave dispersion curve while the analytic model with shear spring still exhibit high accuracy. Thus, the proposed analytic modeling with shear springs shown in equation (5.30) can be verified. In addition, the use of equation (5.24) at low frequency ranges can be justified from fig. 5.9.

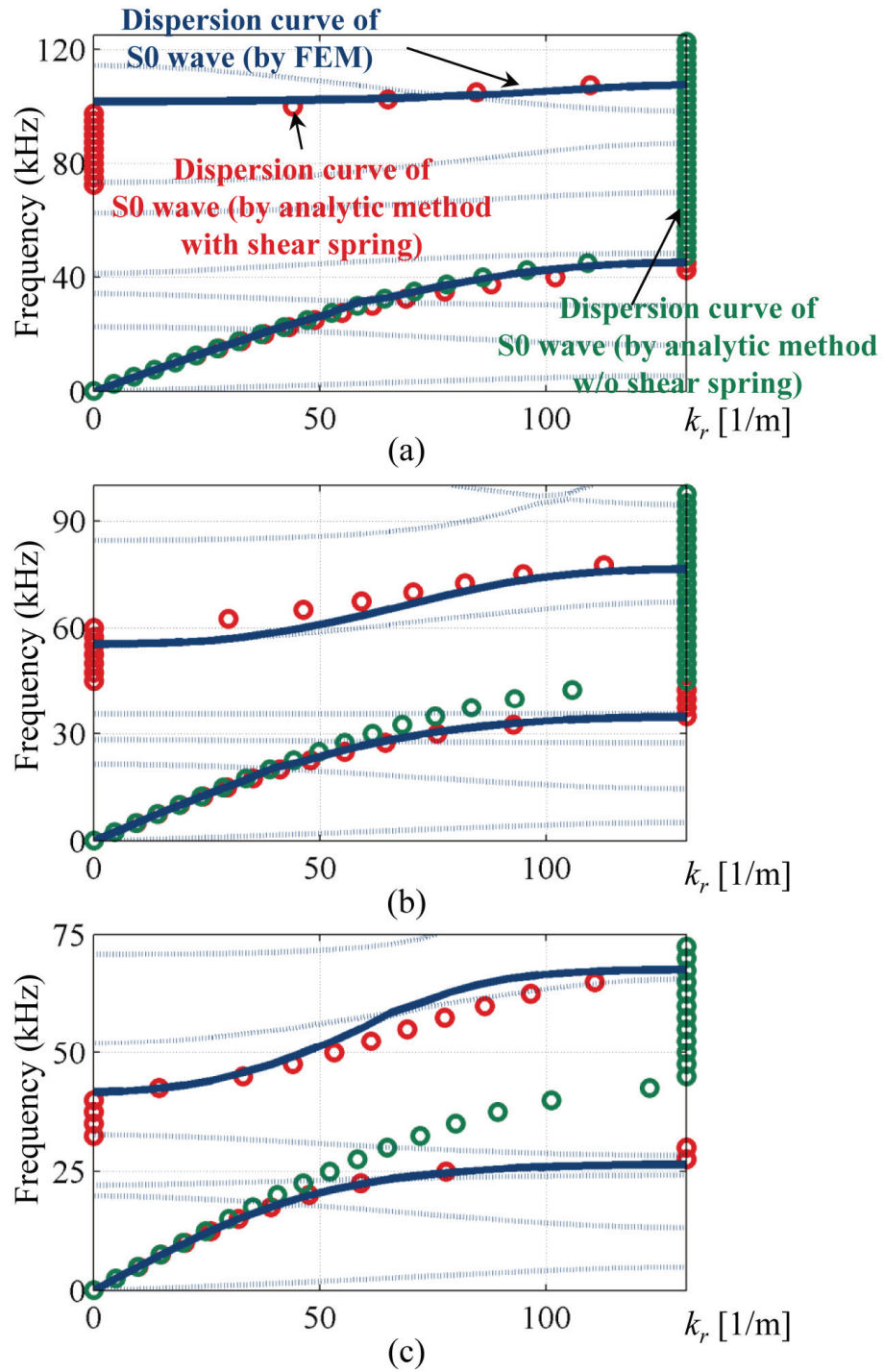


Fig. 5.9 Comparison of radial dispersion curves computed from the developed analytical model and the finite element model for metamaterials with $a =$ (a) 9.6 mm, (b) 14.4 mm and (c) 19.2 mm.

5.4 Design improvement by the proposed analytic method

From the established analytic modeling, the role of each design parameters can be explicitly studied. Before showing how the proposed analytic modeling can be used in designing the proposed elastic hyperlens, a frequency range Δf in which waves can propagate through radially but can't through circumferentially in the designed elastic metamaterial is considered as the performance measure. If hyperlens consists of metamaterials having high Δf , wide operating frequency of the hyperlens can be expected. From the analytic modeling shown previously, followings can be considered to increase Δf of the hyperbolic elastic metamaterial;

- Reducing equivalent spring coefficients s_2 , or
- Increasing resonance frequency of the internal segment (Segment S_2).

To achieve the first method, the bending stiffness of beam segments B-C and D-E in fig. 5.3 (b) should be lowered. Focusing on the second method, increasing stiffness of beam segments A-B and E-F (corresponding to increase of s_4) and reducing total mass of beam segments B-C, C-D and E-F (corresponding to decrease of m_4) are preferred.

There are infinite ways in achieving the two methods, and one of the possible design candidates is illustrated in fig. 5.10. In the new elastic metamaterial design, thicknesses of beam segments A-B and E-F are doubled to increase the spring coefficient s_4 . On the other hand, thicknesses of beam segments B-C, C-D and D-E are halved to decrease s_2 and m_4 . To check whether the new elastic metamaterial shows improved Δf or not,

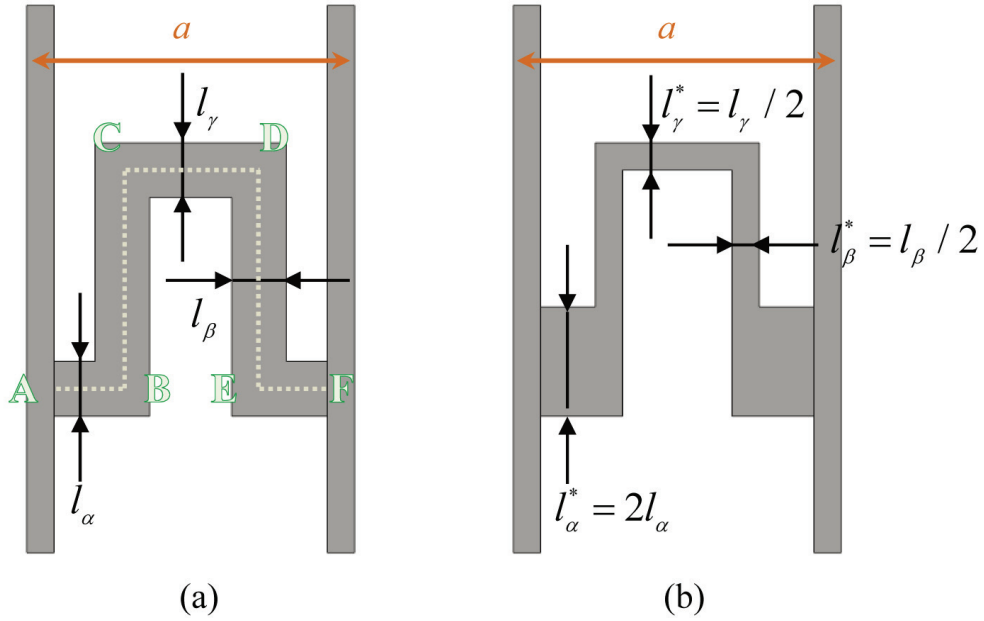


Fig. 5.10 (a) Original hyperbolic elastic metamaterial proposed in the previous chapter, (b) newly designed hyperbolic elastic metamaterial

wave dispersion curves are calculated for the metamaterials in fig. 5.10 (a) and (b) for a of 9.6 mm, 14.4 mm and 19.2 mm.

Fig. 5.11 shows the calculated dispersion curves. For comparison, normalized wavevector of $k_{norm} = k / (d\pi)$ is used while $d = a$ for waves along circumferential direction and $d = 0.024$ for waves along radial direction. From fig. 5.11, it can be seen that the newly designed elastic hyperbolic metamaterial has higher Δf . The resonance gaps along radial direction are increase while the frequencies where band-gap starts are decreased along circumferential direction. The improvements are 47.2 %, 71.6 % and 88.1 % for a of 9.6 mm, 14.4 mm and 19.2 mm, respectively. Note that changing the thickness of each beam segment is shown to be the most effective way in the hyperbolic

metamaterial design. The results shown in fig. 5.11 clearly shows that design improvement can be made based on the proposed analytic modeling.

As shown in this section, the performance of the proposed hyperlens can be further increased by tailoring the geometry of the unit cell. Thus, the structural optimization, such as topology optimization, can be effectively applied for the hyperlens design. The topology optimization of the proposed elastic hyperbolic metamaterial can be considered as a future work in which the proposed analytic mass-spring modeling is expected to provide proper object functions for the optimization and to support the physical explanation of the performance improvement in optimized results.

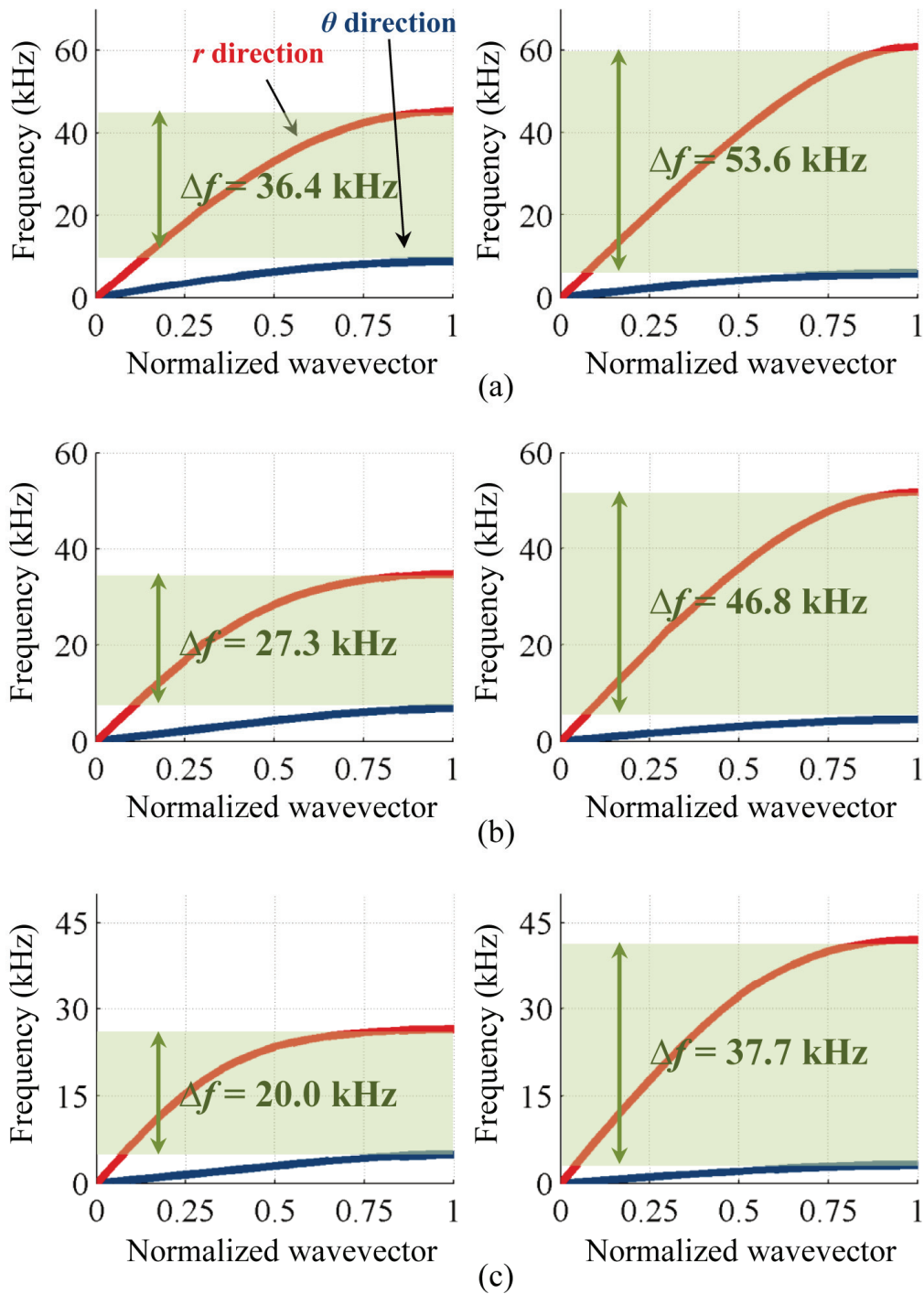


Fig. 5.11 Comparison of dispersion curves between original metamaterial (left) and new metamaterial (right) for $w =$ (a) 9.6 mm, (b) 14.4 mm and (c) 19.2 mm.

Chapter 6.

Conclusion

In this work, new elastic hyperlens which exhibit theoretically unlimited resolution was realized. Previously proposed elastic hyperlens achieved sub-wavelength resolution but it had certain resolution limit and thus showed degraded performance. Motivated by this, the major object of this work was developing new elastic hyperlens which can overcome the limitation of the previously proposed elastic hyperlens. In this investigation, not only design and simulation of the new hyperlens but also experimental and analytic approaches were made. The summary of detailed investigations is presented in the following.

First, physical origin of diffraction limit and operating principle of hyperlens were reviewed. It was explained that diffraction limit takes place since general material cannot carry waves having k_{θ} above certain limit. On the other hand, it was shown that hyperlens can break diffraction limit since waves which were unable to be carried in general material can be carried in the hyperlens. In addition, the interaction between higher order scattering modes and crack becomes very high in the hyperlens, which allow sub-wavelength resolution. The sub-wavelength resolution by hyperlens was shown to be achieved by either elliptic or hyperbolic EFC's, but hyperbolic EFC can show much high performance. Since the previously proposed elastic hyperlens had been based on elliptic EFC, it was shown that designing elastic metamaterial having hyperbolic EFC is key in

the present investigation.

To design new elastic metamaterial having hyperbolic EFC, the design requirements were figured out – 1. exhibiting hyperbolic EFC, 2. wide operating frequency range with low loss, 3. low scattering for imaging purpose, 4. various design variables. A new elastic metamaterial was designed in which corrugated structure is inserted between two beam segments. Also, new hyperlens was engineered based on the proposed elastic metamaterial. By finite element method, the proposed elastic hyperlens were proven to show hyperbolic EFC. In addition, the proposed hyperlens was shown to exhibit sub-wavelength resolution at far field with higher performance than previously proposed one by numerical simulation.

After design and numerical verification of the hyperlens were shown, realization and experimental approach of the proposed hyperlens were made. Here, elastic wave actuators which can realize wide line source of 150 mm with low frequency waves of 15 kHz were required. Since general elastic transducers could not satisfy the requirement, new magnetostrictive transducer, G-MPT, was developed. In addition, specially-shaped Gabor pulse was used to avoid data distortion by induction signal. During post-processing, it was shown that signal calibration by normalization is essential. As a result, sub-wavelength resolution by the proposed hyperlens was experimentally shown, which agreed well with the simulation results.

Finally, an analytic modeling was formulated via equivalent mass-spring system for the

proposed elastic metamaterial. The equivalent mass-spring system consists of three masses and springs were mainly considered. By equation of motion in each mass and periodic wave assumption, wave dispersion equations of the mass-spring system were derived. Each equivalent mass and spring coefficient was calculated analytically. Especially, equivalent spring coefficients of the corrugated structure inside the proposed hyperbolic elastic metamaterial were calculated via energy method. By comparing wave dispersion curve obtained by proposed analytic method and finite element simulation, the proposed analytic approach was verified. Based on the proposed analytic equation, design guidelines for improving performance of the proposed elastic hyperlens were given.

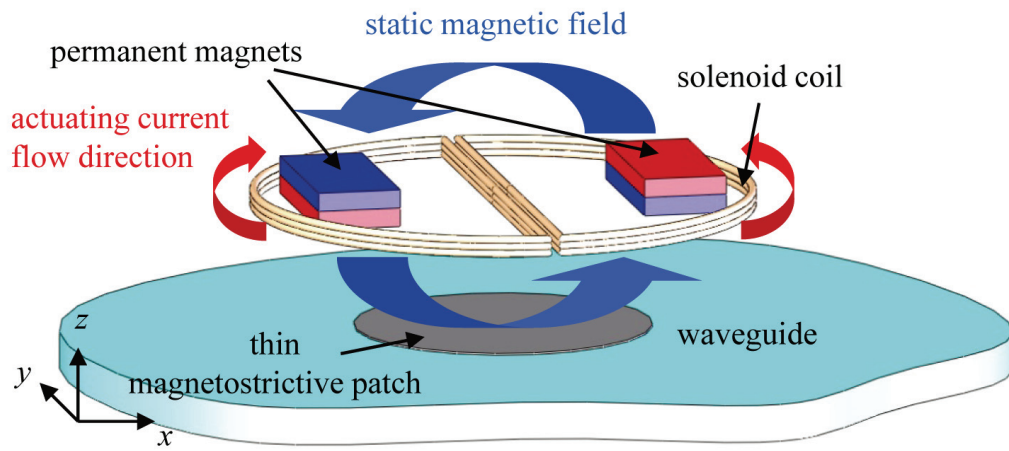
Appendix A.

Finite element analysis of radiation characteristics of guided waves generated by magnetostrictive patch-type transducers

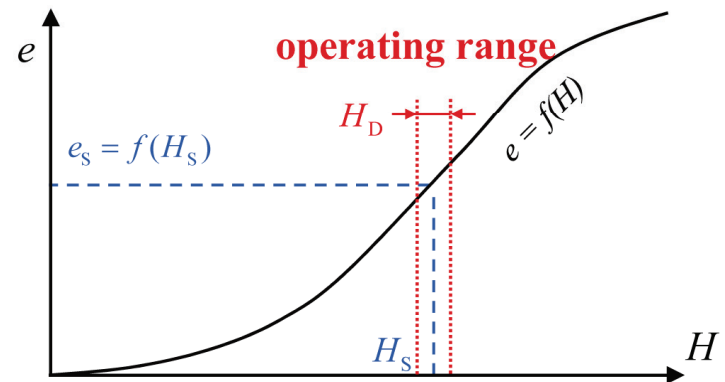
A.1. Appendix overview

Magnetostriction [72, 73] indicates coupling effect between mechanical elastic fields and magnetic fields, which can be observed in ferromagnetic materials. If magnetic field is applied to magnetostrictive material, mechanical deformation of the material occurs (i.e. Joule effect). On the other hand, if stress is induced in magnetostrictive material, its magnetization changes (i.e. Villari effect). Due to magnetostriction, energy transformation between mechanical energy and magnetic energy can take place. Therefore, magnetostriction has been widely used in many engineering applications such as sensor and actuators [80-82], system control devices [83, 84] and energy harvesting devices [85, 86].

Among various applications of magnetostriction, let's focus on recently developed elastic wave transducers based on thin magnetostrictive patches [66,67,87]. These transducers use thin magnetostrictive patches to generate and measure ultrasonic elastic waves. Fig. A1 (a) shows a schematic diagram of the magnetostrictive patch-type transducer (MPT) installed on an aluminum plate for guided elastic wave based ultrasonic non-destructive evaluation. As shown in fig. A1 (a), the transducer consists of a thin magnetostrictive



(a)



(b)

Fig. A.1 (a) Schematic illustration of an MPT installed on a plate waveguide with circular magnetostrictive patch, (b) typical magnetostriction curve

patch bonded onto a plate waveguide and a magnetic circuit consisting of two permanent magnets and a figure-eight-shaped coil. Before presenting detailed finite element analysis for sensing and actuation with MPT's, the underlying working principle will be briefly explained first.

When actuation current flows through the coil, dynamic magnetic field (H_D) is

generated around the coil. As the dynamic magnetic field is applied to the patch, a time-varying elastic deformation will be developed in the patch due to the magnetostrictive effect. Regarding that the patch is bonded to a plate waveguide, the patch-bonded region of the waveguide will also dynamically deform accordingly. As a result, the dynamic deformation produces elastic wave propagating in the waveguide. In the overall process, static magnetic field H_s is induced to magnetostrictive patch to facilitate magnetostriction in the patch. This can be observed in fig. A1 (b) where typical magnetostrictive behavior is depicted as a strain-magnetic field curve. Since static magnetic field H_s by a pair of permanent magnets offsets the operating range, the linear range in the magnetostrictive curve is used during MPT's operation.

Some studies [68-70,88] have been performed to understand wave generation and measurement mechanism by MPT and to improve its performance (i. e. sensitivity, wave-mode decoupling or optimization). However, since these studies were mainly based on experimental approach, detailed wave generation and measurement mechanisms are not still fully investigated. To study the detailed wave generation mechanism, analytic first-order theory in Ref. [68,69] was developed to explain some basic wave phenomena, but it was hard to be applied for general MPT's. For the investigation based on numerical simulation, Kim and Jung [89] proposed finite element analysis for acoustic wave characteristics of acoustic magnetostrictive transducer and Perez-Aparicio and Sosa [90] developed three dimensional, fully coupled finite element formulation dedicated for magnetostrictive materials. Recently, Ribichini *et al.* [91,92] investigated wave generation by the magnetostrictive nickel under unidirectional bias magnetic field by

numerical simulation. However, there have been some limitations in applying the previously investigated methods to MPT's because magnetic fields induced on a thin magnetostrictive patch are generally not constant. Motivated by this, the main goal of this appendix is to develop a numerical simulation method to predict wave generation and measurement mechanics of general MPT's. Here, the finite element method and time-harmonic elastic wave analysis is applied for the simulation.

In the present investigation, two main difficulties in the numerical simulation of the wave generation and measurement mechanism by MPT's are mainly focused. The first difficulty is that a previously proposed numerical analysis model [89-92] is not applicable in simulating the magnetostrictive patch used in MPT's. In MPT's, the generation and measurement of elastic waves are significantly influenced by how the static and dynamic magnetic fields are applied to the patch. However, the previously proposed analysis model does not take it into account. Therefore, this issue should be properly overcome to accurately simulate the wave generation and measurement mechanism of MPT's. In this issue, any magnetic circuit having non-uniformly distributed or arbitrarily oriented magnetic fields must be handled. The other difficulty is that the generated guided waves by MPT's usually have multi-modes [93] which should be distinguished properly. In experiments, multi-modes can be easily distinguished by time-of-flight. For numerical simulation, transient analysis can be performed to distinguish each mode by time-of-flight as in experiment, but it requires huge computation time. Thus, a special scheme is required to distinguish the influence of each mode in time-harmonic numerical analysis.

This appendix is organized as follows. In chapter A.2, a time-harmonic finite element formulation is made based on the linearized magnetostrictive coupling equation. In chapter A.3, the proposed finite element analysis is verified and several discussions related to the finite element analysis results is investigated. The conclusions of the appendix are drawn in chapter A.4.

A.2. Finite element formulation for general MPT's

A.2.1 Linearized magnetostrictive modeling for general MPT's

In this section, a linearized magnetostrictive modeling for general MPT's is formulated. Especially, linearized modeling is properly formulated to deal with arbitrarily induced static magnetic fields for problems involving MPT's.

As shown in fig. A.1 (b), magnetostriction is a nonlinear phenomenon in which the relation between magnetic field H and strain S is plotted as a nonlinear curve. However, only considering small magnetic field variation due to induced dynamic magnetic field \mathbf{H}_D in the magnetostrictive material under the large static magnetic field \mathbf{H}_S as in MPT, the behavior around \mathbf{H}_S can be written in linear form as [94]:

$$\mathbf{e} = \mathbf{S}\boldsymbol{\sigma} + \mathbf{d}^T \mathbf{H}_D \quad (\text{A.1a})$$

$$\mathbf{B}_D = \mathbf{d}\boldsymbol{\sigma} + \boldsymbol{\mu}\mathbf{H}_D . \quad (\text{A.1b})$$

Here, \mathbf{e} denotes strain fields defined as $\mathbf{e} = [e_{xx} \ e_{yy} \ e_{zz} \ e_{yz} \ e_{xz} \ e_{xy}]^T$ and \mathbf{H}_D denotes dynamic magnetic fields defined as $\mathbf{H}_D = [H_{D_x} \ H_{D_y} \ H_{D_z}]^T$. $\boldsymbol{\sigma}$ and \mathbf{B}_D are stress and dynamic magnetic flux density, respectively, which are defined in the same manner as strain and dynamic magnetic field. Also, \mathbf{S} is used as compliance, $\boldsymbol{\mu}$ permeability and \mathbf{d} piezomagnetic coupling coefficient.

As previously explained, only local magneto-mechanical coupling around \mathbf{H}_S is considered in equation (A.1). Thus, the coupling coefficient \mathbf{d} in equation (A.1) should be a function of the static magnetic field \mathbf{H}_S . This means that the coupling coefficient \mathbf{d} has a directional property since the coefficient is defined based on the static magnetic field \mathbf{H}_S which has a specific direction. As a matter of convenience, local coordinates (x', y', z') of which the direction of x' axis is same as the direction of the static magnetic field \mathbf{H}_S is introduced, as in fig. A.2. For nickel, which is mainly considered as a magnetostrictive patch in this work, the coupling coefficient \mathbf{d} is defined in the local coordinates (x', y', z') as [72]:

$$\mathbf{d} = \begin{bmatrix} d_{1'1'} & d_{1'2'} & d_{1'2'} & 0 & 0 & 0 \\ 0 & 0 & 0 & 0 & 0 & d_{3'5'} \\ 0 & 0 & 0 & 0 & d_{3'5'} & 0 \end{bmatrix} \quad (\text{A.2})$$

while the components in equation (A.2) are defined as [71]

$$d_{1'1'} = \left. \frac{\partial f(H)}{\partial H} \right|_{H_S} \quad (\text{A.3a})$$

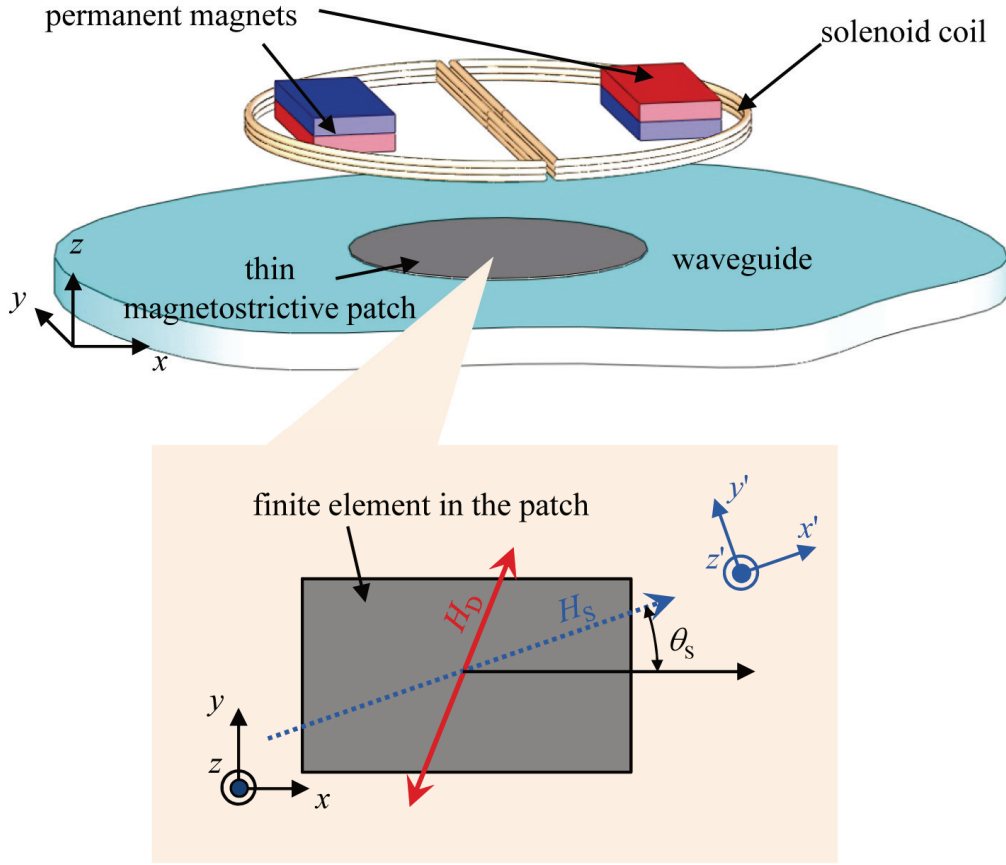


Fig. A.2 a finite element in the patch under simultaneous applications of the static magnetic field H_S and the dynamic magnetic field H_D

$$d_{1'2'} = -0.5d_{1'1'} \quad (\text{A.3b})$$

$$d_{3'5'} = 3 \frac{f(H_S)}{H_S} \quad (\text{A.3c})$$

In equation (A.3), $f(H)$ is a strain function with respect to the magnetic field H as $S = f(H)$, as shown in fig. A.1 (c). Also, H_S is the magnitude of the static magnetic field vector, $H_S = |\mathbf{H}_S|$.

Assuming that the static magnetic field in a magnetostrictive material is uniformly oriented, i.e. has same direction everywhere in the material, the local coordinate (x',y',z') defined in the patch would be same for everywhere. Under this assumption, the finite element analysis can be simplified by setting the local coordinate (x',y',z') same as the global coordinate (x,y,z) everywhere in the patch. For this case, the coupling coefficient \mathbf{d} can be easily defined from the magnitude of the static field in each element, as in equation (A.2) and (A.3). Unfortunately, the assumption cannot be used for MPT's since static magnetic field in a magnetostrictive patch has various directions in the patch, depending on the shape of the patch. In analyzing MPT's, the local coordinate (x',y',z') in which the coupling coefficient \mathbf{d} in equation (A.2) is defined should be different from one element to another. However, this is not preferred in finite element analysis in which all finite element formulations for every element are formulated in the same global coordinate (x,y,z) .

To make equation (A.2) more suited for finite element analysis, the coupling coefficient \mathbf{d} , which is defined in the local coordinate in equation (A.2), is re-defined in the global coordinate system by axis transformation. The axis transformation from the local coordinate (x',y',z') to the global coordinate (x,y,z) can be made by 3-dimensional tensor analyses. However, in this work, 2-dimensional assumption is utilized in the axis transformation to simplify the process. Since magnetostrictive patch in MPT's is usually very thin, the z component of the induced static magnetic field in the patch is usually negligible. This means that the static magnetic field in the patch can be regarded as a 2-

dimensional in-plane magnetic field lying in the x - y plane. Therefore, the z' axis in the local coordinate (x', y', z') can be set to be same as the z axis in the global coordinate (x, y, z) everywhere in the patch. Under this assumption, the 3-dimensional axis transformation is reduced to a 2-dimensional axis transformation from the local coordinate (x', y') to the global coordinate (x, y) . Resulting axis transformation from the local coordinate (x', y', z') to the global coordinate (x, y, z) yield following coupling coefficients \mathbf{d} defined in the global coordinate as:

$$\mathbf{d} = \begin{bmatrix} d_{11} & d_{12} & d_{13} & 0 & 0 & d_{16} \\ d_{21} & d_{22} & d_{23} & 0 & 0 & d_{26} \\ 0 & 0 & 0 & d_{34} & d_{35} & 0 \end{bmatrix} \quad (\text{A.4})$$

where

$$d_{11} = d_{1'1'} \cos^3 \theta_S + (d_{1'2'} + 2d_{3'5'}) \cos \theta_S \sin^2 \theta_S \quad (\text{A.5a})$$

$$d_{12} = d_{1'2'} \cos^3 \theta_S + (d_{1'1'} - 2d_{3'5'}) \cos \theta_S \sin^2 \theta_S \quad (\text{A.5b})$$

$$d_{21} = d_{1'2'} \sin^3 \theta_S + (d_{1'1'} - 2d_{3'5'}) \cos^2 \theta_S \sin \theta_S \quad (\text{A.5c})$$

$$d_{22} = d_{1'1'} \sin^3 \theta_S + (d_{1'2'} + 2d_{3'5'}) \cos^2 \theta_S \sin \theta_S \quad (\text{A.5d})$$

$$d_{13} = d_{1'2'} \cos \theta_S, \quad d_{23} = d_{1'2'} \sin \theta_S \quad (\text{A.5e, A. 5f})$$

$$d_{34} = d_{3'5'} \sin \theta_S, \quad d_{35} = d_{3'5'} \cos \theta_S \quad (\text{A.5g, A.5h})$$

$$d_{16} = (d_{1'1'} - d_{1'2'} - d_{3'5'}) \cos^2 \theta_S \sin \theta_S + d_{3'5'} \sin^3 \theta_S \quad (\text{A.5i})$$

$$d_{26} = (d_{1'1'} - d_{1'2'} - d_{3'5'}) \cos \theta_S \sin^2 \theta_S + d_{3'5'} \cos^3 \theta_S. \quad (\text{A.5j})$$

Here, the value θ_S is an angle which the static magnetic field and the x axis in the global coordinate (x, y, z) make for each element in the patch, as illustrated in fig. A.2.

Using the results shown in equation (A.4), any magnetostriction phenomena under arbitrarily induced static magnetic field can be analyzed, which is necessary in simulating general MPT's.

Before closing the section, it is worth to introduce the one-directional coupling assumption which can simplify the analysis. Strictly speaking, a fully-coupled magnetostrictive equation (both equation (A.1a) and (A.1b)) is required to analyze the magnetostriction in the patch. However, if material shows very small magnetostriction in which the coupling coefficient \mathbf{d} is comparably small, a one-directional coupling assumption can be adopted. For wave actuation case in MPT where external magnetic field generates strain changes, the one-directional coupled equation can be written as:

$$\mathbf{e} = \mathbf{S}\boldsymbol{\sigma} + \mathbf{e}_{\text{MS}} \quad (\text{A.6a})$$

$$\mathbf{B}_D = \boldsymbol{\mu}\mathbf{H}_D \quad (\text{A.6b})$$

where $\mathbf{e}_{\text{MS}} = \mathbf{d}^T \mathbf{H}_D$ is an additional strain due to the magnetostriction effect. This one-directional coupling equation significantly reduces the computational time. Since a ferromagnetic nickel mainly considered in this work has very small magnetostriction, the one-directional coupling equation in equation (A.6) can be used in this work. Note that the finite element analysis results based on the fully-coupled equation and the one-directional coupling equation were almost identical, which support the one-directional coupling assumption for this work.

A.2.2 Time-harmonic wave simulation for general MPT's

In this section, an analysis for elastic wave generation and propagation due to the magnetostrictive deformation of the patch will be formulated. In calculating the wave generation and propagation in the waveguide, a time-harmonic elastic analysis is substituted for the linearized magnetostrictive equation previously derived. Starting from elastic wave analysis, elastic equilibrium equation can be written in tensor form as:

$$\boldsymbol{\rho} \frac{\partial^2 \mathbf{u}}{\partial t^2} - \bar{\nabla} \boldsymbol{\sigma} = 0. \quad (\text{A.7})$$

while

$$\bar{\nabla} = \begin{bmatrix} \frac{\partial}{\partial x} & 0 & 0 & 0 & \frac{\partial}{\partial z} & \frac{\partial}{\partial y} \\ 0 & \frac{\partial}{\partial y} & 0 & \frac{\partial}{\partial z} & 0 & \frac{\partial}{\partial x} \\ 0 & 0 & \frac{\partial}{\partial x} & \frac{\partial}{\partial y} & \frac{\partial}{\partial z} & 0 \end{bmatrix} \quad (\text{A.8})$$

In equation (A.7), $\boldsymbol{\rho}$ is density matrix and \mathbf{u} is displacement vector. Substituting the one-directional magnetostrictive coupling equation in equation (A.6a), equation (A.7) can be re-written as:

$$\boldsymbol{\rho} \frac{\partial^2 \mathbf{u}}{\partial t^2} - \bar{\nabla} \cdot (\mathbf{S})^{-1} \mathbf{e} = -\bar{\nabla} \cdot (\mathbf{S})^{-1} \mathbf{e}_{\text{MS}} = -\bar{\nabla} \cdot (\mathbf{S})^{-1} \mathbf{d}^T \mathbf{H}_D. \quad (\text{A.9})$$

Equation (A.9) indicates that the strain induced by magnetostriction can be treated as external elastic force.

For time-harmonic analysis, the field variables \mathbf{u} and \mathbf{H}_D can be assumed to be a harmonic function with respect to the frequency ω , as $\mathbf{u} = \mathbf{u}_0 \exp(i\omega t)$ and

$\mathbf{H}_D = \mathbf{H}_0 \exp(i\omega t)$. Therefore, by substituting time-harmonic wave solution with equation (A.9), the following time-harmonic equation can be formulated:

$$\rho\omega^2 \mathbf{u}_0 + \nabla \cdot (\mathbf{S})^{-1} \nabla_s \mathbf{u}_0 = \nabla \cdot (\mathbf{S})^{-1} \mathbf{d}^T \mathbf{H}_0 \quad (\text{A.10})$$

where ∇_s is a strain-displacement matrix which is already defined in chapter 3. In equation (A.10), \mathbf{d} and \mathbf{H}_0 can be determined from preceding magnetic analyses for static and dynamic magnetic fields. As a result, the elastic wave generation and radiation can be solved by equation (A.10).

It should be noted that although the dynamic magnetic field induced by the actuation current flow in the coil is assumed to be harmonic, the dynamic equations are only considered for elastic fields. In other word, quasi-static magnetic field assumption is made and no electric field generated by time-varying magnetic field, or Faraday's Law, is considered in this work [68]. The justification of the quasi-static assumption can be made by considering that operating frequencies of MPT's are generally several kHz which is so low that any electromagnetic wave phenomena can be ignored. In this frequency range, the overall MPT system's scale is extremely smaller than the wavelength of electromagnetic wave. Therefore, although the dynamic magnetic field is applied to the patch, its distribution in the patch can be obtained by a quasi-magnetic analysis. On the other hand, for elastic waves the quasi-static assumption cannot be used since wavelength of elastic wave is comparable to the MPT system. This is why the time derivatives are only defined for elastic field variables, or displacement vector \mathbf{u} , in equation (A.10).

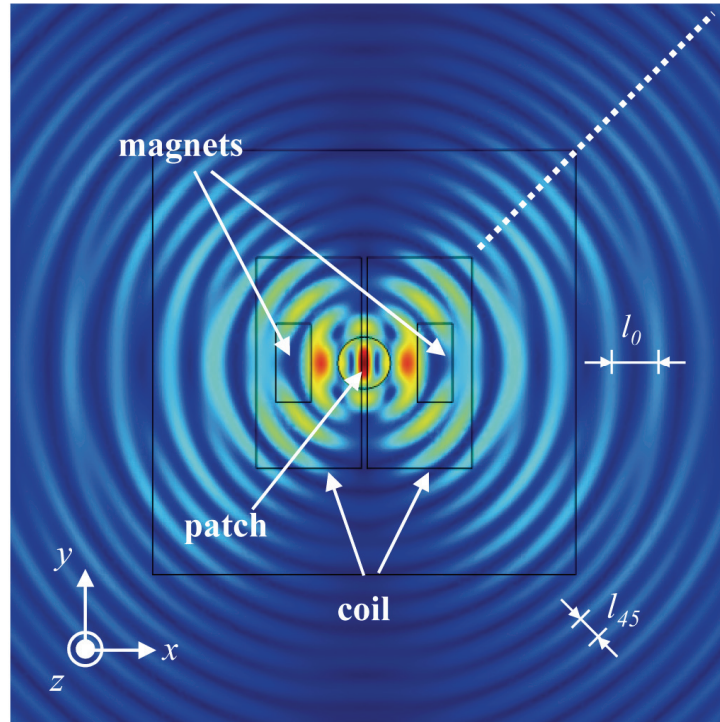


Fig. A.3 The total displacement field distribution in the waveguide obtained by the proposed finite element method

After the actuation and propagation of elastic guided waves from MPT's are calculated, a radiation pattern of the generated waves should be evaluated. As previously explained, since multiple modes of guided wave are actuated by MPT, a special scheme is required to distinguish the displacement field of each guided wave modes. In experiments in which a pulse-type actuating signal such as a modulated Gaussian pulse [68,69] is used, the signals corresponding to different elastic guided modes can be separately measured due to their speed difference [93]. However, in the time-harmonic analysis as in this work, wave speeds are not considered during simulation and the displacement fields for different elastic guided modes is mixed in the analyzed results. Fig. A.3 shows the total

displacement field $u_{\text{total}} = \sqrt{\text{real}^2(u) + \text{real}^2(v) + \text{real}^2(w)}$ distribution in the waveguide obtained by the proposed finite element method of which the operating frequency is 300 kHz. In fig. A.3, it can be seen that wavelengths measured along various direction have different values. For example, it can be observed in fig. A.3 that the peak-to-peak distance of the displacement fields along x direction, denoted as l_0 in fig. A.3, is different from that along the 45° tilted direction, denoted as l_{45} in fig. A.3. This indicates that propagating wave's mode along x direction is different from that along 45° tilted direction. From this investigation, it is clearly shown that displacement fields of multiple guided wave modes are mixed in the waveguide. This is why a special scheme which can distinguish the displacement fields of each guided wave modes should be introduced.

In the previous researches [68-70], normal and shear strains at the measurement point in the waveguides are used to distinguish each mode. However, this is not preferred in the finite element analysis where the strain fields might have low accuracy since they are interpolated by lower order of element's shape function than the displacement fields [63]. Therefore, in this work, the displacement fields based extraction is carried out. At a given measurement point illustrated in fig. A.4, two dominant modes, S0 and SH0 modes [93], are distinguished by extracting the radial and circumferential displacement fields which can be written as:

$$\text{For S0 mode : } u_\xi, \text{ For SH0 mode : } u_\eta. \quad (\text{A.11})$$

In equation (A.11), only S0 and SH0 modes are considered since the dominantly

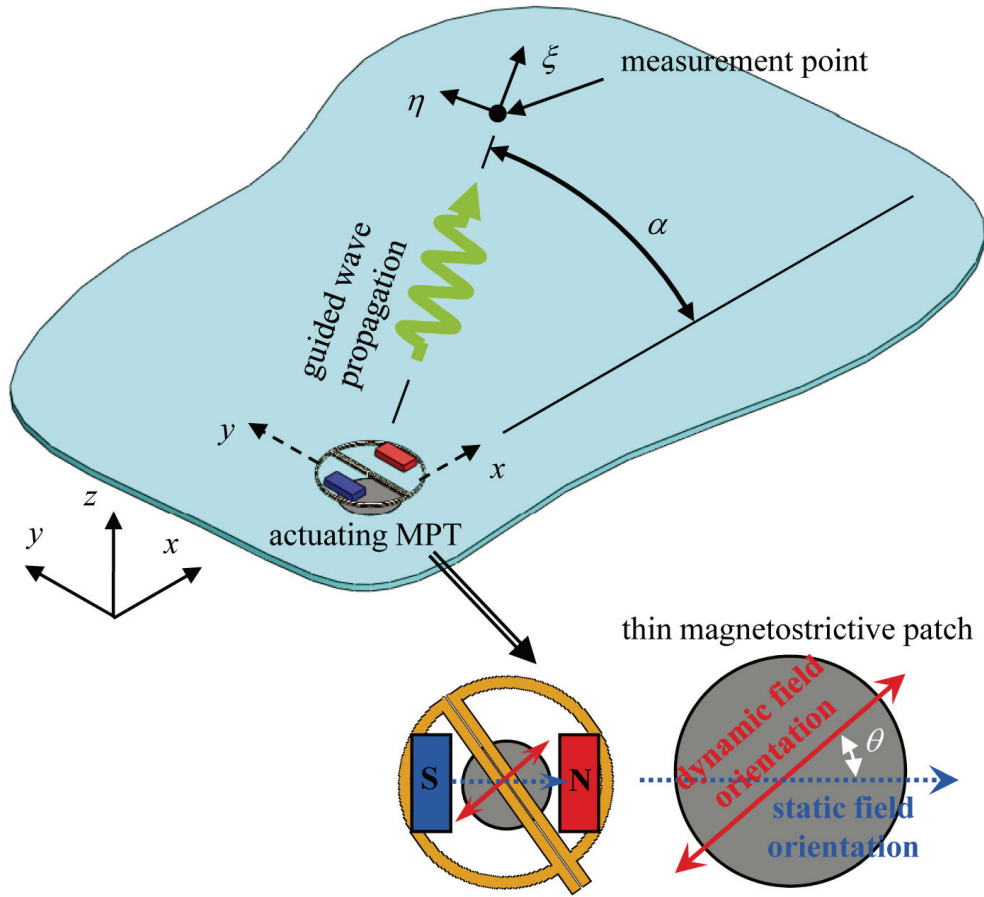


Fig. A.4 Schematic diagram of the waveguide mode extraction scheme at the measurement point

generated modes are S0 and SH0 modes in MPT's [68,69]. In addition, an operating frequency of MPT's is usually lower than the cut-off frequency of the higher modes such as S1 and SH1 modes [93], and only the lowest modes can be considered. Nevertheless, other guided wave modes such as A0 mode can also be extracted by using the out-of-plane displacement fields.

To verify the proposed wave mode extraction scheme in equation (A.11), a spatial

Fourier transformation is performed for the extracted displacement fields. In particular, the finite element results plotted in fig. A.3 is considered. First, the real value of u_ξ and u_η are measured along the dotted white line in fig. A.3. Then, a spatial Fourier transformation is performed for the measured displacement fields. Fig. A.5 shows the results of the spatial Fourier transformation for the displacement fields u_ξ and u_η along the line. From fig. A.5, it can be seen that there exists only one peak for each case. For example, the peak for measured displacement field u_ξ is located at the wavevector value of 355.3, which is same as the wavevector value of the S0 mode for 300 kHz in a 3 mm thick aluminum plate. In addition, the peak for measured displacement field u_η is located by the wavevector value of 621.9, which is the same as the wavevector value of the SH0 mode for 300 kHz in a 3 mm thick aluminum plate. Thus, results in fig. A.5

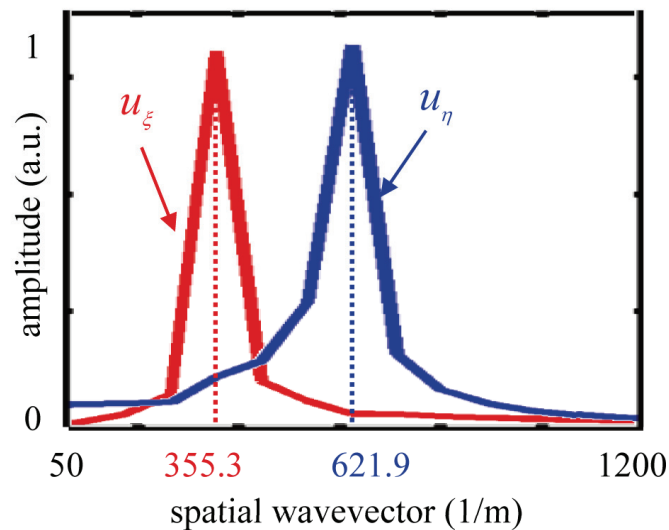


Fig. A.5 The results of spatial Fourier transformation for two displacement fields measured along the dotted line in fig. A.3

indicates that only one wave mode exists for each of the calculated displacement data. From this investigation, it is verified that the displacement field for each elastic guided wave modes can be well distinguished by using equation (A.11).

Finally, the radiation pattern for each elastic guided wave modes can be calculated as followings. In experiments, the radiation pattern is measured by the peak-to-peak value V_{p-p} . Thus, the amplitude of the extracted displacement field in equation (A.11) is used as a measured value in the finite element analysis. In other words, the absolute value of the complex displacement field value, such as $\sqrt{real(u_{\xi})^2 + imag(u_{\xi})^2}$ for S0 mode wave, is used as a measured value. This value is measured for every measurement point which is arranged circularly around the actuating MPT. Finally, the measured displacement values at every measurement point are normalized by their maximum value, which gives the MPT's radiation pattern.

A.2.3 Overall finite element analysis procedure

The overall process of the proposed finite element analysis is shown in fig. A.6. As in fig. A.6, the overall analysis process can be divided into three steps. In the first step, magnetic finite element analyses are performed for the magnetic field induced by the permanent magnets and by the current flow in the coil. Here, the static magnetic fields due to the permanent magnets and dynamic magnetic field due to the coil are independently calculated by the separated magnetic finite element analysis. As explained

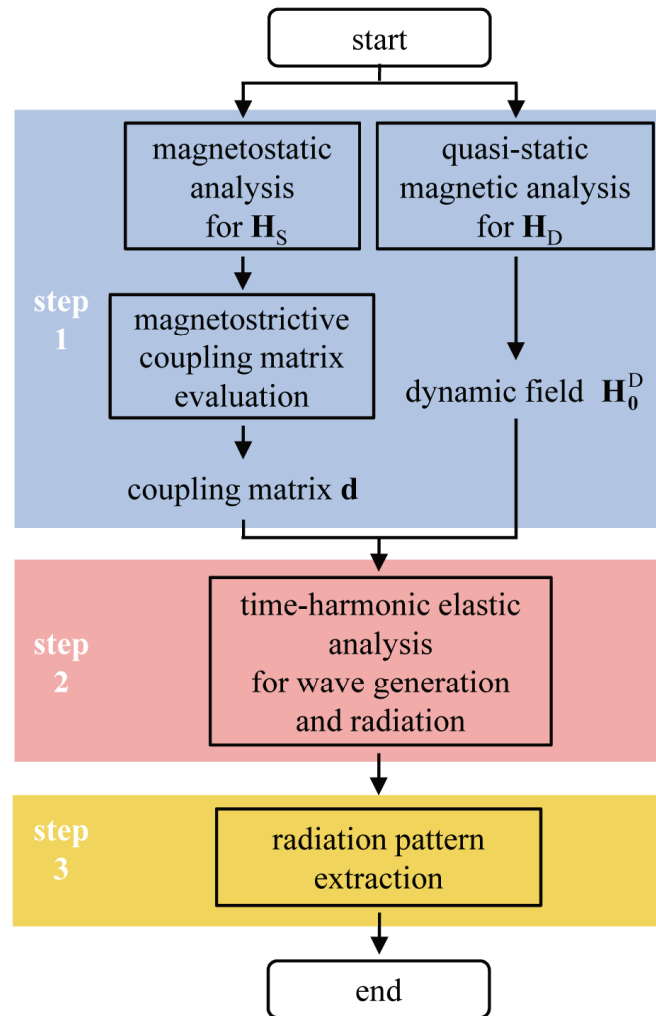


Fig. A.6 The proposed finite element analysis procedure for the MPT-waveguide system

earlier, although the magnetic field induced by the coils is dynamic, quasi-static magnetic finite element analysis is carried out. After the induced static magnetic field is calculated at all finite elements of the magnetostrictive patch, the coupling coefficients of each of the finite element in the magnetostrictive patch are determined by equations (A.4, A.5).

In the second step, time-harmonic elastic finite element analysis is performed for elastic

guided wave generation and propagation, as in equation (A.10). From the dynamic magnetic field and the coupling coefficients determined in the first step, the external harmonic force term in the right side of equation (A.10) can be evaluated. At the patch-waveguide interface, a perfect bonding condition is considered, i.e. the nodes at the patch-waveguide interface are shared by the finite elements of the patch and those of the waveguide. As a result, the elastic guided wave propagating in the elastic waveguide can be calculated by time-harmonic analysis.

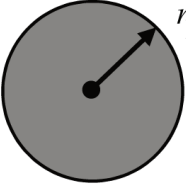
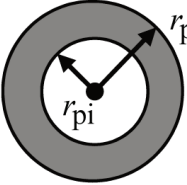
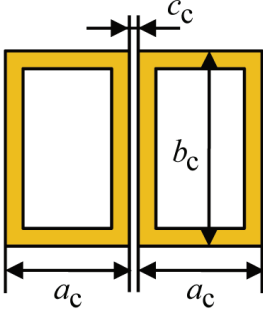
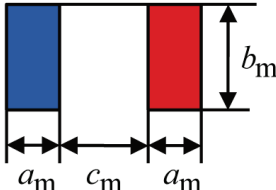
In the final step, radiation patterns for each of the modes are calculated from time-harmonic analysis result. From the time-harmonic analysis results calculated in the previous step, the displacement fields for each of the guided wave modes are extracted at each measurement points on the waveguide by using the equation (A.11). Finally, the measured values are normalized for their maximum value, resulting in the MPT's radiation pattern for desired guided wave mode.

A.3. Verification of the proposed analysis and numerical observations

A.3.1 Verification of the proposed finite element analysis

In this section, the developed finite element analysis will be applied to the real MPT-waveguide system and verified by comparing the results with experimentally measured radiation patterns. Two MPT's having different magnetostrictive patch are considered – one has a circular shape and the other has a ring shape. The detailed geometric data of the

patch and the magnetic circuits is shown in fig. A.7. To check the accuracy of the developed method, an experiment for both cases are conducted and compared with the developed finite element analysis results. The material properties used in the finite element analyses are summarized in below:

	CASE 1	CASE 2
patch	 $r_p = 5$ $t_p = 0.15$ thickness : t_p	 $r_{po} = 5$ $r_{pi} = 1.5$ $t_p = 0.15$ thickness : t_p
solenoid coil	 $a_c = 20, b_c = 40, c_c = 1$ 6 mm above the waveguide consist of line elements	
permanent magnet	 $a_m = 6.7, b_m = 15$ $c_m = 20, t_m = 3$ 8 mm above the waveguide thickness : t_m	
waveguide	thickness $t_w = 3$	

(unit : mm)

Fig. A.7 The geometric parameters of MPT's considered in CASE 1 and CASE 2

- **Magnetic circuit**

current in coil : 1 A

magnetization of the permanent magnet : 4×10^5 A/m

permeability of the coil and magnets : $4\pi \times 10^{-7}$ H/m (same as air)

- **Magnetostrictive patch made of nickel**

Young's Modulus of the nickel : 207×10^9 Pa

Poisson's ration of the nickel: 0.31

density of the nickel : 8880 kg/m^3

permeability of the nickel : 3.1416×10^{-4} H/m (relative permeability : 250)

- **Plate waveguide made of aluminum**

Young's Modulus of the aluminum: 70×10^9 Pa

Poisson's ration of the aluminum : 0.33

density of the aluminum : 2700 kg/m^3

permeability of the aluminum : $4\pi \times 10^{-7}$ H/m (same as air)

For the magnetostriction curve of nickel, the experimental data given in [72] is interpolated as:

$$e_{x'x'} = -6.9868 \times 10^{-5} \times \tanh^2(0.0005 \times H_{x'}). \quad (\text{A.12})$$

In equation (A.12), x' indicate the direction of the induced magnetic field, as in fig. A.2. Note that the hyperbolic form of magnetostriction curve is used in the nonlinear magnetostrictive modeling [95]. The major advantage of the hyperbolic tangent based

interpolation is that interpolation has a zero slope around the origin, which is physically admissible. On the other hand, the zero slope around the origin may not be observed if the polynomial functions are used in the interpolation. For the finite element simulation, COMSOL multiphysics is used [64].

In the previous experiments [68,69], the measurements were made at the points located 200 mm away from the actuating MPT. However, using the same measurement requires extremely large computational cost. This is because the size of the finite element should be small enough to correctly analyze the dynamic wave behavior. Thus, in the finite element analysis, measurements are made at 65 mm away from the actuating MPT. Although these measurement points are closer than those in the experiments, they are far enough for the far-field assumption [96] and the difference does not affect the radiation pattern.

CASE 1

As the first problem, three MPT's with $\theta = 0^\circ$, $\theta = 45^\circ$ and $\theta = 90^\circ$ are considered. Here, θ is an angle between the dominant static magnetic field direction and the dominant dynamic magnetic field direction, as illustrated in fig. A.4. As shown in the previous researches [68,69], MPT's radiation pattern changes as θ changes since the relative distribution of the static and dynamic magnetic field in the patch is different for the different θ .

Each of the three MPT's and waveguide is discretized by almost 390,000 finite elements.

Especially, the maximum distance between the neighboring nodes in the patch and the waveguide is set to be 1 mm, which is 17 times smaller than S0 mode's wavelength and 10 times smaller than SH0 mode's wavelength at the actuating frequency of 300 kHz. This insures sufficiently accurate analysis of the dynamic wave behavior in the patch and the waveguide. Note that more elements were also tried in simulation, but the solution improvement was marginal. At the each edge of the waveguide, perfectly matched layers (PML) [64] are placed to prevent any wave reflection at the boundary. Thus, only the waves which propagate in the radial direction from the actuating MPT are calculated in the proposed finite element analysis.

From the finite element results, normalized displacement for S0 and SH0 modes are measured by equation (A.11). Fig. A.8 shows the displacement plot of finite element analysis results for the wave generation of the MPT with $\theta = 0^\circ$. After the radiation pattern is calculated numerically, the resultant radiation pattern is compared with the experimental results. The comparison between the numerically and experimentally measured radiation patterns are plotted in fig. A.9 and A.10. In figs. A.9 and A. 10, good agreements can be observed between the two radiation patterns.

For the MPT with $\theta = 0^\circ$, both the static and dynamic magnetic fields have same dominant direction along x axis ($\alpha = 0^\circ$). Thus, the major longitudinal deformation of the patch occurs along x axis ($\alpha = 0^\circ$ and 180°), which generates S0 mode wave along $\alpha = 0^\circ, 90^\circ, 180^\circ$ and 270° inside the waveguide (fig. A.9 (a)). In addition, since

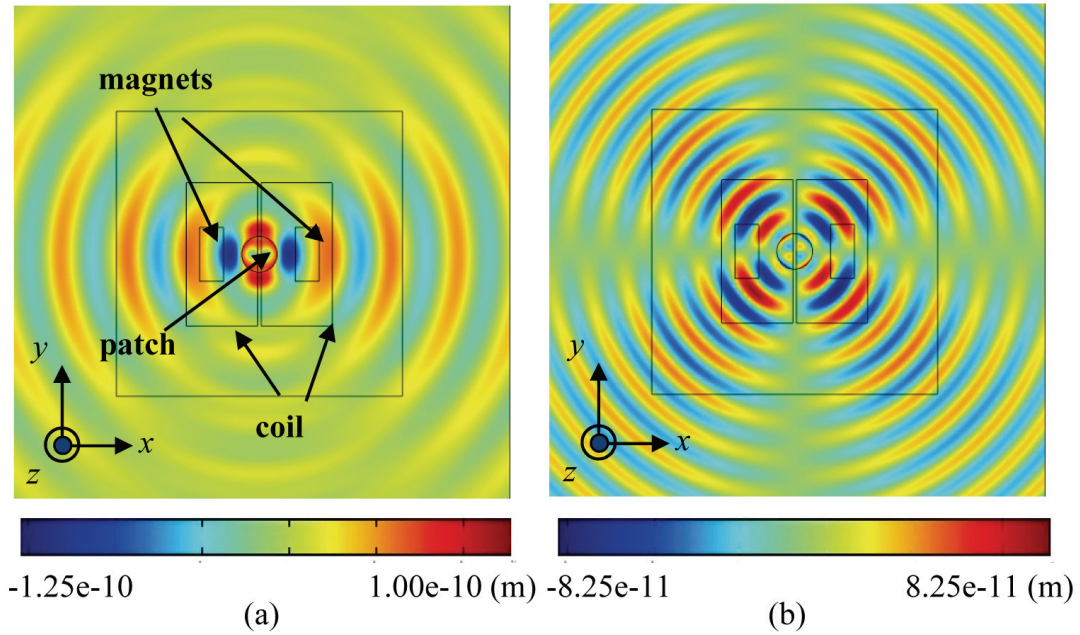
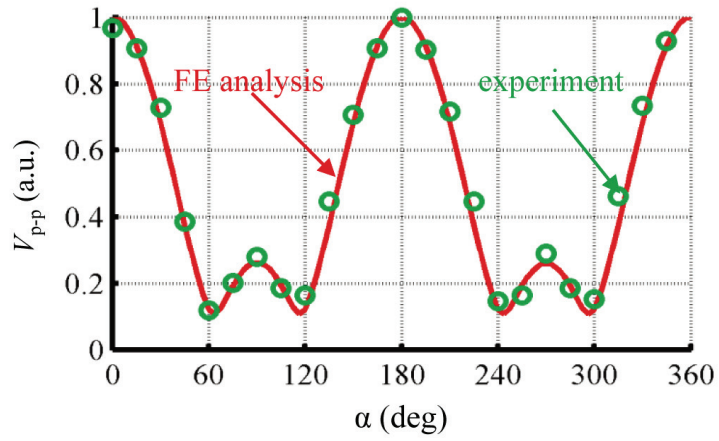


Fig. A.8 Plots of wave displacement fields of (a) S0 mode and (b) SH0 mode generated by the MPT of CASE 1 with $\theta = 0^\circ$

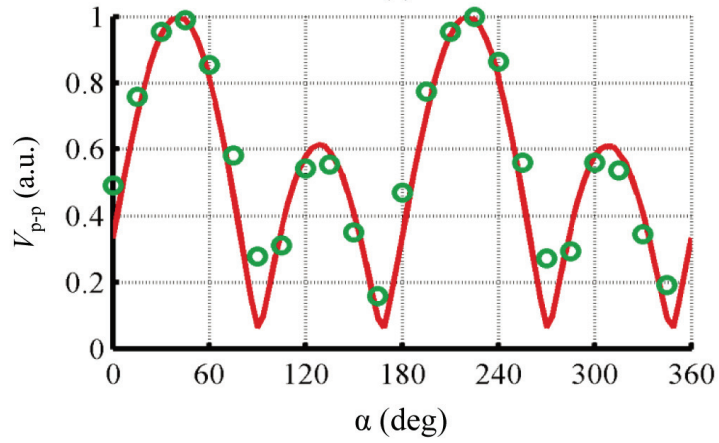
the longitudinal deformation along x axis can be seen as a shear deformation along 45° tilted direction, this contraction also generates SH0 mode wave along 45° tilted directions, i.e. $\alpha = 45^\circ, 135^\circ, 225^\circ$ and 315° , inside the waveguide (fig. A.10 (a)).

Likewise, For the MPT with $\theta = 90^\circ$, the dominant directions of the static and dynamic magnetic fields are normal to each other. The major deformation of the patch for this case is a shear deformation along x axis ($\alpha = 0^\circ$). This shear deformation provides SH0 mode wave along $\alpha = 0^\circ, 90^\circ, 180^\circ$ and 270° inside the waveguide (fig. A.10 (c)), and S0 mode wave along $\alpha = 45^\circ, 135^\circ, 225^\circ$ and 315° inside the waveguide (fig. A.9 (c)).

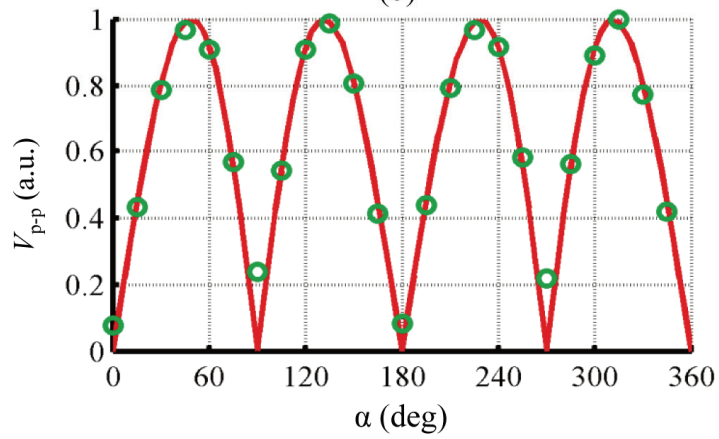
Since the MPT with $\theta = 45^\circ$ can be considered as the linear sum of the MPT's with



(a)

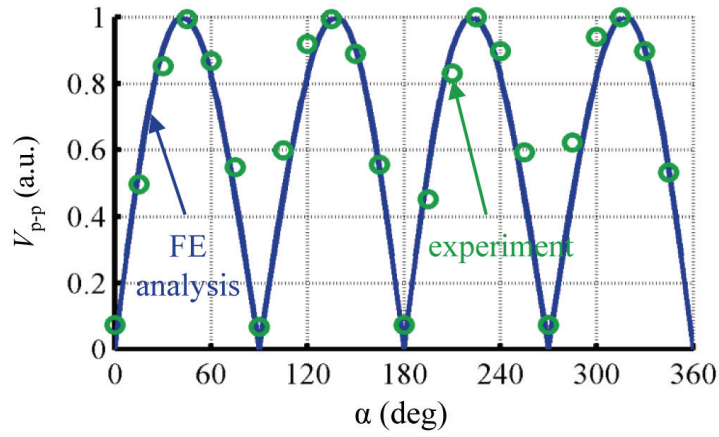


(b)

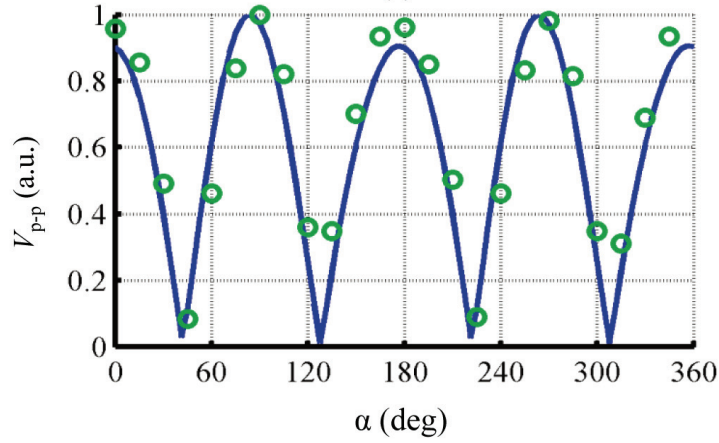


(c)

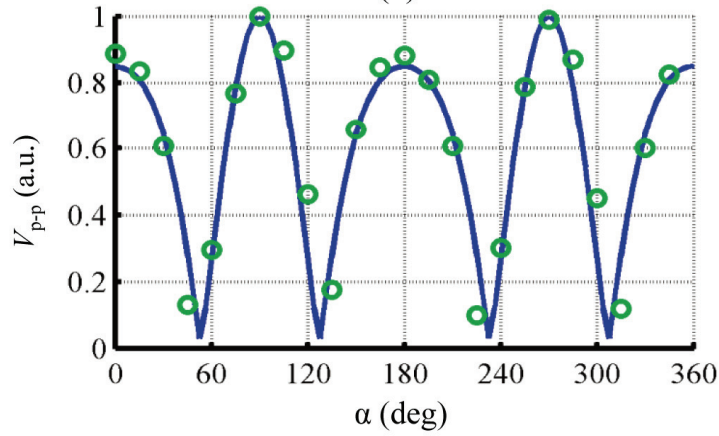
Fig. A.9 Comparison of the numerically and experimentally measured radiation patterns of the S0 mode for CASE 1 with (a) $\theta = 0^\circ$, (b) $\theta = 45^\circ$ and (c) $\theta = 90^\circ$



(a)



(b)



(c)

Fig. A.10 Comparison of the numerically and experimentally measured radiation patterns of the SH0 mode for CASE 1 with (a) $\theta = 0^\circ$, (b) $\theta = 45^\circ$ and (c) $\theta = 90^\circ$

$\theta = 0^\circ$ and $\theta = 90^\circ$, it can be seen from fig. A.9 (b) and A.10 (b) that its radiation pattern is almost same as the average of the radiation patterns of the MPT with $\theta = 0^\circ$ (fig. A.9 (a) and A.10 (a)) and $\theta = 90^\circ$ (fig A.9 (c) and A.10 (c)).

Before proceeding to the CASE 2, some interesting points should be noted. Considering the MPT with $\theta = 0^\circ$, it was explained that the major deformation of the patch is a longitudinal deformation along x axis ($\alpha = 0^\circ$ and 180°). Since no volume change occurs during magnetostriction, the longitudinal deformation of the magnetostrictive patch along y axis ($\alpha = 90^\circ$ and 270°) should be half of that along x axis, as in equation (A.3). Thus, it can be expected that the wave propagation along x axis is twice as large as that propagating along y axis. However, as shown in fig. A.9 (a) in which the S0 radiation pattern for $\theta = 0^\circ$ is plotted, the ratio of the normalized V_{p-p} along $\alpha = 0^\circ$ and $\alpha = 90^\circ$ is 0.3, not 0.5. The same phenomena can also be observed in fig. A.10 (c) in which the SH0 radiation pattern for $\theta = 90^\circ$ is plotted. In fig. A.10 (c), the normalized V_{p-p} along $\alpha = 0^\circ$ and $\alpha = 90^\circ$ is not same. This may seem strange since the major deformation of the patch is a shear deformation in which deformations along x and y axis are same. The major reason of these phenomena is the non-uniform magnetic field induction in the patch, which will be discussed in the later section.

CASE 2

In CASE 2, MPT using a ring patch instead of the circular patch used for CASE 1 is

considered. Here, the orientations of the permanent magnets and the coil are set to be same as those in the MPT considered in CASE 1 with $\theta = 0^\circ$. Fig. A.11 shows the finite element analysis results for the MPT with the ring patch with $\theta = 0^\circ$. To check the validation of the finite element analysis, an experiment for the MPT with the ring patch is carried out to measure its radiation pattern. In the experiment, the radiation pattern measurements of the S0 and SH0 modes at the center frequency of 300 kHz were conducted, and the measurement was made at the same point as in the CASE 1.

The comparison between the radiation patterns obtained from the proposed finite element analysis and experiments is shown in fig A.12. Good agreements can be observed

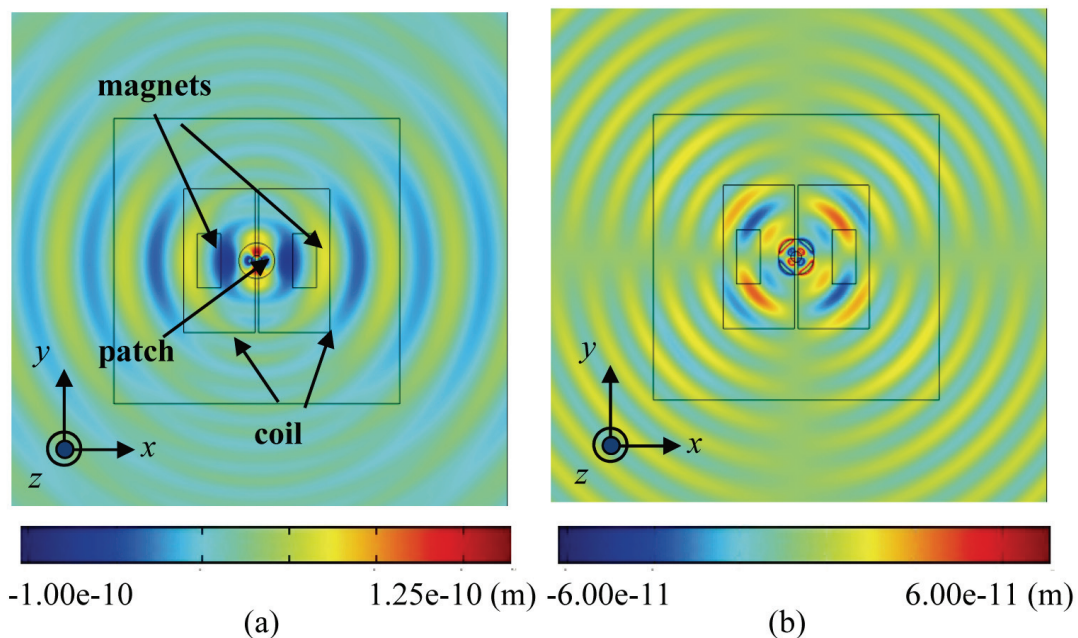


Fig. A.11 Plots of wave displacement fields of (a) S0 mode and (b) SH0 mode generated by the MPT of CASE 2 with $\theta = 0^\circ$

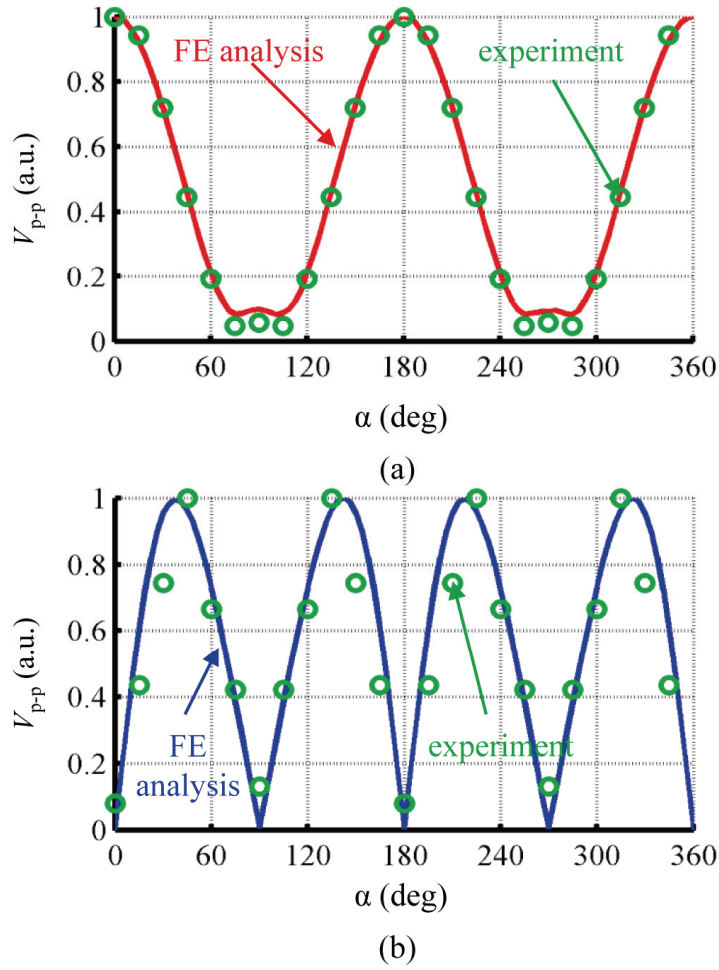


Fig. A.12 Comparison of the numerically and experimentally measured radiation patterns of (a) the S0 mode and (b) the SH0 mode for CASE 2 with $\theta = 0^\circ$

between two radiation patterns in fig. A.12. Interestingly, it can be seen that the side lobes (normalized V_{p-p} at $\alpha = 90^\circ$ and 270°) of S0 mode wave in fig. A.12 (a) is considerably reduced in comparison with the side lobes in CASE 1 shown in fig. A.9 (a). The major reason of the side lobe reduction is the different magnetic field distribution in the patch. Since the patch has higher permeability than other materials surrounding it, magnetic fields tend to flow along the patch. For the CASE 2 where the ring patch is

used, the induced magnetic flow is fluctuated accordingly. Therefore, there are significant y directional components in the static and dynamic magnetic fields inside the patch. These y directional components generate longitudinal deformation along y axis, which was not existed in CASE 1. Note that in the CASE 1, the main origin of the side lobe was the elongation along y axis which was accompanied with the dominant contraction along x axis. On the other hand, for the MPT with the ring patch, the contraction generated by the y components of the magnetic fields compensates the elongation, resulting in a significantly reduced side lobe. Regarding that the side lobe reduction is an important issue in elastic wave transducer, this observation may show that the present finite element analysis can be employed as an efficient tool for further patch design problem or optimization.

A.3.2 Numerical observations for elastic wave generation in MPT's

As previously explained, since the induced magnetic fields are non-uniformly distributed in the patch, the generated elastic guided waves are highly affected by the distribution of the static and dynamic magnetic fields inside the patch. As shown in equation (A.10), the external force term due to the magnetostriction is directly proportional to the coupling coefficients \mathbf{d} and the amplitude of the induced dynamic magnetic field \mathbf{H}_0 . Therefore, the external force term and following generated guided waves should have larger value at the region in which both the induced dynamic magnetic field and the magnetostrictive coupling coefficients are large. This indicates that the amount of the guided wave generation is not uniform in the patch. The magnetostrictive patch cannot be viewed as a

simple point source even at the far field.

Fig. A.13 shows the external shear strain term $e_{MS_{xy}}$ and related field's distributions in

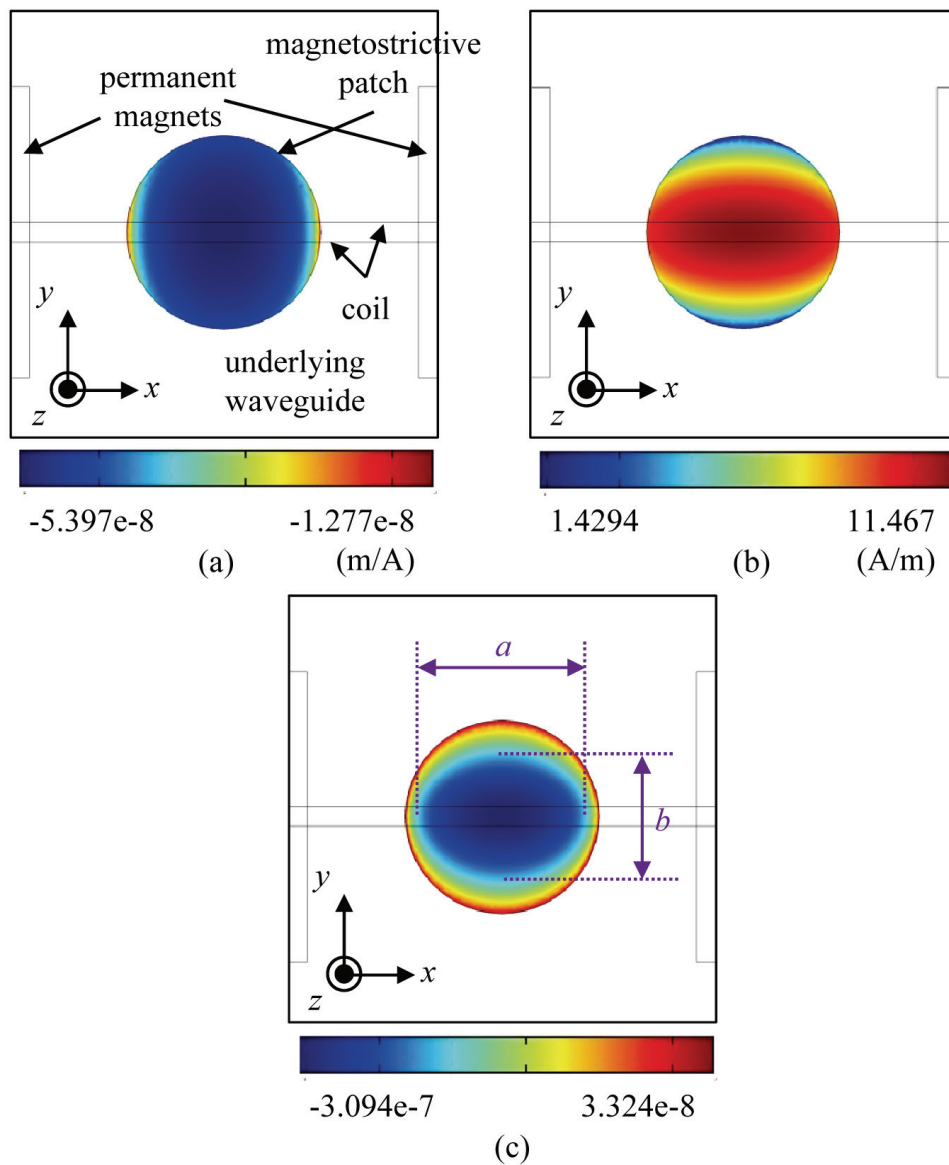


Fig. A.13 Distribution plots of (a) coupling coefficient d_{35} , (b) induced dynamic magnetic field H_{D_y} and (c) external shear force term $S_{MS_{xy}}$ in the patch

the MPT with circular patch considered in CASE 1 with $\theta = 90^\circ$. As shown in fig. A.13 (a), the coupling coefficient d_{35} is almost constant in the patch. On the other hand, since the coil is located directly above the patch and passes through the central region of the patch, the dynamic magnetic field H_{D_y} has a longish distribution inside the patch as shown in fig. A.13 (b). Thus, the external shear strain term e_{MS_y} also has a longish distribution similar to the dynamic magnetic field distribution, as shown in fig. A.13 (c). As a result, the generation of elastic guided wave in the MPT with $\theta = 90^\circ$ can be viewed as similar to that in a line source of which the length and width is a and b in fig. A.13 (c), respectively. Along the y axis (corresponding to the direction normal to the line source), the generated waves show constructive interference. On the other hand, along the x axis (corresponding to the direction parallel to the line source), the generated waves show destructive interference, resulting in a small wave radiation [96]. This point clearly explains why the normalized V_{p-p} along $\alpha = 0^\circ$ and $\alpha = 90^\circ$ is not same in the radiation pattern shown in fig. A.10 (c). In the same manner, the ratio of the normalized V_{p-p} along $\alpha = 0^\circ$ and $\alpha = 90^\circ$ is reduced to 0.3 from the 0.5 in the radiation pattern for $\theta = 0^\circ$, shown in fig. A.9 (a).

This line source-like behavior can be more clearly seen in the fig. A.14 in which the radiation pattern for various size of the patch is plotted. Considering the configuration of the MPT, the length a in fig. A.13 (c) becomes smaller while b remains relatively unchanged as the radius of the circular patch is reduced. Thus, it can be expected that the

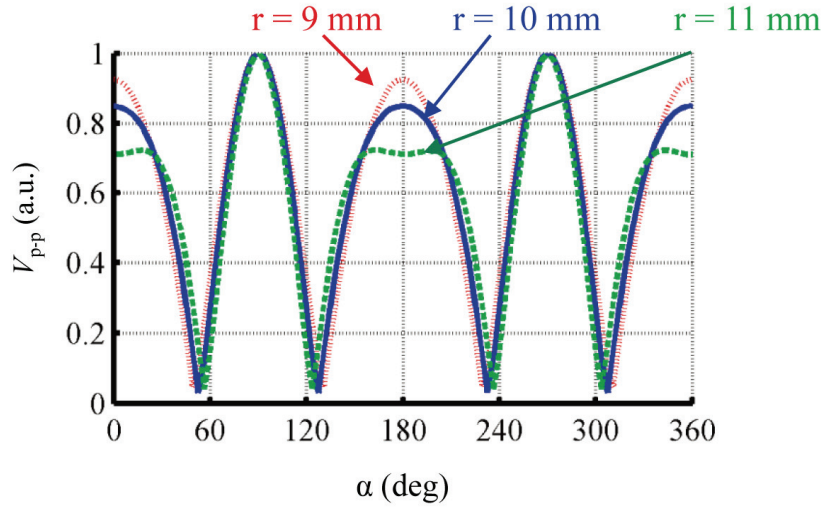


Fig. A.14 Comparison of the SH0 mode generated by the MPT with a circular patch of various radiuses with $\theta = 90^\circ$

generation of an elastic guided wave by MPT with smaller patch is more similar to that by a point source than that by MPT with larger patch. From fig. A.14, it can be seen that the normalized V_{p-p} along $\alpha = 0^\circ$ and $\alpha = 180^\circ$ becomes larger as the size of the patch is reduced. Thus, the line-source like behavior of MPT can be verified by this investigation. Likewise, any change of configuration or location of the magnetic circuits of MPT alters the static and dynamic magnetic field distribution in the patch, resulting in different wave radiation pattern of the MPT.

A.4. Conclusion

In this appendix, a linearized, time-harmonic finite element formulation was developed to investigate the radiation patterns of elastic guided waves that are generated by MPT's.

Because the magnetic fields generated by magnetic circuit are not uniformly distributed in the magnetostrictive patch, linear magnetostrictive equation was properly modified to consider various static magnetic field's orientation. In modification, special attentions were paid to properly consider the fact that the magnitude and direction of the static and dynamic magnetic fields vary from one point to another. During numerical simulation, time-harmonic analysis is used in studying the radiation patterns of the guided waves by MPT's in a plate to reduce computational time. Also, a technique to measure the wave radiation patterns of each desired modes such as S0 and SH0 modes from the time-harmonic analyses results was proposed. Finally, a three-step process was established to numerically calculate MPT's radiation patterns. The verification of the proposed approach is carried out by comparing the predicted radiation patterns and experimentally measured radiation patterns.

Another important issue explained in the appendix is that the dynamic strain behavior around the patch was investigated by numerical analysis results, which was almost impossible previously. It was shown that the non-uniformly distributed magnetic field in the patch significantly affects the far-field radiation pattern of the generated guided waves by MPT. Due to the longish distribution of the dynamic magnetic field, the patch cannot be treated as a point source even at far-field. These observations would be difficult to be studied if only experimental approaches were made. However, since the proposed investigation is based on the finite element analysis, the information for the dynamic wave behaviors around MPT could be obtained.

Since the proposed method can be applied to general MPT's, the proposed finite element analysis is expected to be widely used in predicting the radiation pattern of MPT's. Moreover, since the proposed finite element analysis can provide detailed physics around the patch, it can facilitate future researches related to MPT's. One of the possible future research would be transient analysis for MPT that can reveal all of the wave propagation phenomena such as interactions of the generated wave with cracks. Also, the developed finite element analysis is expected to provide basic analysis method in finding optimal configuration of an MPT which can better focus guided wave beams and show much reduced side lobes.

References

- [1] E. Abbe, *Beiträge zur theorie des mikroskops und der mikroskopischen wahrnehmung*, Arch. Mikrosk. Anat. **9**, 413-468 (1873)
- [2] E. Betzig and J. K. Trautman, *Near-field optics: microscopy, spectroscopy, and surface modification beyond the diffraction limit*, Science **257**, 189-195 (1992)
- [3] S. W. Hell and J. Wichmann, *Breaking the diffraction resolution limit by stimulated emission: stimulated-emission-depletion fluorescence microscopy*, Opt. Lett. **19**, 780-782 (1994)
- [4] A. S. G. Curtis, *The mechanism of adhesion of cells to glass*, J. Cell Bio. **20**, 199-215 (1964)
- [5] E. H. K. Stelzer, *Beyond the diffraction limit?*, Nature **417**, 806-807 (2002)
- [6] Z. Jacob, L. V. Alekseyev and E. Narimanov, *Optical Hyperlens: Far-field imaging beyond the diffraction limit*, Opt. Exp. **14**, 8247-8256 (2006)
- [7] A. Salandrino and N. Engheta, *Far-field subdiffraction optical microscopy using metamaterial crystals: Theory and simulations*, Phys. Rev. B **74**, 075103 (2006)

- [8] H. J. Lee, H. W. Kim and Y. Y. Kim, *Far-field subwavelength imaging for ultrasonic elastic waves in a plate using an elastic hyperlens*, Appl. Phys. Lett. **98**, 241912 (2011)
- [9] V. G. Veselago, *The electrodynamics of substances with simultaneously negative values of ϵ and μ* , Sov. Phys. Usp. **10**, 510-514 (1968)
- [10] J. B. Pendry, A. J. Holden, W. J. Stewart and I. Youngs, *Extremely low frequency plasmons in metallic meso structures*, Phys. Rev. Lett. **76**, 4773-4776 (1996)
- [11] J. B. Pendry, A. J. Holden, D. J. Robbins and W. J. Stewart, *Low frequency plasmons in thin wire structures*, J. Phys. Condens. Matter **10**, 4785-4809 (1998)
- [12] D. R. Smith, W. J. Padilla, D. C. Vier, S. C. Nemat-Nasser and S. Schylytz, *Composite Medium with Simultaneously Negative Permeability and Permittivity*, Phys. Rev. Lett. **84**, 4184-4187 (2000)
- [13] E. Cubukcu, K. Aydin, E. Ozbay, S. Foteinopoulou and C. M. Soukoulis, *Electromagnetic waves: Negative refraction by photonic crystals*, Nature **423**, 604-605 (2003)
- [14] J. B. Pendry, *Negative refraction makes a perfect lens*, Phys. Rev. Lett **85**, 3966-3969 (2000)

- [15] N. Fang, H. Lee, C. Sun and X. Zhang, *Sub-diffraction-limited optical imaging with a silver superlens*, Science **308**, 534-537 (2005)
- [16] D. Melville and R. Blaikie, *Super-resolution imaging through a planar silver layer*, Opt. Exp. **13**, 2127-2134 (2005)
- [17] B. Wood, J. B. Pendry and D. P. Tsai, *Directed sub-wavelength imaging using a layered metal-dielectric system*, Phys. Rev. B **74**, 115116 (2006)
- [18] T. Taubner, D. Korobkin, Y. Urzhumov, G. Shvets and R. Hillenbrand, *Near-field microscopy through a SiC superlens*, Science **313**, 1595 (2006)
- [19] C. Luo, S. G. Johnson and J. D. Joannopoulos, *Subwavelength imaging in photonic crystals*, Phys. Rev. B **68**, 045115 (2003)
- [20] P. V. Parimi, W. T. Lu, P. Vodo and S. Sridhar, *Imaging by flat lens using negative refraction*, Nature **426**, 404 (2003)
- [21] E. Cubukcu, K. Aydin, E. Ozbay, S. Foteinopoulou and C. M. Soukoulis, *Subwavelength resolution in a two-dimensional photonic-crystal-based superlens*, Phys. Rev. Lett. **91**, 207401 (2003)
- [22] X. Zhang and Z. Liu, *Superlenses to overcome the diffraction limit*, Nature **7**, 435-

441 (2008)

[23] M. Ambati, N. Fang, C. Sun and X. Zhang, *Surface resonant states and superlensing in acoustic metamaterials*, Phys. Rev. B **75**, 195447 (2007)

[24] K. Deng, Y. Ding, Z. He, H. Zhao, J. Shi and Z. Liu, *Theoretical study of subwavelength imaging by acoustic metamaterial slabs*, J. Appl. Phys. **105**, 124909 (2009)

[25] H. Jia, M. Ke, R. Hao, Y. Ye, F. Liu and Z. Liu, *Subwavelength imaging by a simple planar acoustic superlens*, Appl. Phys. Lett. **97**, 173507 (2010)

[26] A. Sukhovich, B. Merheb, K. Muralidharan, J. O. Vasseur, Y. Pennec, P. A. Deymier and J. H. Page, *Experimental and theoretical evidence for subwavelength imaging in phononic crystals*, Phys. Rev. Lett. **102**, 154301 (2009)

[27] Z. He, X. Li, J. Mei and Z. Liu, *Improving imaging resolution of a phononic crystal lens by employing acoustic surface waves*, J. Appl. Phys. **106**, 026105 (2009)

[28] Z. Liu, H. Lee, Y. Xiong, C. Sun and X. Zhang, *Far-field optical hyperlens magnifying sub-diffraction-limited objects*, Science **315**, 1686-1701 (2007)

[29] H. Lee, Z. Liu, Y. Xiong, C. Sun and X. Zhang, *Development of optical hyperlens*

for imaging below the diffraction limit, Opt. Exp. **15**, 15886-15891 (2007)

[30] A. V. Kildishev and E. E. Narimanov, *Impedance-matched hyperlens*, Opt. Lett. **32**, 3432-3434 (2007)

[31] W. Wang, H. Xing, L. Fanb, Y. Liu, J. Ma, L. Lin, C. Wang and X. Luo, *Far-field imaging device: planar hyperlens with magnification using multi-layer metamaterial*, Opt. Exp. **16**, 21142-21148 (2008)

[32] Y. Xiong, Z. W. Liu and X. Zhang, *A simple design of flat hyperlens for lithography and imaging with half-pitch resolution down to 20 nm*, Appl. Phys. Lett. **94**, 203108 (2009)

[33] J. Rho, Z. Ye, Y. Xiong, X. Yin, Z. Liu, H. Choi, G. Bartal and X. Zhang. *Spherical hyperlens for two-dimensional sub-diffractive imaging at visible frequencies*, Nat. Commun. **1**, 143 (2010)

[34] D. Lu and Z. Liu, *Hyperlenses and metalenses for far-field super-resolution imaging*, Nat. Commun. **3**, 1205 (2012)

[35] X. Ao and C. T. Chan, *Far-field image magnification for acoustic waves using anisotropic acoustic metamaterials*, Phys. Rev. E **77**, 025601 (2008)

- [36] J. Li, L. Fok, X. Yin, G. Bartal and X. Zhang, *Experimental demonstration of an acoustic magnifying hyperlens* Nat. Mat. **8**, 931-934 (2009)
- [37] P. Sheng, *Acoustic lenses to shout about*, Nat. Mat. **8**, 928-929 (2009)
- [38] J. Zhu, J. Christensen, J. Jung, L. Martin-Moreno, X. Yin, L. Fok, X. Zhang and F. J. Garcia-Vidal, *A holey-structured metamaterial for acoustic deep-subwavelength imaging*, Nat. Phys. **7**, 52-55 (2011)
- [39] T. Y. Chiang, L. Y. Wu, C. N. Tsai and L. W. Chen, *A multilayered acoustic hyperlens with acoustic metamaterials*, Appl. Phys. A **103**, 355-359 (2011).
- [40] B. A. Auld, *Acoustic fields and waves in solids*, Krieger Publishing Company, Florida, 1990
- [40] E. Hacht, *Optics*, Addison Wesley: San Francisco, 2002
- [41] K. F. Graff, *Wave motion in elastic solids*, Dover Publications, INC: New York, 1991
- [42] S. Durant, Z. Liu, J. M. Steele and X. Zhang, *Theory of the transmission properties of an optical far-field superlens for imaging beyond the diffraction limit*, J. Opt. Soc. Am. B **23**, 2383–2392 (2006)

- [43] Z. Liu, S. Durant, H. Lee, Y. Pikus, Y. Xiong, C. Sun and X. Zhang, *Experimental studies of far-field superlens for sub-diffractive optical imaging*, Opt. Exp. **15**, 6947–6954 (2007)
- [44] Z. Liu, S. Durant, H. Lee, Y. Pikus, N. Fang, Y. Xiong, C. Sun and X. Zhang, *Far-field optical superlens*, Nano Lett. **7**, 403–408 (2007)
- [45] Y. Xiong, Z. Liu, S. Durant, H. Lee, C. Sun and X. Zhang, *Tuning the far-field superlens: from UV to visible*, Opt. Exp. **15**, 7095–7102 (2007)
- [46] C. Ma, R. Aguirre and Z. Liu, *Advances in the hyperlens*, Chin. Sci. Bull. **55**, 2618-2624 (2010)
- [47] Z. Liu, X. Zhang, Y. Mao, Y. Y. Zhu, Z. Yang, C. T. Chan and P. Sheng, *Locally resonant sonic materials*, Science **289**, 1734-1736 (2000)
- [48] Z. Liu, C. T. Chan and P. Sheng, *Analytic model of phononic crystals with local resonances*, Phys. Rev. B **71**, 014103 (2005)
- [49] N. Fang, D. Xi, J. Xu, M. Ambati, W. Srituravanich, C. Sun and X. Zhang, *Ultrasonic metamaterials with negative modulus*, Nat. Mater. **5**, 452-456 (2006)

- [50] Z. Yang, J. Mei, M. Yang, N. H. Chan and P. Sheng, *Membrane-type acoustic metamaterial with negative dynamic mass*, Phys. Rev. Lett. **101**, 204301 (2008)
- [51] S. H. Lee, C. M. Park, Y. M. Seo, Z. G. Wang and C. K. Kim, *Composite acoustic medium with simultaneously negative density and modulus*, Phys. Rev. Lett. **104**, 054301 (2010)
- [52] Y. Lai, Y. Wu, P. Sheng and Z. Q. Zhang, *Hybrid elastic solid*, Nat. Mater. **10**, 620-624 (2011)
- [53] M. S. Kushwaha, P. Halevi, L. Dobrzynski and B. Djafari-Rouhani, *Acoustic band structure of periodic elastic composites*, Phys. Rev. Lett. **71**, 2022-2025 (1993)
- [54] M. Sigalas and E. N. Economou, *Band structure of elastic waves in two dimensional systems*, Solid State Commun. **86**, 141-143 (1993)
- [55] L. Meirovitch, *Fundamentals of vibrations*, McGraw-Hill: Singapore, 2001
- [56] J. Mei, G. Ma, M. Yang, Z. Yang, W. Wen and P. Sheng, *Dark acoustic metamaterials as super absorbers for low-frequency sound*, Nat. Commun. **3**, 756 (2012)
- [57] Z. Liang and J. Li, *Extreme Acoustic Metamaterial by Coiling Up Space*, Phys. Rev. Lett. **108**, 114301 (2012)

[58] Y. Xie, B. I. Popa, L. Zigoneanu and S. A. Cummer, *Measurement of a Broadband Negative Index with Space-Coiling Acoustic Metamaterials*, Phys. Rev. Lett. **110**, 175501 (2013)

[59] Z. Liang, T. Feng, S. Lok, F. Liu, K. B. Ng, C. H. Chan, J. Wang, S. Han, S. Lee and J. Li, *Space-coiling metamaterials with double negativity and conical dispersion*, Sci. Rep. **3**, 1614-1619 (2013)

[60] P. Langlet, A. C. Hladky-Hennion and J. N. Decarpigny, *Analysis of the propagation of plane acoustic waves in passive periodic materials using the finite element method*, J. Acoust. Soc. Am. **98**, 2792-2800 (1995)

[61] M. S. Kushwaha, P. Halevi, L. Dobrzynski and B. Djarafi-Rouhani, *Acoustic band structure of periodic elastic composites*, Phys. Rev. Lett., **71**, 2022-2025 (1993)

[62] M. S. Kushwaha, P. Halevi, G. Martinez, L. Dobrzynski and B. Djarafi-Rouhani, *Theory of acoustic band structure of periodic elastic composites*, Phys. Rev. B **49**, 2313-2322 (1994)

[63] K. J. Bathe, *Finite element procedures*, Prentice Hall: New Jersey (1992)

[64] COMSOL Multiphysics, *COMSOL Multiphysics modeling guide: Version 3.5*,

COMSOL AB: Stockholm (2008)

[65] S. H. Cho, K. H. Sun, J. S. Lee and Y. Y. Kim, *Magnetostrictive transducer for generating and measuring elastic waves, and apparatus for structural diagnosis using the same*, United States: United States Patent No. US 6,924,642 B1 (2005)

[66] H. Kwun, *Method and apparatus for nondestructive inspection of plate type ferromagnetic structures using magnetostrictive techniques*, United States: United States Patent No. 6,294,912 B1 (2001)

[67] G. M. Light, H. Kwun, S. Y. Kim and R. L. Spinks, *Method and apparatus for short term inspection of long term structural health monitoring*, United States: United States Patent No. 6,396,262 B2 (2001)

[68] S. H. Cho, J. S. Lee and Y. Y. Kim, *Guided wave transduction experiment using a circular magnetostrictive patch and a figure-of-eight coil in nonferromagnetic plates*, Appl. Phys. Lett. **88** 224101 (2006)

[69] J. S. Lee, S. H. Cho and Y. Y. Kim, *Radiation pattern of Lamb waves generated by a circular magnetostrictive patch transducer*, Appl. Phys. Lett. **90** 054102 (2007)

[70] J. S. Lee, Y. Y. Kim and S. H. Cho, *Beam-focused shear-horizontal wave generation in a plate by a circular magnetostrictive patch transducer employing a planar solenoid*

array, Smart Mater. Struct. **18** 015009 (2009)

[71] M. Hirao and H. Ogi, *EMATS for Science and Industry*, Kluwer Academic Publishers: Dordrecht (2003)

[72] G. Engdahl, *Handbook of giant magnetostrictive materials*, Academic Press: San Diego, CA (2000)

[73] D. C. Jiles, *Theory of the magnetomechanical effect*, J. Phys. D: Appl. Phys. **28** 1537-1546 (1995)

[74] J. H. Oh, K. H. Sun and Y. Y. Kim, *Time-harmonic finite element analysis of guided waves generated by magnetostrictive patch transducers*, Smart. Mater. Struct. **22**, 085007 (2013)

[75] L. Brillouin, L. *Wave Propagation in Periodic Structures*, Dover Publications, Inc.: New York, NY (1946).

[76] H. H. Huang, C. T. Sun and G. L. Huang, *On the negative effective mass density in acoustic metamaterials*, Int. J. Eng. Sci. **47**, 610-617 (2009)

[77] Y. Y. Kim and H. C. Lee, *Analytic solutions for fundamental eignefrequencies of optical actuators in six directions of motion*, Int. J. Solid Struct. **38**, 1327-1339 (2001)

- [78] K. Washizu, *Variational Methods in Elasticity and Plasticity*, 3rd Ed., Pergamon Press: New York, NY (1982)
- [79] S. P. Timoshenko and J. N. Goodier, *Theory of elasticity*, McGraw-Hill: Singapore (1970)
- [80] M. Anjanappa and J. Bi, *A theoretical and experimental study of magnetostrictive mini-actuators*, *Smart Mater. Struct.* **3** 83-91 (1994)
- [81] F. T. Calkins, A. B. Flatau and M. J. Dapino, *Overview of Magnetostrictive Sensor Technology*, *J. Intell. Mater. Sys. Struct.* **18** 1057-1066 (2007)
- [82] M. J. Dapino, R. C. Smith, F. T. Calkins and A. B. Flatau, *A coupled magnetomechanical model for magnetostrictive transducers and its application to Villari-effect sensors*, *J. Intell. Mater. Sys. Struct.* **13** 737-747 (2002)
- [83] K. Ohmata, M. Zaike and T. Koh, *A three-link arm type vibration control device using magnetostrictive actuators*, *J. Alloys Compounds* **258** 74-78 (1997)
- [84] H. M. Zhou, X. J. Zheng and Y. H. Zhou, *Active vibration control of nonlinear giant magnetostrictive actuators*, *Smart Mater. Struct.* **15** 792-798 (2006)

- [85] L. Wang and F. G. Yuan, *Vibration energy harvesting by magnetostrictive material*, Smart Mater. Struct. **17** 045009 (2008)
- [86] X. Zhao and D. G. Lord, *Application of the Villari effect to electric power harvesting*, J. Appl. Phys. **99** 08M703 (2006)
- [87] E. Kannan, B. W. Maxfield and K. Balasubramaniam, *SHM of pipes using torsional waves generated by in situ magnetostrictive tapes*, Smart Mater. Struct. **16** 2505-2515 (2007)
- [88] K. H. Sun, S. H. Cho and Y. Y. Kim, *Topology design optimization of a magnetostrictive patch for maximizing elastic wave transduction in waveguides*, IEEE Trans. Magn. **44** 2373-2380 (2008)
- [89] J. Kim and E. Jung, *Finite element analysis for acoustic characteristics of a magnetostrictive transducer*, Smart Mater. and Struct. **14** 1273-1280 (2005)
- [90] J. L. Pérez-Aparicio and H. Sosa, *A continuum three-dimensional, fully coupled, dynamic, non-linear finite element formulation for magnetostrictive materials*, Smart Mater. and Struct. **13** 493-502 (2004)
- [91] R. Ribichini, F. Cegla, P. B. Nagy and P. Cawley, *Quantitative modeling of the transduction of electromagnetic acoustic transducers operating on ferromagnetic media*,

IEEE Trans. Ultrason. Ferroelectr. Freq. Control **57** 2808-2817 (2010)

[92] R. Ribichini, F. Cegla, P. B. Nagy and P. Cawley, *Study and comparison of different EMAT configurations for SH wave inspection*, IEEE Trans. Ultrason. Ferroelectr. Freq. Control **58** 2571-2581 (2011)

[93] J. L. Rose, *Ultrasonic Waves in Solid Media*, Cambridge University Press: Cambridge (1999)

[94] IEEE, *IEEE Standard on Magnetostrictive Materials: Piezomagnetic Nomenclature*, IEEE: New York, NY (1971)

[95] Y. Wan, D. Fang and K. C. Hwang, *Non-linear constitutive relations for magnetostrictive materials*, Int. J. Non-linear Mech. **38** 1053-1065 (2003)

[96] L. E. Kinsler, A. R. Frey, A. B. Coppens and J. V. Sanders, *Fundamentals of Acoustics*, John Wiley & Sons, Inc.: New York, NY (1999)

Abstract (Korean)

하이퍼볼릭 메타물질을 응용한 초음파의 회절한계 이상 해상도 구현

오 주 환

서울대학교 대학원

기계항공공학부

본 논문에서는 탄성파의 회절 한계(diffraction limit)를 넘어선 초고해상도(sub-wavelength resolution)를 구현 가능케 하는 탄성 메타물질(elastic metamaterial) 기반의 렌즈를 제안한다. 일반적으로 탄성 초음파에 기반한 이미징 기술은 매우 효과적인 기술로 인정받고 있으나, 반파장 이상의 해상도를 얻을 수 없는 이론적 해상도 한계인 회절 한계가 존재한다는 것이 큰 문제가 되어왔다. 이에 따라 ‘어떻게 회절 한계를 극복할 수 있을 것인가?’가 매우 중요한 이슈가 되고 있다. 최근 메타물질 분야에서의 큰 진보에 힘입어 회절 한계 이상의 해상도를 구현할 수 있는 하이퍼렌즈(hyperlens)의 개념이 제안된 바 있으나 탄성 분야에서의 하이퍼렌즈 관련 연구는 매우 드물며, 기존에 제안된 탄성 하이퍼렌즈는 그 성능이 제한적인 실정이다. 이에 따라 본 연구에서는 기존의 탄성 하이퍼렌즈보다 뛰어난 해상도를 보이는 새로운 탄성 하이퍼렌즈를 제

안하고자 한다.

본 연구에서 수행한 연구는 새로운 탄성 하이퍼렌즈의 제안과 더불어 물리적, 수치해석적, 실험적 그리고 이론적 접근을 포괄한다. 먼저 회절 한계의 물리적 근원을 검토한 후 기존의 탄성 하이퍼렌즈가 지니는 한계를 극복할 수 있는 방안을 제안한다. 이에 따라 새로운 탄성 메타물질을 개발하고 이에 기반한 새로운 탄성 하이퍼렌즈를 설계한다. 제안된 탄성 하이퍼렌즈의 성능을 검증하기 위해 유한요소 해석 기법을 정립하고 수치해석 기반 탄성과 시뮬레이션을 수행한다. 이어서 제안된 탄성 하이퍼렌즈에서의 회절한계 이상 해상도 구현 여부를 실험적으로 검증한다. 실험 수행시 반파장 이하의 두 파동 가진 원을 실험적으로 구현하기 위한 새로운 탄성과 트랜스듀서(transducer)를 개발하고 가진 신호의 조절, 측정 신호 보정 기술 등의 보조 실험 기법을 도입한다. 마지막으로 제안된 메타물질에 대한 등가 질량-스프링 모델(equivalent mass-spring model)을 구축하고 이로부터 내부 파동 거동에 대한 이론적 수식을 정립한다. 뿐만 아니라 제안된 등가 질량-스프링 모델을 통해 제안된 탄성 하이퍼렌즈의 성능 향상을 위한 설계 개선 방향을 다룬다.

주제어 : 하이퍼볼릭 등주파수 곡선, 탄성 하이퍼렌즈, 회절한계 이상 해상도,

탄성 메타물질

학 번 : 2008-20762

Acknowledgements

This work was supported by the National Research Foundation of Korea (NRF) grant (No: 2013035194) funded by the Korean Ministry of Education, Science and Technology (MEST) contracted through IAMD at Seoul National University.